Identification of cambium stem cell factors and their positioning mechanism

Gugan Eswaran[1,2]†, Xixi Zhang[1,2]†, Jacob Pieter Rutten[3]†, Jingyi Han[4]‡, Hiroyuki Iida[1,2]‡, Jennifer Lopez Ortiz[1,2]‡, Riikka Mäkilä[1,2]‡, Brecht Wybouw[1,2], Benjamin Planterose Jiménez[3], Leo Vainio[1,2], Alexis Porcher[1], Marina Leal Gavarron[1,2], Jing Zhang[1,2]¶, Tiina Blomster[1,2], Xin Wang[1,2], David Dolan[4]§, Ondřej Smetana[1,2], Siobhán M. Brady[5], Melis Kucukoglu Topcu[1], Kirsten ten Tusscher[3,6*], J. Peter Etchells[4*], Ari Pekka Mähönen[1,2*]

[1] Organismal and Evolutionary Biology Research Programme, Faculty of Biological and Environmental Sciences and Viikki Plant Science Centre, University of Helsinki, 00014 Helsinki, Finland.

[2] Institute of Biotechnology, HiLIFE, University of Helsinki, 00014 Helsinki, Finland.

[3] Theoretical Biology and Bioinformatics, Utrecht University, Utrecht 3584 CH, the Netherlands.

[4] Department of Biosciences, Durham University, Durham DH1 3LE, United Kingdom.

[5] Department of Plant Biology, University of California, Davis, Davis, CA, 95616 USA.

[6] Experimental and Computational Plant Development, Utrecht University, Utrecht 3584 CH, The Netherlands.

† These authors contributed equally to this work.

‡ These authors contributed equally to this work.

¶ Current address: Department of Plant Biology and Ecology, College of Life Sciences, Nankai University, Tianjin 300071, China.

§ Current address: Department of Informatics, University of Bergen, 5020 Bergen, Norway.

[*] Correspondence: K.H.W.J.tenTusscher@uu.nl; peter.etchells@durham.ac.uk and aripekka.mahonen@helsinki.fi

Abstract

Wood constitutes the largest reservoir of terrestrial biomass. Composed of xylem, it arises from one side of the vascular cambium, a bifacial stem cell niche that also produces phloem on the opposing side. It is currently unknown which molecular factors endow cambium stem cell identity. Here we show that TDIF ligand-activated PXY receptors promote the expression of CAMBIUM-EXPRESSED AINTEGUMENTA-LIKE (CAIL) transcription factors to define cambium stem cell identity in the *Arabidopsis* root. By sequestrating the phloem-originated TDIF, xylem-expressed PXY confines the TDIF signaling front, resulting in the activation of CAIL expression and stem cell identity in only a narrow domain. Our findings show how signals emanating from cells on opposing sides ensure robust yet dynamically adjustable positioning of a bifacial stem cell layer.

One-Sentence Summary: The TDIF-PXY ligand-receptor pair defines cambium stem cells by controlling the expression of CAIL transcription factors.

Main Text

In seed plants, stem cell populations that drive apical-basal growth are formed in the embryo. However, the vascular cambium (hereafter cambium), which promotes radial growth, and thus the majority of plant biomass, is formed following germination (*1*, *2*). In the *Arabidopsis thaliana* root, this occurs when cells with xylem identity promote stem cell function in their neighbors. This xylem identity cell layer is thus considered to be the cambium organizer (*3*) (**Fig. 1A**). The cambium is dynamic in size, ranging from a few to multiple undifferentiated cells, depending on the level of proliferation, yet contains only a single bifacial stem cell layer (*3*–*5*). Due to the rarity of transit amplifying divisions within the xylem or phloem lineages (*3*), the vast majority of observed cell divisions in the *Arabidopsis* cambium are stem cell divisions. The remaining undifferentiated cells in the cambium have xylem or phloem identity (**Fig. 1A**). How the organizer cells can exert their exquisite control over stem cells at variable distance is still unknown. A prerequisite to addressing this question is identification of regulators that define stem cell identity within the cambium, which have not been determined either. In the root cambium, the stem cell organizer is defined by a local signaling maximum of auxin, which contributes to stem cell positioning (*3*, *6*). Auxin promotes the expression of CLASS III HOMEODOMAIN-LEUCINE ZIPPER (HD-ZIP III) transcription factors defining xylem identity (*3*, *7*, *8*), as well as a receptor kinase, PHLOEM INTERCALATED WITH XYLEM (PXY) (*3*). TRACHEARY ELEMENT DIFFERENTIATION INHIBITORY FACTOR (TDIF), which is derived from phloem-expressed CLAVATA3/ESR-RELATED 41 (CLE41) and CLE44, is the cognate ligand of PXY. Disruption of TDIF-PXY signaling causes major patterning and stem cell maintenance defects (*9*–*14*). These defects suggest that the elusive regulators of cambium stem cell identity are likely to be TDIF-PXY regulated. Here we define a set of *AINTEGUMENTA-like* genes (CAMBIUM-EXPRESSED AILs; CAILs) as performing this function, and show that their positioning is defined by opposing gradients of TDIF and auxin.

Identification of CAILs as cambium stem cell factors downstream of TDIF-PXY

To identify genes involved in specifying cambium stem cells, we compared transcriptomes of wild type *Arabidopsis* seedlings undergoing cambium initiation to an overexpressor of TDIF (*p35S:CLE41*) and *pxy* mutant, characterized by enhanced or reduced TDIF-PXY signaling, respectively (*9*, *12*). In line with these phenotypes, GO terms under-represented in *pxy* included meristem maintenance; those over-represented in *p35S:CLE41* included meristem growth (**Fig. S1**). Transcripts under-represented in *pxy* and over-represented in *p35S:CLE41* included *PLETHORA 3* and *5* (*PLT3* and *PLT5*), members of the *AINTEGUMENTA-LIKE/PLT* (*AIL/PLT*) family (**fig. S1; and data S1**). Previously, different members of the AIL/PLT transcription factor family have been associated with promoting stemness and/or an undifferentiated state in apical meristems (*15*–*18*). In the cambium, *AINTEGUMENTA* (*ANT*) is specifically expressed in stem cells (*3*, *19*) and its absence leads to reduced radial growth (*19*, *20*). Thus, AIL/PLTs represent strong candidates for cambial stem cell regulators. Ectopic cell proliferation in *p35S:CLE41* occurs where xylem parenchyma cells reside in wild type. This phenotype was suppressed by *plt3plt5*, demonstrating that these genes are required for ectopic cambium proliferation in *p35S:CLE41*

(**Fig. 1, B and C**). Nevertheless, the *plt3plt5* line demonstrated no obvious cambium phenotype (**Fig. 1, B and C**). Thus, we investigated the AIL/PLT family for further redundancy. The AIL/PLT family consists of 8 members (*21*, *22*). Expression analysis of *AIL*/*PLT* fluorescent reporters showed that *ANT* (*3*), *PLT3*, *PLT5* and *PLT7* are expressed in the cambium, while *PLT1*, *PLT2* and *PLT4* expression appeared to be absent (**Fig. 1D; and fig. S2**). *ANT* was downregulated in the *pxy* mutant and *PLT7* upregulated in *p35S:CLE41* (**fig. S1C; and data S1**). Thus, we hypothesize that PLT3, PLT5, PLT7 and ANT act redundantly in cambium development downstream of TDIF-PXY signaling. Supporting this hypothesis, induction of *ANT-YFP* or *PLT5-YFP* under the *PXY* promoter restored cambium activity in a *pxy* mutant (**Fig. 1E**). While *ant* mutants are characterized by reductions in cambium activity (*19*, *20*), *PLT3*, *PLT5* and *PLT7* mutant combinations failed to show cambial phenotypes (**Fig. 1, F and G; and fig. S3C**). To determine potential redundancy between *ant* and *plt*s, several mutant combinations were analyzed. While *antplt5* roots demonstrated slight but significant reductions of secondary growth, quadruple mutant (*plt3plt5plt7-cr;ant-GK*) roots showed major reductions in secondary growth (**fig. S3, A and C**). Similarly, in *plt3plt5plt7-cr* (*23*) lines transformed with a gene editing construct to target *ANT*, secondary growth was strongly reduced in the majority of T1 individuals. However, *plt3plt5plt7-cr;ant-GK* and *plt3plt5plt7-cr;ant-cr* lines were unable to maintain a shoot apical meristem (**fig. S3B and fig. S4A**), as previously shown for *antplt3plt7* (*24*). Thus, both to assess loss of the four *AIL*/*PLT* genes during cambium development, and to avoid secondary effects caused by shoot apical meristem loss, we generated an inducible genome editing (IGE) (*25*) construct targeting *ANT* (*ANT-IGE*). *ANT-IGE* was introduced to both the null *plt3plt5plt7-cr* (*23*) and *plt3plt5plt7-tdna* (*22*) backgrounds**.** Primary growth appeared normal in both conditional quadruple mutants, albeit *plt3plt5plt7-cr;IGE-ant* showed slightly reduced root length (**fig. S4A**). *plt3plt5plt7-tdna;IGE-ant* displayed radial sectors without differentiated secondary xylem vessels and reduced phloem sieve elements suggesting loss of cambium identity (**fig. S4C**). In the *plt3plt5plt7-cr;IGE-ant* null background, secondary growth was significantly reduced, and this was associated with a reduction in cambial cells per radial cell file, or occasionally, cell files with a complete loss of cambial cells (**Fig. 1, F and G; and fig. S4B**). These data demonstrate that the four CAILs - PLT3, PLT5, PLT7, and ANT - are critical in maintaining cambium identity.

The expression of *CAIL*s is typically present in both daughter cells following recent divisions, which are identifiable by the presence of a thin cell wall (white arrowheads in **Fig. 2A**). As such, *CAIL* expression marks cambial stem cells and their daughters. In these daughter cells partial overlap between *CAIL*s and the neighboring early xylem and phloem identity reporters occurs (*3*) (**Fig. 2A; and fig. S5, A and B**). To investigate the role of CAILs in shaping these cell identities, we focused on PLT5 as a representative factor. To obtain a genome-wide view of PLT5 action in the cambium we performed RNA-seq on root tissues undergoing radial growth after 8 hours and 24 hours of induced overexpression of *PLT5*. We generated a 17-β-estradiol inducible (*26*) line, *35S:XVE>>PLT5-TagRFP,* for that purpose. Remarkably, 37% of xylem identity (*27*) and 53% phloem identity (*28*) genes were downregulated after 8 hours of *PLT5* induction, in comparison to 26% of all genes downregulated. Among core cell cycle genes (*29*) 55% were upregulated after 24 hours of PLT5 overexpression in comparison to 36% of all upregulated genes (**Fig. 2B; fig. S6, A and B; and data S1**). Thus, PLT5 regulates a large set of genes associated with cell proliferation and xylem and phloem formation, upregulating the former while downregulating the latter two.

Next, we investigated the consequences of *PLT5* induction on morphogenesis. Short-term *PLT5* induction promoted ectopic DNA replication observed with EdU staining, accompanied by ectopic cell divisions within xylem and phloem (**Fig. 2, D and E; and fig. S6C**). In support of our RNA-seq data (**Fig. 2B; fig. S6, A and B**), *PLT5* induction caused rapid down-regulation of xylem (*VND6*) and phloem (*PEAR1, APL*) reporter lines (**fig. S6D; and Fig. 2C**), leading to inhibition of xylem vessel and phloem sieve element formation (**Fig. 2, F and G**), and subsequently, inhibition of radial growth (**fig. S6E**). These data demonstrate that in the cambium, PLT5 maintains cell division capacity and the undifferentiated state of cambium cells. This occurs both through promoting cell division and through active opposition of differentiation to either xylem or phloem. Together, over-expression and loss-of-function analysis shows that CAILs are key cambium stem cell factors.

Computational model for cell fate determination in cambium

CAIL expression occurs only in a narrow stem cell domain of the cambium. This contrasts with the *PXY* receptor expression domain, which is strongest in the xylem/organizer domain tapering off towards weak expression in stem cells (*3*) **(Fig. 3A; and fig. S5C**). Even though cambium activity was restored in *pxy* by induction of *PLT5-YFP* or *ANT-YFP* in the *PXY* domain*,* xylem differentiation appeared perturbed (**Fig. 1E**). This demonstrates the importance of constrained CAIL expression in the stem cell, raising the question of how the downstream CAILs are constrained to the subdomain of low *PXY* expression. In any biological system, ligand binding to a receptor results in its sequestration from the pool of free ligands. *CLE41* expression and the subsequent TDIF peptide gradient extends from the phloem (*12*, *13*, *30*) (**fig. S5C**), thus the first PXY receptors that TDIF peptides encounter are those located at the lower end of the PXY gradient. Therefore, we hypothesized that sufficiently strong TDIF sequestration by PXY could abrogate further TDIF spread and thereby lead to a narrow active TDIF-PXY signaling domain and hence restrict *CAIL* expression to the stem cells. After a 24-hour application of synthetic TDIF peptide, the expression of *PLT5* and *ANT* expanded towards xylem parenchyma, coinciding with ectopic cell divisions (**Fig. 3A; and fig. S5D**), supporting the idea that excess TDIF prohibits sufficient sequestration. Long-term TDIF treatment led to further expansion of *PLT5* expression and cell proliferation in xylem parenchyma (**Fig. 3B**).

To address whether the TDIF sequestration hypothesis could explain the above observations, we developed a computational model (codes are available on https://tbb.bio.uu.nl/khwjtuss/cambium as well as (31)). This model combined the regulatory interactions discovered here and those published previously (**Fig. 3C, top panel; and fig. S**7), to determine the spatial patterning of the cambium and cells differentiating towards xylem and phloem fate **(Modelling Methods**). Previous models investigated cambium patterning dynamics while partly invoking hypothetical regulatory factors (*31*–*34*). Instead, we focused on testing the TDIF sequestration hypothesis while also incorporating the role of the newly identified CAIL factors by using a simple 1D static tissue model. The model incorporates TDIF-PXY promotion of *PLT5* (as a representative of the PLT subclade) and *ANT* (**Fig. 3A; and fig. S5C**); repression of *PXY* by PLT5 which we observed upon induction of *PLT5* (**Fig. 2B; and Fig. 3D**); auxin-mediated promotion of HD-ZIP III (*3*, *7*, *8*), ANT (*3*, *35*), and PXY (*3*); and HD-ZIP III promotion of xylem differentiation (*3*, *36*–*38*) and inhibition of phloem differentiation (*3*, *39*). By using *HD-ZIP III*-targeting inducible *miR165a* (*3*), we noticed that HD-ZIP IIIs repress *ANT* in xylem identity cells (**Fig. 3E**). Prior to testing the influence of TDIF sequestration by PXY in a multicellular setting, we first explored the capacity of this network to correctly assign cell fate identity in a single cell given various auxin and TDIF levels (for details on parameter sweep see **Modelling Methods**). Specifically, (i) cells experiencing high auxin and low TDIF levels should express HD-ZIP III and acquire xylem fate;

(ii) cells with high TDIF and low auxin levels should obtain phloem fate; and (iii) cells with intermediate TDIF and auxin levels should have high ANT and PLT5 expression and thus cambium stem cell identity. Parameter sweeps in which simulations were performed until a steady state was reached showed that these requirements were met for a wide range of parameter values independently of specific fate determination threshold levels (**fig. S8, A-C; and Modelling Methods).** However, in the presence of high TDIF and high auxin levels, a more robust formation of the xylem occurs in conditions when we maximize the repression of ANT by HD-ZIP III (**fig. S8D; and Fig. 3C, bottom panel**).

TDIF sequestration mechanism explains observed cambium phenotypes

From the parameter sweep we derived a final set of parameter values providing robust single cell patterning (Supplementary Tables S1-S3) with maximum HD-ZIP III-mediated ANT repression. Arabidopsis root cambium radial cell files typically consist of 2 to 6 cells (**Fig. 1, A and G**)(*3*), and cell type patterning has to be robust to variations in cambium width. Therefore, we extended our model to a row of 3-5 cells on which oppositely oriented auxin and TDIF gradients were superimposed. To decipher the role of gene regulatory network (GRN) architecture versus TDIF sequestration on cambium patterning robustness, we decoupled in our model the TDIF-PXY complex formation that induces ANT/PLT5 expression from the TDIF sequestration that limits the amount of TDIF available for diffusion (for details see Supplemental Methods). We started with model settings in which TDIF sequestration was ignored and TDIF-PXY binding was set to medium strength (K_d of 5). In a 3-cell tissue these settings readily resulted in correct patterning of the three cell types for variable TDIF gradient settings (**fig. S9A**). However, under 5-cell settings, overlap between the TDIF and PXY gradients was insufficient for TDIF-PXY to promote PLT5 expression, even when TDIF production was further elevated. Furthermore, this same elevated TDIF level caused invasion of PLT5 expression into the xylem in 3-cell settings (**fig. S9B)**. Clearly, increasing or decreasing TDIF expression would improve one issue at the cost of the other indicating a lack of robustness in cell type patterning across variable tissue widths. As a next step, we compared the patterning capacity of this strong ANT repression with that of strong TDIF sequestration (K_d of 1) (**fig. S9C and D**), both with default TDIF gradient parameters. In the strong TDIF sequestration scenario we halved ANT repression, thus reducing the impact of GRN architecture to enable us to focus instead on the effect TDIF sequestration has on patterning. (**fig. S10**; **Modelling Methods**). In contrast to the patterning issues, we observed with strong ANT repression, strong TDIF-PXY binding and TDIF sequestration ensured sufficient PXY-TDIF overlap under the 5-cell settings to promote PLT5 expression, and under 3-cell settings PLT5 invasion into the xylem was largely prevented. Nevertheless, under those settings, lack of strong HD-ZIP III-mediated repression on ANT allowed auxin to induce ANT in the xylem in the 3-cell settings. Combined, this suggests that both regulatory network and sequestration mechanisms must be active *in planta* to some extent. To test which of these mechanisms dominates patterning of the narrow cambial domain observed *in planta*, we sought to investigate both hypothesized mechanisms in perturbed conditions simulating patterning in a 4-cell tissue. One prominent difference between the modelled "maximum HD-ZIP III ANT repression", and "strong TDIF sequestration" parameter regimes was the predicted behavior of ANT. Under maximum HD-ZIP III-mediated ANT repression, the model predicted that decreased *PXY* expression would reduce active TDIF-PXY complexes and consequently PLT5 expression in the cambium (**Fig. 4A**). By contrast, in regimes where TDIF sequestration was dominant, the model predicted that decreased

PXY expression resulted in xylemward expansion of TDIF gradient, leading to activation of further PXY receptors and hence ANT expression towards the xylem (**Fig. 4B**). To compare these differential predictions against *in planta* behavior, we lowered *PXY* levels by inducible RNA interference (*RNAi-PXY*) in an *ANT* fluorescent reporter background in Arabidopsis roots. Upon *RNAi-PXY* induction, *PXY* levels dropped to 71% of wild type levels (**fig. S6F**) and a shift in *ANT* expression towards the xylem was observed (**Fig. 4, C and D; fig. S9E**), as the model predicted for the TDIF sequestration scenario.

Further corroboration of the dominance of TDIF sequestration came from the predicted differential responses of the two modelled mechanisms to increased TDIF levels emanating from the phloem. In the maximum HD-ZIP III ANT repression mechanism, a modelled increase in TDIF levels resulted in little change to the *ANT* expression domain (**Fig. 4E**). By contrast, for TDIF sequestration, expansion of the *ANT* expression domain towards the xylem was predicted (**Fig. 4F**). Supporting the sequestration model, TDIF overproduction *in planta* via phloem precursor-specific *pPEAR1:XVE>>CLE41* line resulted in expansion of *ANT* expression into the xylem (**Fig. 4, G and H; fig. S9F**). Thus, while both mechanisms may co-exist *in planta*, our modelling and experimentation suggest that the sequestration mechanism provides the dominant patterning constraint. Thus, the sequestration of TDIF by its PXY receptor effectively constrains TDIF mobility to the first few PXY expressing cells, enabling robust, spatially constrained patterning of the cambium stem cells. To confirm this behavior, wild type and two signaling-impaired versions of PXY-YFP, kinase-dead (K747E) (*40*) and truncated (ΔKD), were generated (**Fig. 5A**). As expected, only the wild type PXY-YFP version under its own promoter complemented *pxy,* indicating that the PXY-YFP fusion was functional (**fig. S11A**). Next, in wild type, we expressed each of the three PXY-YFP versions in phloem precursors, the source tissue of TDIF, using a *PEAR1* promoter (**fig. S11B**). In all three instances this resulted in a *pxy* phenotype (**Fig. 5B**). Since all three versions contain an intact TDIF binding domain, these results suggest TDIF was sequestered in the source tissue, prior to meeting the endogenous PXY receptors in the cambium stem cells. Our data indicate that sustained TDIF-PXY binding underlies this strong sequestration, even in the absence of a functional kinase domain. Translational reporters (*pPXY:gPXY-YFP* and *pPXY:cPXY-YFP*) displayed greater signal asymmetry between the stem cell daughters than the transcriptional version (*pPXY:erVenus*), with signal stronger in the xylem-side daughter (**Fig. 5, C and D**). As the phloem-side daughter cell experiences higher TDIF levels than the xylem-side daughter cell, one explanation for the asymmetry is that PXY-YFP with sequestered TDIF is subject to turnover. While the exact mechanism for sequestration requires further investigation, internalization and subsequent ligand and receptor degradation has been observed in other similar receptor kinases (*41–44*).

Discussion

Our combined experimental and modelling approach shows how PXY-mediated TDIF sequestration generates a robust patterning mechanism. By manipulating the auxin and TDIF gradients, we observed that the balance between the auxin gradient and the TDIF gradient determines the localization of the cambial stem cells as well as cambium size (*6*) **(Fig. 4G, fig. S12)**. We propose that this patterning mechanism flexibly enables adjustment of both phloem to xylem ratio and overall growth. A dominance of auxin localizes the cambium stem cell phloemward, leaving room for xylem cells to differentiate (*6*) **(fig. S12**). A TDIF dominated condition localizes the cambium stem cells xylemward, allowing phloem cells to differentiate, although the underlying connection to phloem differentiation remains to be studied. A strong combination of the two gradients allows for a larger cambium that sustains a larger total cell production (*45*) (**Fig. 4G; and fig. S12**). A WUSCHEL-related HOMEOBOX gene, *WOX4*, has been shown to act downstream of TDIF-PXY signaling (*46*, *47*). It remains to be studied how WOX4 is integrated with the signaling network described here, particularly because *WOX4* has a broader expression domain than *CAIL*s in the cambium (this paper and (*3*, *19*)). Also, it remains to be determined through which mechanism TDIF-PXY promotes *CAIL* transcription. Previously, we discovered a stem cell organizer at the xylem side of the cambium, defined by high levels of auxin signaling (*3*). Here, CAIL transcription factors were identified as the key stem cell factors operating downstream of the auxin-regulated PXY receptor. We elucidated how through sequestering TDIF ligands on the edge of the PXY gradient, the auxin-promoted organizer can induce CAILs and perform cambial stem cell patterning at a distance. Our findings suggest that like animals, plants use opposing morphogen gradients fine-tuned by sequestration-based feedback mechanisms to control precise positioning and cell fate decisions.

References

1. R. F. Evert, S. E. Eichhorn, *Esau's Plant Anatomy: Meristems, Cells, and Tissues of the Plant Body: Their Structure, Function, and Development: Third Edition* (2006).
2. P. R. Larson, *The Vascular Cambium: Development and Structure* (1994).
3. O. Smetana, R. Mäkilä, M. Lyu, A. Amiryousefi, F. Sánchez Rodríguez, M. F. Wu, A. Solé-Gil, M. Leal Gavarrón, R. Siligato, S. Miyashima, P. Roszak, T. Blomster, J. W. Reed, S. Broholm, A. P. Mähönen, High levels of auxin signalling define the stem-cell organizer of the vascular cambium. *Nature* **565**, 485–489 (2019).
4. D. Shi, I. Lebovka, V. Lopez-Salmeroń, P. Sanchez, T. Greb, Bifacial cambium stem cells generate xylem and phloem during radial plant growth. *Development* **146**, dev171355 (2019).
5. G. Bossinger, A. V. Spokevicius, Sector analysis reveals patterns of cambium differentiation in poplar stems. *J Exp Bot* **69**, 4339–4348 (2018).
6. R. Mäkilä, B. Wybouw, O. Smetana, L. Vainio, A. Solé-Gil, M. Lyu, L. Ye, X. Wang, R. Siligato, M. K. Jenness, A. S. Murphy, A. P. Mähönen, Gibberellins promote polar auxin transport to regulate stem cell fate decisions in cambium. *Nat Plants* **9**, 631–644 (2023).
7. T. J. Donner, I. Sherr, E. Scarpella, Regulation of preprocambial cell state acquisition by auxin signaling in Arabidopsis leaves. *Development* **136**, 3235–3246 (2009).
8. R. Ursache, S. Miyashima, Q. Chen, A. Vatén, K. Nakajima, A. Carlsbecker, Y. Zhao, Y. Helariutta, J. Dettmer, Tryptophan-dependent auxin biosynthesis is required for HD-ZIP III-mediated xylem patterning. *Development* **141**, 1250–1259 (2014).
9. K. Fisher, S. Turner, PXY, a Receptor-like Kinase Essential for Maintaining Polarity during Plant Vascular-Tissue Development. *Current Biology* **17**, 1061–1066 (2007).
10. R. Whitford, A. Fernandez, R. De Groodt, E. Ortega, P. Hilson, Plant CLE peptides from two distinct functional classes synergistically induce division of vascular cells. *Proc Natl Acad Sci U S A* **105**, 18625–18630 (2008).

11. J. Morita, K. Kato, T. Nakane, Y. Kondo, H. Fukuda, H. Nishimasu, R. Ishitani, O. Nureki, Crystal structure of the plant receptor-like kinase TDR in complex with the TDIF peptide. *Nat Commun* **7**, 12383 (2016).
12. J. P. Etchells, S. R. Turner, The PXY-CLE41 receptor ligand pair defines a multifunctional pathway that controls the rate and orientation of vascular cell division. *Development* **137**, 767–774 (2010).
13. Y. Hirakawa, H. Shinohara, Y. Kondo, A. Inoue, I. Nakanomyo, M. Ogawa, S. Sawa, K. Ohashi-Ito, Y. Matsubayashi, H. Fukuda, Non-cell-autonomous control of vascular stem cell fate by a CLE peptide/receptor system. *Proc Natl Acad Sci U S A* **105**, 15208–15213 (2008).
14. M. E. Smit, S. R. McGregor, H. Sun, C. Gough, A. M. Bågman, C. L. Soyars, J. T. Kroon, A. Gaudinier, C. J. Williams, X. Yang, Z. L. Nimchuk, D. Weijers, S. R. Turner, S. M. Brady, J. P. Etchells, A PXY-mediated transcriptional network integrates signaling mechanisms to control vascular development in Arabidopsis. *Plant Cell* **32**, 319–335 (2020).
15. J. S. Mudunkothge, B. A. Krizek, Three Arabidopsis AIL/PLT genes act in combination to regulate shoot apical meristem function. *Plant Journal* **71**, 108–21 (2012).
16. M. Aida, D. Beis, R. Heidstra, V. Willemsen, I. Blilou, C. Galinha, L. Nussaume, Y.-S. Noh, R. Amasino, B. Scheres, The *PLETHORA* Genes Mediate Patterning of the Arabidopsis Root Stem Cell Niche. *Cell* **119**, 109–120 (2004).
17. C. Galinha, H. Hofhuis, M. Luijten, V. Willemsen, I. Blilou, R. Heidstra, B. Scheres, PLETHORA proteins as dose-dependent master regulators of Arabidopsis root development. *Nature* **449**, 1053–1057 (2007).
18. A. P. Mähönen, K. Ten Tusscher, R. Siligato, O. Smetana, S. Díaz-Triviño, J. Salojärvi, G. Wachsman, K. Prasad, R. Heidstra, B. Scheres, PLETHORA gradient formation mechanism separates auxin responses. *Nature* **515**, 125–129 (2014).
19. J. Zhang, G. Eswaran, J. Alonso-Serra, M. Kucukoglu, J. Xiang, W. Yang, A. Elo, K. Nieminen, T. Damén, J.-G. Joung, J.-Y. Yun, J.-H. Lee, L. Ragni, P. Barbier de Reuille, S. E. Ahnert, J.-Y. Lee, A. P. Mähönen, Y. Helariutta, Transcriptional regulatory framework for vascular cambium development in Arabidopsis roots. *Nat Plants* **5**, 1033–1042 (2019).
20. R. S. Randall, S. Miyashima, T. Blomster, J. Zhang, A. Elo, A. Karlberg, J. Immanen, K. Nieminen, J. Y. Lee, T. Kakimoto, K. Blajecka, C. W. Melnyk, A. Alcasabas, C. Forzani, M. Matsumoto-Kitano, A. P. Mähönen, R. Bhalerao, W. Dewitte, Y. Helariutta, J. A. H. Murray, AINTEGUMENTA and the D-type cyclin CYCD3;1 regulate root secondary growth and respond to cytokinins. *Biol Open* **4**, 1229–1236 (2015).
21. S. Nole-Wilson, T. L. Tranby, B. A. Krizek, *AINTEGUMENTA-like* (*AIL*) genes are expressed in young tissues and may specify meristematic or division-competent states. *Plant Mol Biol* **57**, 613–28 (2005).
22. K. Prasad, S. P. Grigg, M. Barkoulas, R. K. Yadav, G. F. Sanchez-Perez, V. Pinon, I. Blilou, H. Hofhuis, P. Dhonukshe, C. Galinha, A. P. Mähönen, W. H. Muller, S. Raman, A. J. Verkleij, B. Snel, G. V. Reddy, M. Tsiantis, B. Scheres, Arabidopsis PLETHORA transcription factors control phyllotaxis. *Current Biology* **21**, 1123–1128 (2011).

23. M. Kerstens, V. Hesen, K. Yalamanchili, A. Bimbo, S. Grigg, D. Opdenacker, T. Beeckman, R. Heidstra, V. Willemsen, Nature and nurture: Genotype-dependent differential responses of root architecture to agar and soil environments. *Genes (Basel)* **12**, 1028 (2021).
24. B. A. Krizek, AINTEGUMENTA and AINTEGUMENTA-LIKE6 act redundantly to regulate arabidopsis floral growth and patterning. *Plant Physiol* **150**, 1916–29 (2009).
25. X. Wang, L. Ye, M. Lyu, R. Ursache, A. Löytynoja, A. P. Mähönen, An inducible genome editing system for plants. *Nat Plants* **6**, 766–772 (2020).
26. R. Siligato, X. Wang, S. R. Yadav, S. Lehesranta, G. Ma, R. Ursache, I. Sevilem, J. Zhang, M. Gorte, K. Prasad, M. Wrzaczek, R. Heidstra, A. Murphy, B. Scheres, A. P. Mähönen, Multisite gateway-compatible cell type-specific gene-inducible system for plants. *Plant Physiol* **170**, 627–641 (2016).
27. J. R. Wendrich, B. Yang, N. Vandamme, K. Verstaen, W. Smet, C. Van de Velde, M. Minne, B. Wybouw, E. Mor, H. E. Arents, J. Nolf, J. Van Duyse, G. Van Isterdael, S. Maere, Y. Saeys, B. De Rybel, Vascular transcription factors guide plant epidermal responses to limiting phosphate conditions. *Science (1979)* **370**, eaay4970 (2020).
28. P. Roszak, J. Heo, B. Blob, K. Toyokura, Y. Sugiyama, M. A. de Luis Balaguer, W. W. Y. Lau, F. Hamey, J. Cirrone, E. Madej, A. M. Bouatta, X. Wang, M. Guichard, R. Ursache, H. Tavares, K. Verstaen, J. Wendrich, C. W. Melnyk, Y. Oda, D. Shasha, S. E. Ahnert, Y. Saeys, B. De Rybel, R. Heidstra, B. Scheres, G. Grossmann, A. P. Mähönen, P. Denninger, B. Göttgens, R. Sozzani, K. D. Birnbaum, Y. Helariutta, Cell-by-cell dissection of phloem development links a maturation gradient to cell specialization. *Science (1979)* **374**, eaba5531 (2021).
29. T. Q. Zhang, Y. Chen, J. W. Wang, A single-cell analysis of the Arabidopsis vegetative shoot apex. *Dev Cell* **56**, 1056-1074.e8 (2021).
30. Y. Zhu, D. Song, R. Zhang, L. Luo, S. Cao, C. Huang, J. Sun, J. Gui, L. Li, A xylem-produced peptide PtrCLE20 inhibits vascular cambium activity in Populus. *Plant Biotechnol J* **18**, 195–206 (2020).
31. F. P. Hartmann, C. B. K. Rathgeber, É. Badel, M. Fournier, B. Moulia, Modelling the spatial crosstalk between two biochemical signals explains wood formation dynamics and tree-ring structure. *J Exp Bot* **72**, 1727–1737 (2021).
32. I. Lebovka, B. H. Mele, X. Liu, A. Zakieva, T. Schlamp, N. R. Gursanscky, R. M. H. Merks, R. Großeholz, T. Greb, Computational modeling of cambium activity provides a regulatory framework for simulating radial plant growth. *Elife* **12**, e66627 (2023).
33. K. S. Bagdassarian, J. P. Etchells, N. S. Savage, A mathematical model integrates diverging PXY and MP interactions in cambium development. *In Silico Plants* **5**, diad003 (2023).
34. F. P. Hartmann, C. B. K. Rathgeber, É. Badel, M. Fournier, B. Moulia, Modelling the spatial crosstalk between two biochemical signals explains wood formation dynamics and tree-ring structure. *J Exp Bot* **72**, 1727–1737 (2021).
35. N. Yamaguchi, M. F. Wu, C. M. Winter, M. C. Berns, S. Nole-Wilson, A. Yamaguchi, G. Coupland, B. A. Krizek, D. Wagner, A Molecular Framework for Auxin-Mediated Initiation of Flower Primordia. *Dev Cell* **24**, 271–282 (2013).

36. R. Zhong, Z. H. Ye, IFL1, a gene regulating interfascicular fiber differentiation in Arabidopsis, encodes a homeodomain-leucine zipper protein. *Plant cell* **11**, 2139–52 (1999).
37. K. Ohashi-Ito, M. Kubo, T. Demura, H. Fukuda, Class III homeodomain leucine-zipper proteins regulate xylem cell differentiation. *Plant Cell Physiol* **46**, 1646–1656 (2005).
38. A. Carlsbecker, J. Y. Lee, C. J. Roberts, J. Dettmer, S. Lehesranta, J. Zhou, O. Lindgren, M. A. Moreno-Risueno, A. Vatén, S. Thitamadee, A. Campilho, J. Sebastian, J. L. Bowman, Y. Helariutta, P. N. Benfey, Cell signalling by microRNA165/6 directs gene dose-dependent root cell fate. *Nature* **465**, 316–321 (2010).
39. S. Miyashima, P. Roszak, I. Sevilem, K. Toyokura, B. Blob, J. ok Heo, N. Mellor, H. Help-Rinta-Rahko, S. Otero, W. Smet, M. Boekschoten, G. Hooiveld, K. Hashimoto, O. Smetana, R. Siligato, E. S. Wallner, A. P. Mähönen, Y. Kondo, C. W. Melnyk, T. Greb, K. Nakajima, R. Sozzani, A. Bishopp, B. De Rybel, Y. Helariutta, Mobile PEAR transcription factors integrate positional cues to prime cambial growth. *Nature* **565**, 490–494 (2019).
40. Y. Kondo, T. Ito, H. Nakagami, Y. Hirakawa, M. Saito, T. Tamaki, K. Shirasu, H. Fukuda, Plant GSK3 proteins regulate xylem cell differentiation downstream of TDIF–TDR signalling. *Nat Commun* **5**, 3504 (2014).
41. S. Robatzek, D. Chinchilla, T. Boller, Ligand-induced endocytosis of the pattern recognition receptor FLS2 in Arabidopsis. *Genes Dev* **20**, 537–542 (2006).
42. Z. L. Nimchuk, P. T. Tarr, C. Ohno, X. Qu, E. M. Meyerowitz, Plant stem cell signaling involves ligand-dependent trafficking of the CLAVATA1 receptor kinase. *Current Biology* **21**, 345–352 (2011).
43. M. Mbengue, G. Bourdais, F. Gervasi, M. Beck, J. Zhou, T. Spallek, S. Bartels, T. Boller, T. Ueda, H. Kuhn, S. Robatzek, Clathrin-dependent endocytosis is required for immunity mediated by pattern recognition receptor kinases. *Proc Natl Acad Sci U S A* **113**, 11034–11039 (2016).
44. F. A. Ortiz-Morea, D. V. Savatin, W. Dejonghe, R. Kumar, Y. Luo, M. Adamowski, J. Den Van Begin, K. Dressano, G. P. De Oliveira, X. Zhao, Q. Lu, A. Madder, J. Friml, D. S. de Moura, E. Russinova, Danger-associated peptide signaling in Arabidopsis requires clathrin. *Proc Natl Acad Sci U S A* **113**, 11028–11033 (2016).
45. J. P. Etchells, L. S. Mishra, M. Kumar, L. Campbell, S. R. Turner, Wood Formation in Trees Is Increased by Manipulating PXY-Regulated Cell Division. *Current Biology* **25**, 1050–1055 (2015).
46. Y. Hirakawa, Y. Kondo, H. Fukuda, TDIF peptide signaling regulates vascular stem cell proliferation via the *WOX4* homeobox gene in Arabidopsis. *Plant Cell* **22**, 2618–2629 (2010).
47. S. Suer, J. Agusti, P. Sanchez, M. Schwarz, T. Greb, WOX4 imparts auxin responsiveness to cambium cells in Arabidopsis. *Plant Cell* **23**, 3247–3259 (2011).
48. H. Hofhuis, M. Laskowski, Y. Du, K. Prasad, S. Grigg, V. Pinon, B. Scheres, Phyllotaxis and rhizotaxis in Arabidopsis are modified by three plethora transcription factors. *Current Biology* **23**, 956–962 (2013).
49. K. Yamagishi, K. Tatematsu, R. Yano, J. Preston, S. Kitamura, H. Takahashi, P. McCourt, Y. Kamiya, E. Nambara, CHOTTO1, a double AP2 domain protein of

Arabidopsis thaliana, regulates germination and seedling growth under excess supply of glucose and nitrate. *Plant Cell Physiol* **50**, 330–40 (2009).
50. R. Zhong, C. Lee, J. Zhou, R. L. McCarthy, Z.-H. Ye, A Battery of Transcription Factors Involved in the Regulation of Secondary Cell Wall Biosynthesis in Arabidopsis. *Plant Cell* **20**, 2763–2782 (2008).
51. S. Otero, I. Gildea, P. Roszak, Y. Lu, V. Di Vittori, M. Bourdon, L. Kalmbach, B. Blob, J. ok Heo, F. Peruzzo, T. Laux, A. R. Fernie, H. Tavares, Y. Helariutta, A root phloem pole cell atlas reveals common transcriptional states in protophloem-adjacent cells. *Nat Plants* **8**, 954–970 (2022).
52. R. Grützner, P. Martin, C. Horn, S. Mortensen, E. J. Cram, C. W. T. Lee-Parsons, J. Stuttmann, S. Marillonnet, High-efficiency genome editing in plants mediated by a *Cas9* gene containing multiple introns. *Plant Commun* **2**, 100135 (2021).
53. A. P. Mähönen, M. Bonke, L. Kauppinen, M. Riikonen, P. N. Benfey, Y. Helariutta, A novel two-component hybrid molecule regulates vascular morphogenesis of the Arabidopsis root. *Genes Dev* **14**, 2938–43 (2000).
54. R. Kumar, Y. Ichihashi, S. Kimura, D. H. Chitwood, L. R. Headland, J. Peng, J. N. Maloof, N. R. Sinha, A High-Throughput Method for Illumina RNA-Seq Library Preparation. *Front Plant Sci* **3**, doi.org/10.3389/fpls.2012.00202 (2012).
55. M. P. A. Davis, S. van Dongen, C. Abreu-Goodger, N. Bartonicek, A. J. Enright, Kraken: A set of tools for quality control and analysis of high-throughput sequence data. *Methods* **63**, 41–49 (2013).
56. D. Kim, G. Pertea, C. Trapnell, H. Pimentel, R. Kelley, S. L. Salzberg, TopHat2: accurate alignment of transcriptomes in the presence of insertions, deletions and gene fusions. *Genome Biol* **14**, R36 (2013).
57. S. Anders, P. T. Pyl, W. Huber, HTSeq-A Python framework to work with high-throughput sequencing data. *Bioinformatics* **31**, 166–169 (2015).
58. M. I. Love, W. Huber, S. Anders, Moderated estimation of fold change and dispersion for RNA-seq data with DESeq2. *Genome Biol* **15**, 550 (2014).
59. L. Ye, X. Wang, M. Lyu, R. Siligato, G. Eswaran, L. Vainio, T. Blomster, J. Zhang, A. P. Mähönen, Cytokinins initiate secondary growth in the Arabidopsis root through a set of *LBD* genes. *Current Biology* **31**, 3365-3373.e7 (2021).
60. M. D. Robinson, D. J. McCarthy, G. K. Smyth, edgeR: A Bioconductor package for differential expression analysis of digital gene expression data. *Bioinformatics* **26**, 139–140 (2009).
61. N. Idänheimo, A. Gauthier, J. Salojärvi, R. Siligato, M. Brosché, H. Kollist, A. P. Mähönen, J. Kangasjärvi, M. Wrzaczek, The *Arabidopsis thaliana* cysteine-rich receptor-like kinases CRK6 and CRK7 protect against apoplastic oxidative stress. *Biochem Biophys Res Commun* **445**, 457–462 (2014).
62. R. Ursache, T. G. Andersen, P. Marhavý, N. Geldner, A protocol for combining fluorescent proteins with histological stains for diverse cell wall components. *Plant Journal* **93**, 399–412 (2018).
63. E. Kotogány, D. Dudits, G. V. Horváth, F. Ayaydin, A rapid and robust assay for detection of S-phase cell cycle progression in plant cells and tissues by using ethynyl deoxyuridine. *Plant Methods* **6**, 5 (2010).

64. J. Schindelin, I. Arganda-Carreras, E. Frise, V. Kaynig, M. Longair, T. Pietzsch, S. Preibisch, C. Rueden, S. Saalfeld, B. Schmid, J.-Y. Tinevez, D. J. White, V. Hartenstein, K. Eliceiri, P. Tomancak, A. Cardona, Fiji: an open-source platform for biological-image analysis. *Nat Methods* **9**, 676–682 (2012).
65. K. J. Livak, T. D. Schmittgen, Analysis of relative gene expression data using real-time quantitative PCR and the 2-ΔΔCT method. *Methods* **25**, 402–408 (2001).
66. A. Cruz-Ramírez, S. Díaz-Triviño, I. Blilou, V. A. Grieneisen, R. Sozzani, C. Zamioudis, P. Miskolczi, J. Nieuwland, R. Benjamins, P. Dhonukshe, J. Caballero-Pérez, B. Horvath, Y. Long, A. P. Mähönen, H. Zhang, J. Xu, J. A. H. Murray, P. N. Benfey, L. Bako, A. F. M. Marée, B. Scheres, A bistable circuit involving SCARECROW-RETINOBLASTOMA integrates cues to inform asymmetric stem cell division. *Cell* **150** (2012).
67. J. Raspopovic, L. Marcon, L. Russo, J. Sharpe, Digit patterning is controlled by a Bmp-Sox9-Wnt Turing network modulated by morphogen gradients. *Science (1979)* **345** (2014).
68. Y. Ito, I. Nakanomyo, H. Motose, K. Iwamoto, S. Sawa, N. Dohmae, H. Fukuda, Dodeca-CLE as peptides as suppressors of plant stem cell differentiation. *Science (1979)* **313** (2006).
69. O. Hosoya, S. Chono, Y. Saso, K. Juni, K. Morimoto, T. Seki, Determination of diffusion coefficients of peptides and prediction of permeability through a porous membrane. *Journal of Pharmacy and Pharmacology* **56**, 1501–1507 (2004).
70. J. F. Torres, A. Komiya, J. Okajima, S. Maruyama, Measurement of the Molecular Mass Dependence of the Mass Diffusion Coefficient in Protein Aqueous Solutions. *Defect and Diffusion Forum* **326–328**, 452–458 (2012).
71. J. Lee, S. H. Park, S. Cavagnero, J. H. Lee, High-Resolution Diffusion Measurements of Proteins by NMR under Near-Physiological Conditions. *Anal Chem* **92**, 5073–5081 (2020).
72. N. Hirota, Y. Kumaki, T. Narita, J. P. Gong, Y. Osada, Effect of charge on protein diffusion in hydrogels. *Journal of Physical Chemistry B* **104**, 9898–9903 (2000).
73. E. M. Kramer, N. L. Frazer, T. I. Baskin, Measurement of diffusion within the cell wall in living roots of Arabidopsis thaliana. *J Exp Bot* **58** (2007).

Acknowledgements

We thank Viola Willemsen, Kalika Prasad and Beth Krizek for providing us published material, and Jan Traas for providing the unpublished entry clone containing the *AIL6/PLT3* promoter; Julia Vainonen for help in protein work; and Ykä Helariutta for providing feedback on the manuscript. Confocal imaging was performed with help and using equipment of the Light Microscopy Unit (LMU), University of Helsinki. Special thanks to Mikko Herpola and Filipa Alexandra Silva for technical help.

Funding: This work was supported by the Academy of Finland (grant numbers 316544 and 346141 to G.E., X.X.Z., R.M., B.W., L.V., M.L.G., T.B., O.S. and A.P.M.; 343527 to A.P; 326036, 347130, 353537, 346141 to M.K.T), European Research Council (ERC-CoG CORKtheCAMBIA agreement 819422 to G.E., X.X.Z., H.I., J.L.O., R.M., B.W., X.W., J.Z. and A.P.M.), University of Helsinki (ILS to G.E., and DPPS to R.M. and L.V.), EMBO (Postdoctoral Fellowship ALTF 1235-2020 to X.X.Z., ALTF 128-2020 to H.I.), JSPS (Overseas Research Fellowship to H.I), BBSRC (grant BB/V008129/1 to J.P.E., J.H., and A.P.M.), European Commission (Marie Skłodowska-Curie Fellowship 329978 to J.P.E and S.B.), Dutch Organization for Scientific Research (Nederlandse Organisatie voor Wetenschappelijk Onderzoek, NWO, grant 864.14.003 to J.P.R and K.t.T, and OCENW.GROOT.2019.017 for B.P.J). For the purpose of open access, the authors have applied a Creative Commons Attribution (CC BY) license to any Author Accepted Manuscript version arising.

Author contributions: K.t.T., J.P.E. and A.P.M. conceived the project; G.E., X.X.Z., H.I., J.L.O., O.S., S.B., M.K.T, J.P.E. and A.P.M., designed the experiments; G.E., X.X.Z., J.H., H.I., J.L.O., R.M., B.W., J.Z., M.K.T. and J.P.E. performed the experiments; J.P.R., K.t.T. designed and performed the computational modelling, B.P.J. and K.t.T. performed the mathematical model analysis; L.V. created the circle-unwrapping projections; A.P. performed statistical analysis; X.W. generated genetic material; M.L.G. provided preliminary data; T.B. and D.D. assisted with RNA-seq analysis; G.E., X.X.Z., J.P.R, K.t.T., J.P.E. and A.P.M. wrote the paper with input from all authors.

Competing interests: The authors declare no competing interests.

Data and materials availability: All lines involved in this study are available upon reasonable request from the corresponding authors. Gene accession numbers are as follows: *ANT*, AT4G37750; *APL,* AT1G79430; *AtHB8*, AT4G32880; *CLE41*, AT3G24770; *MIR165A*, AT1G01183; *PEAR1*, AT2G37590; *PLT1*, AT3G20840; *PLT2*, AT1G51190; *PLT3*, AT5G10510; *PLT4*, AT5G17430; *PLT5*, AT5G57390; *PLT7*, AT5G65510; *PXY/TDR*, AT5G61480; *VND6*, AT5G62380; *PEX4/UBC21* AT5G25760. The data of transcriptomes of *pxy* and *35S:CLE41* is available on GEO (accession number GSE119872). The data of transcriptome of *35S:XVE>>PLT5-tagRFP* is available on GEO (accession number GSE264403). The source codes for the different models described here is available on https://tbb.bio.uu.nl/khwjtuss/cambium as well as in GitHub (31).

Supplementary Materials

This pdf includes:

Experimental Materials and Methods

Modelling Methods

Tables S1 to S6

Figs. S1 to S12

References (48–73)

Other Supplementary Materials for this manuscript includes the following:

Data S1 (Source and RNA-seq data)

Data S2 (Primers, constructs, seeds)

Figures and Figure legends

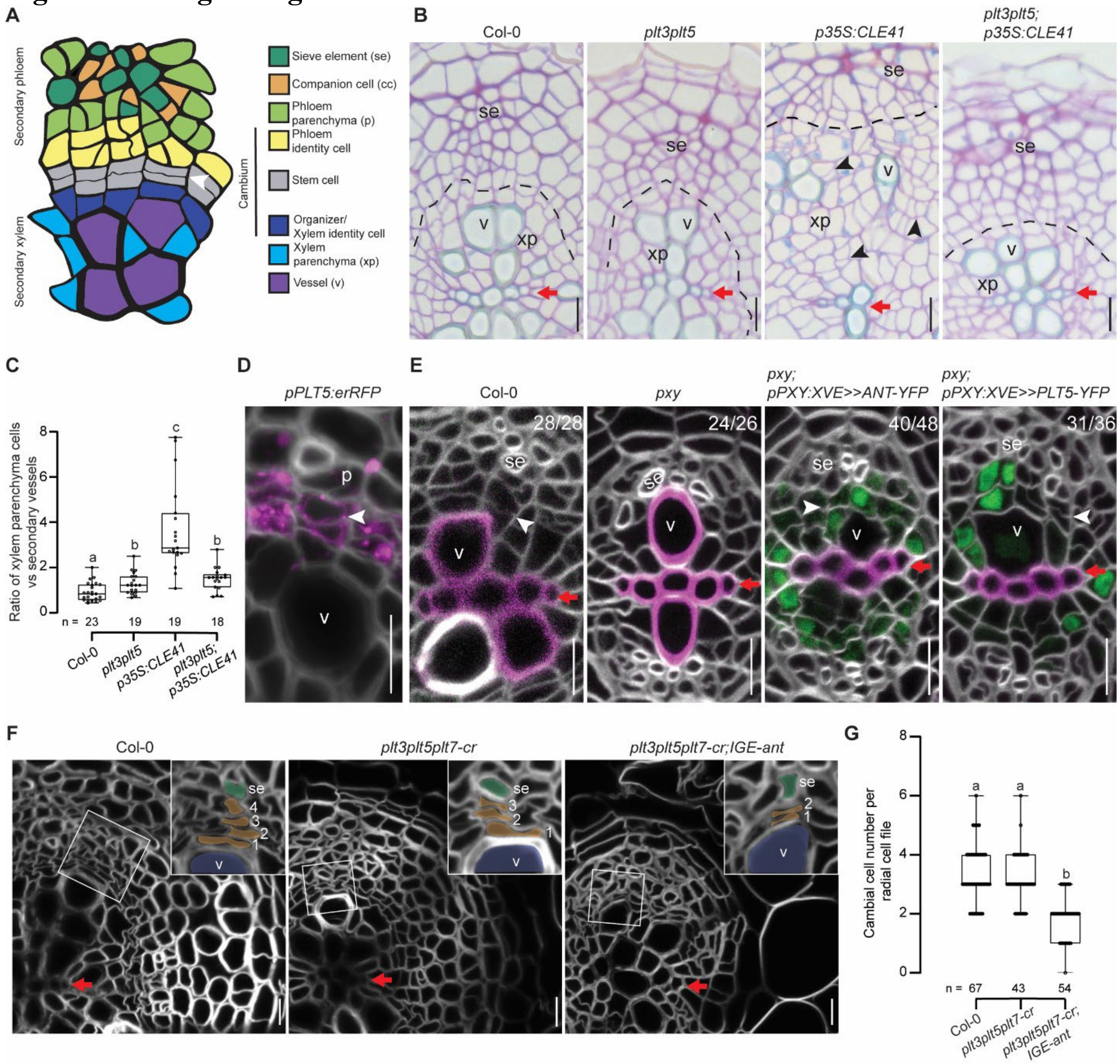

Fig. 1. CAILs operate downstream of TDIF-PXY to maintain cambial stem cells
(A) Schematic representation of 14-day-old wild-type (Col-0) cross section of *Arabidopsis* root. **(B)** Plastic cross-sections of 14-day-old Col-0, *plt3plt5*, *p35S:CLE41*, and *plt3plt5;p35S:CLE41* roots. **(C)** Ratio between numbers of xylem parenchyma cells and secondary vessels. **(D)** Confocal cross-section of 14-day-old *pPLT5:erRFP* root. (**E**) Confocal root cross-sections of 10-day-old Col-0, *pxy*, and 5-day-old *pPXY:XVE>>ANT-YFP* and *pPXY:XVE>>PLT5-YFP* lines induced for 5 days in *pxy* background. The numbers in the top right corner of subpanels represent the frequency of the observed phenotype. Cell walls were stained with SR2200 (grey), and lignified cell walls were stained with 0.1% basic fuchsin (magenta). **(F)** Confocal root cross-sections of 15-d-old Col-0, *plt3plt5plt7-cr* and *plt3plt5plt7-cr;IGE-ant*. The false coloring in the inset highlights the cambial cells (brown) used for the quantification in panel (G). **(G)** Boxplot showing the cambial cell number per cell file between differentiated vessels and sieve elements, as visualized in the insets of panel (F). Letters in (C and G) indicate significant differences using Kruskal-Wallis test

followed by Dunn's post-hoc multiple comparisons with Bonferroni adjusted *p-values* ($p < 0.05$). White arrowheads mark stem cell divisions, black arrowheads mark ectopic divisions, red arrows mark the primary xylem axis, and the black dashed line marks the position of the cambium. Phloem (p), sieve element (se), xylem vessels (v), and xylem parenchyma (xp). Scale bars, 10 µm (B, D, E, and F).

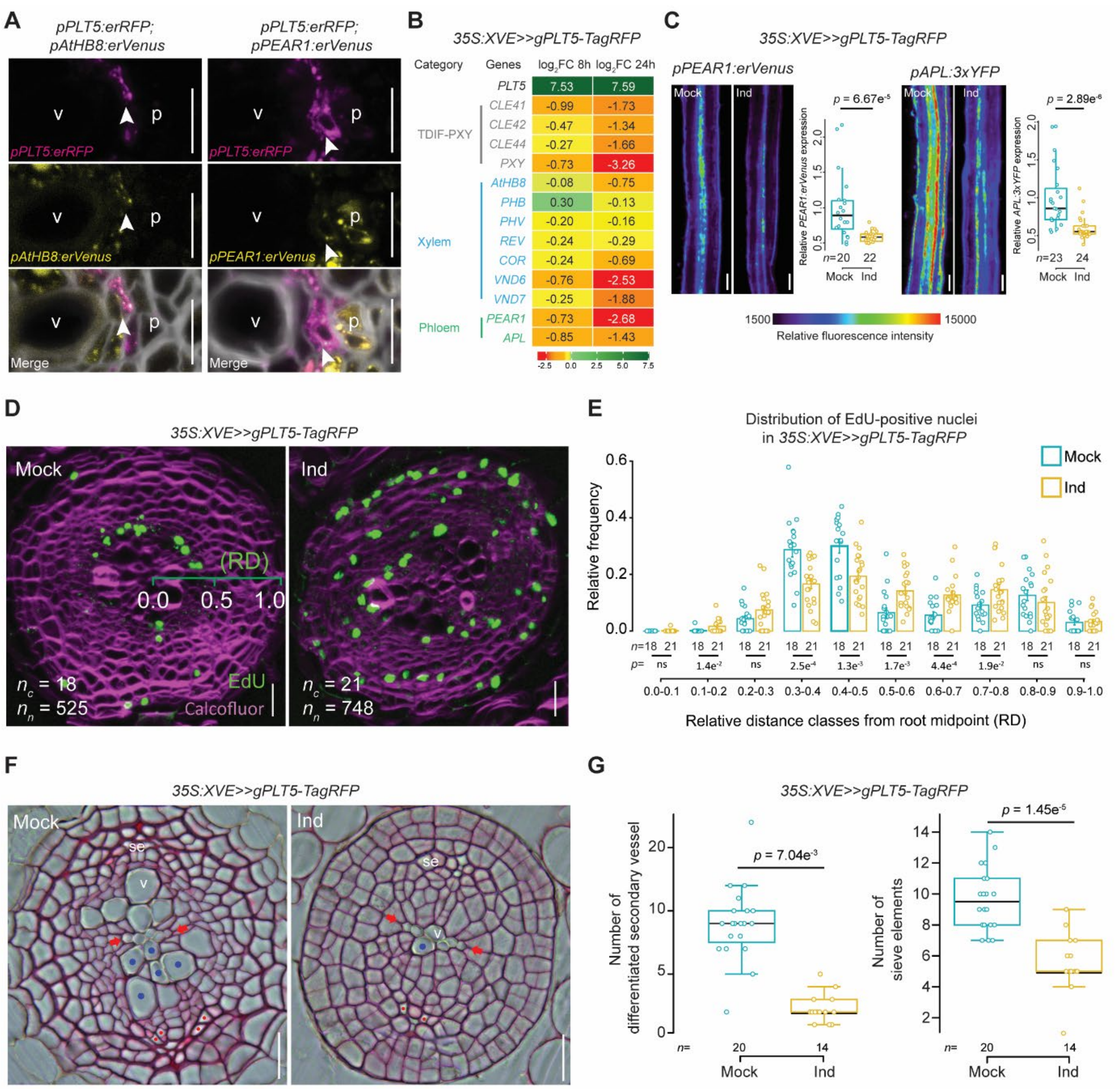

Fig. 2. PLT5 promote cambial cell divisions and inhibit secondary xylem and phloem differentiation

(A) Confocal cross-sections of 12-day-old *pPLT5:erRFP pATHB8:erVenus* (left) and *pPLT5:erRFP pPEAR1:erVenus* (right) double marker lines. **(B)** Heatmap showing normalized $\log_2$FoldChange (FC) as determined by RNA-seq, upon induction of *PLT5* over-expression for 8 hours and 24 hours. **(C)** Lateral view of 8-day-old *35S:XVE>>gPLT5-TagRFP* roots with early (*pPEAR1:erVenus*) and late (*pAPL:3xYFP)* phloem markers after a 2-day induction. Box plots show quantification of relative fluorescent signal intensity. **(D)** Confocal cross-sections of

35S:XVE>>gPLT5-TagRFP after 2-day induction with 16 hours of EdU (green) incorporation (in 12-day-old roots) to detect S-phase nuclei. **(E)** Barplot of relative distribution (RD) of EdU-positive nuclei along the radial root axis in panel (D) (primary xylem axis = 0; root surface = 1). Scale shown on green on the mock panel; n_c = number of cross-sections analyzed; n_n = total number of nuclei. **(F)** Cross-sections of *35S:XVE>>gPLT5-TagRFP* after 4-day induction (in 8-day-old plants). Red dots indicate the sieve elements and blue dots indicate vessels in the lower half of the root. **(G)** Quantification of secondary xylem vessel and sieve element numbers. In (E) error bars show mean ± standard error. Significant differences were calculated using two-tailed student t-test for each relative distance class (ns = $p>0.05$). In (C) and (G) significant differences between mock and induced conditions were calculated using two-sided Wilcoxon-Mann-Whitney test. White arrowheads mark recent cell division, red arrows mark the primary xylem axis. Vessels (v), phloem (p), sieve elements (se). Scale bars, 10 µm (A), 100 µm (C), and 50 µm (D and F).

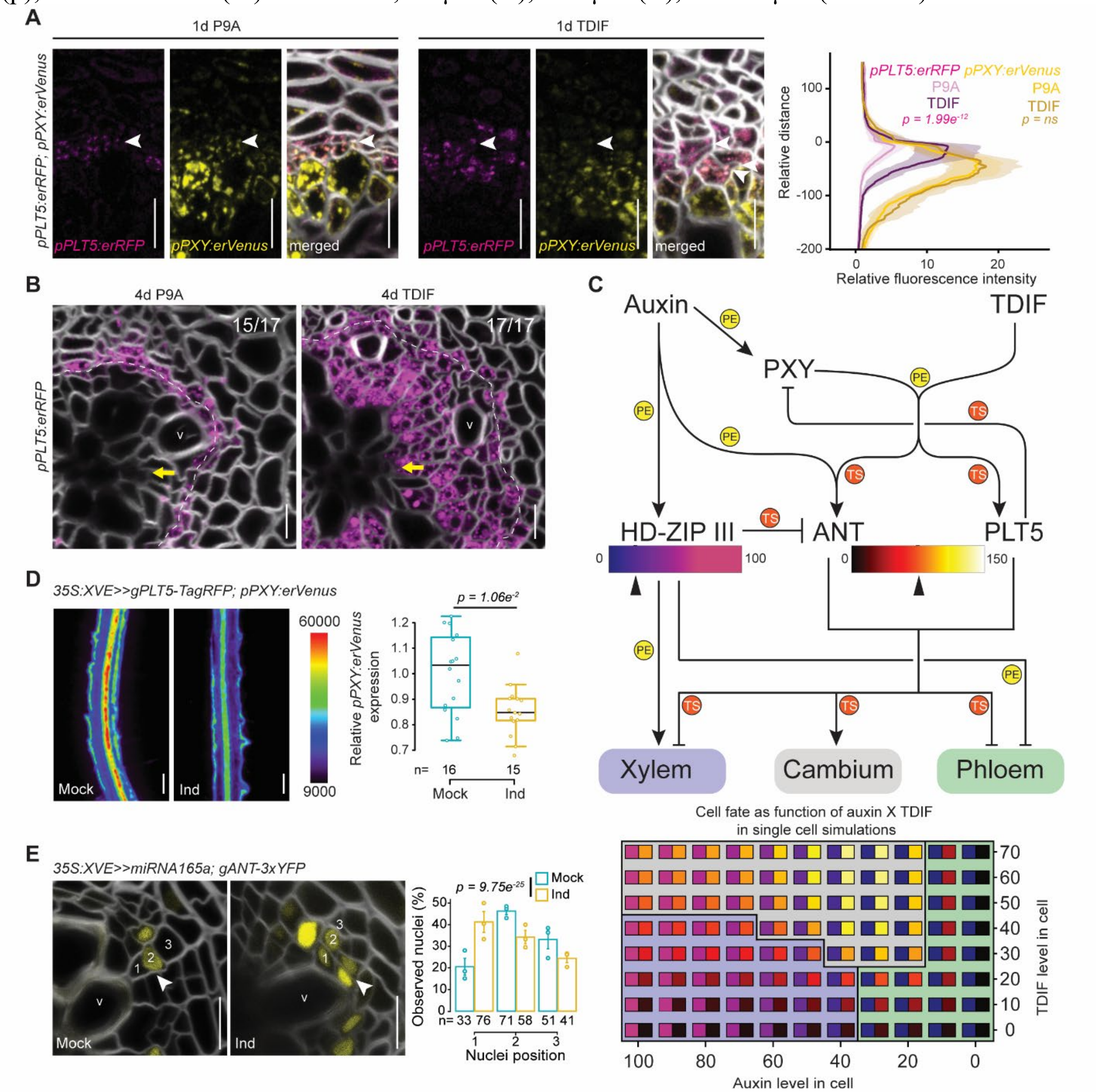

Fig. 3. Regulatory network defining cambium, xylem and phloem

(A) Confocal cross-sections of roots carrying *pPLT5:erRFP* and *pPXY:erVenus* double markers in 15-day-old plants after 24 hours of P9A$_{(n=18)}$ (control) or TDIF$_{(n=16)}$ treatment. P9A is a mutant version of TDIF, incapable to bind PXY. While wild-type or P9A-treated cambia typically have a single cell in every radial cell file that has undergone a recent division (thin cell wall, marked with white arrowhead), TDIF-treated cambium have additional, ectopic divisions in the xylem domain (multiple arrowheads). Quantification of *pPLT5:erRFP* expression (right) shows increases and a shift towards xylem. (ns = p>0.05). **(B)** Confocal cross-sections of *pPLT5:erRFP* expression after 4-day TDIF treatment (in 13-day-old root). White dashed line marks the cambium. Yellow arrows mark the primary xylem axis. **(C)** Modelling cambial cell fate decision making under different combinations of auxin and TDIF concentrations. Top panel: Interaction network underlying cambial cell fate decision making incorporated in the model. PE (yellow) refers to 'Published Elsewhere', TS (orange) refers to 'This Study'. Supporting details with references are listed in (fig. S7). Bottom panel: Fate map of a cambial cell exposed to different auxin-TDIF combinations. For each Auxin-TDIF combination, the left square within the rectangle shows the HD-ZIP III level at steady state and the right square shows the summed PLT5+ANT level at steady state. The black arrowheads on the color bars in the top panel show the threshold levels. Applied cell fate thresholds are as follows: If PLT5+ANT >= 75 cambial identity (grey); if PLT5+ANT < 75 and HD-ZIP III >= 30 xylem identity (blue); if HD-ZIP III < 30 phloem identity (green). Parameter settings are described in the Modelling Methods (maximum HD-ZIP III ANT repression settings). While in the parameter sweep, TDIF levels were varied between 0 and 100, here TDIF levels between 0 and 70 are shown to focus on the key region in terms of cell fate acquisition. **(D)** Lateral view of *35S:XVE>>gPLT5-TagRFP;pPXY:erVenus* 8-day-old plants after a 2-day induction with quantification of relative fluorescent signal intensity. Significant difference between mock and induced condition was calculated using two-sided Wilcoxon-Mann-Whitney test. **(E)** Confocal cross-sections of *35S:XVE>>miRNA165a;gANT-3xYFP* after 2-day induction (in 12-day-old plants). Quantification of positional expression of *gANT-3xYFP* in cambium. Barplot showing position of *gANT-3xYFP*-positive nuclei. In (E) categorical distribution was tested using a chi-square test. Data points represent the mean of each biological repeat. White arrowheads mark recent cell divisions. Vessels (v). Scale bars, 10 µm (A, B and E), 200 µm (D).

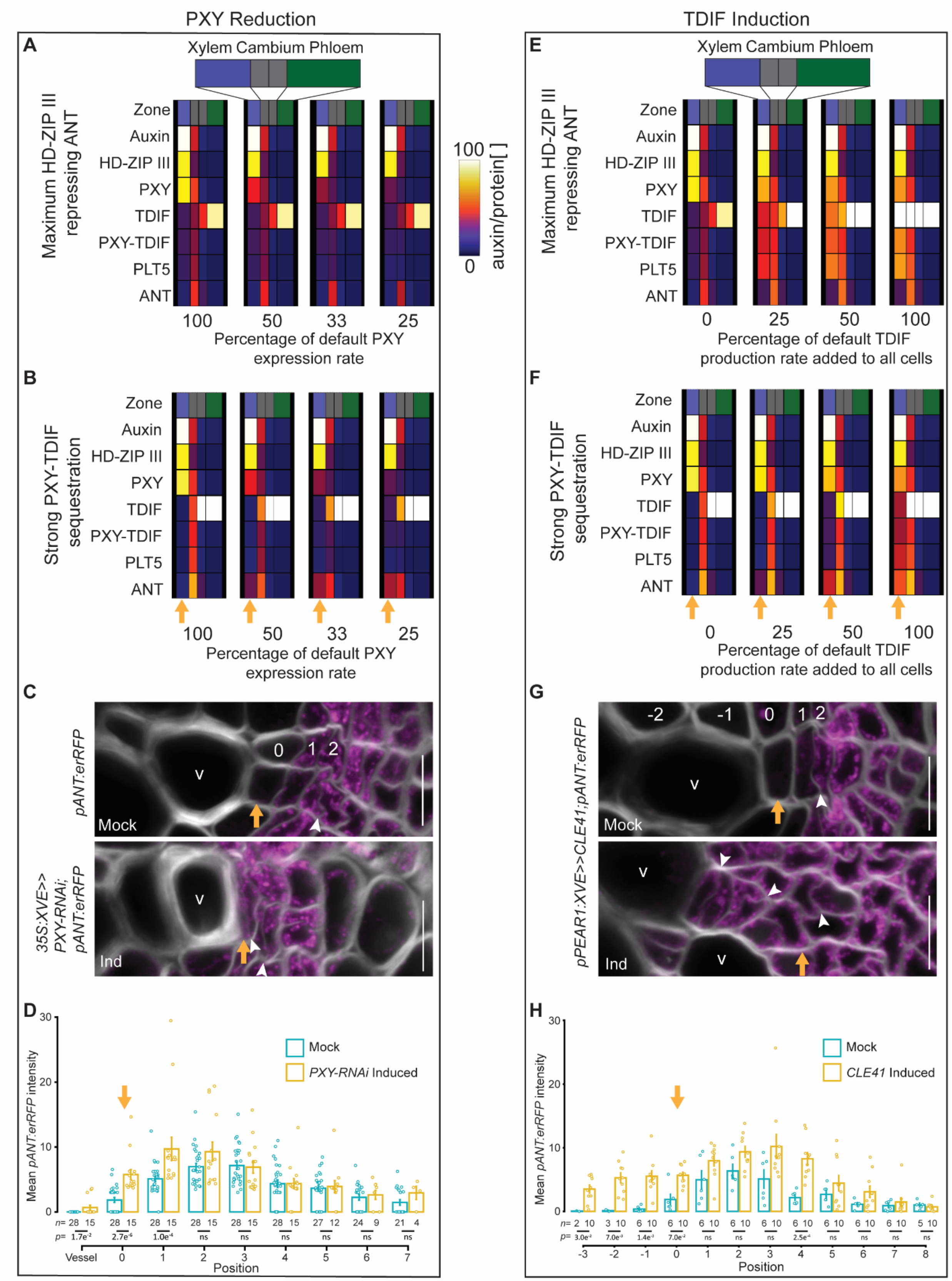

Fig. 4. TDIF sequestration ensures a narrow *ANT* expression domain

(A, B, E and **F)** Comparison between the maximum HD-ZIP III repression parameter regime (A and E) and strong sequestering effect of PXY on TDIF (B and F). Heatmap shows the gene expression level. Parameter settings are described in the Modelling Methods (maximum HD-ZIP III repression versus strong sequestration settings). (A and B) Effect of reducing *PXY* expression rate in the two regimes. In (A) this leads to overall reduction of *ANT* expression, while in (B) it leads to a xylemward shift of *ANT* expression. (E and F) Responses of the two regimes to incorporating various TDIF production rates, expressed as percentage of default phloem production rate, in all cells. Maximum HD-ZIP III repression safeguards the xylem from ANT expression, while in the strong sequestering regime *ANT* is expressed in the xylem. **(C)** Confocal cross-sections of *35S:XVE>>PXY-RNAi; pANT:erRFP* after 2-day induction (in 12-day-old plants). **(D)** Quantification of mean *pANT:erRFP* intensity position. **(G)** Confocal cross-sections *pPEAR1:XVE>>CLE41;pANT:erRFP* after 2-day induction (in 12-day-old plants). **(H)** Quantification of mean *pANT:erRFP* intensity position. In (D and H) error bars show ± standard error. Significance was determined using two-sided Wilcoxon-Mann-Whitney test, (ns = p>0.05). White arrowheads mark recent cell divisions, orange arrows mark the position of xylem identity cells before induction. Xylem identity cell was numbered as position 0, towards xylem (positions -1, -2 and -3) and towards phloem (positions 1, 2…, and 8). Vessels (v). Scale bars 10 µm (C and G).

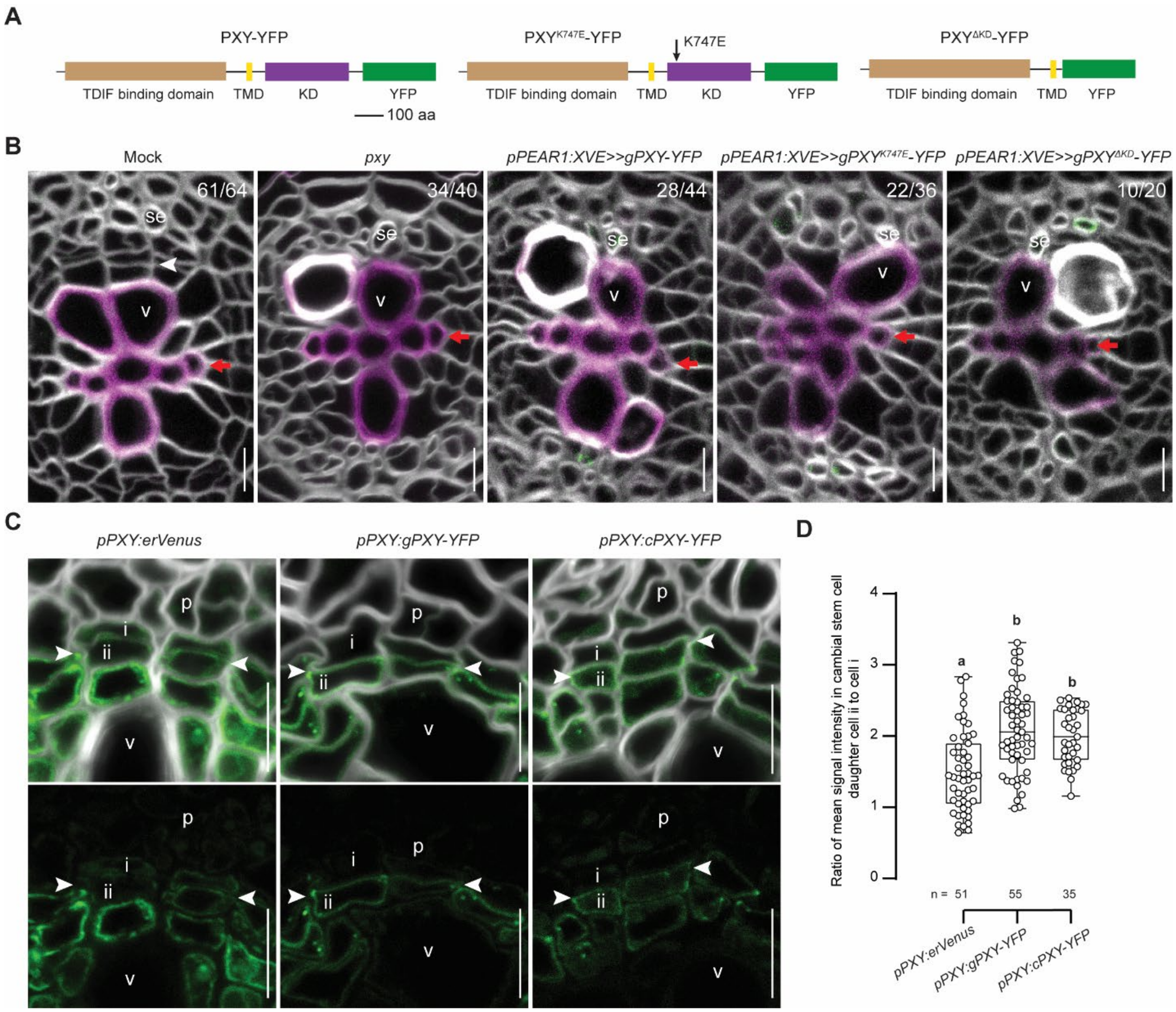

Fig. 5 TDIF peptide is sequestered by PXY protein

(**A**) Schematic representation of PXY translational reporters. PXY protein consists of a Leucine-rich repeat domain containing the TDIF binding motif, a transmembrane domain (TMD) and kinase domain (KD). (**B**) Confocal root cross sections of *pxy* and 5-day-old *pPEAR1:XVE>>gPXY-YFP*, *pPEAR1:XVE>>gPXY^{K747E}-YFP* and *pPEAR1:XVE>>gPXY$^{\Delta KD}$-YFP* lines induced for 5 days each of which showed a *pxy*-like stem cell differentiation phenotype with vessels (v) adjacent to a sieve elements (se), by contrast to the mock. (**C**) Confocal root cross-sections of 14-day-old *pPXY:erVENUS*, *pPXY:gPXY-YFP* and *pPXY:cPXY-YFP*. Phloem (p), xylem vessels (v). (**D**) Boxplot showing the ratio of mean signal intensities between xylem side (ii) and phloem side (i) daughter cells of the cambial stem cell within radial cell files. Letters in (D) indicate significance using one-way ANOVA with a Tukey post hoc test. Red arrows mark the primary xylem axis. White arrowheads mark recent cell divisions. Scale bars 10 µm (B and C).

Science
AAAS

Supplementary Materials for

Identification of cambium stem cell factors and their positioning mechanism

Gugan Eswaran *et al*.

Corresponding authors:
Kirsten ten Tusscher, K.H.W.J.tenTusscher@uu.nl
J. Peter Etchells, peter.etchells@durham.ac.uk
Ari Pekka Mähönen, aripekka.mahonen@helsinki.fi

The PDF file includes:

Materials and Methods
Modelling Methods
Figs. S1 to S12
tables S1 to S6
References

Other Supplementary Materials for this manuscript include the following:

Data S1 and S2

Materials and Methods

Plant material and cloning

The Col-0 background was used throughout. *pxy* (9), *35S:CLE41* (12), *plt3plt5* (*plt3-1, plt5-2*) (48), *ant-GK* (GK-874H08) (20), *plt5* (*cho1*) (49), *plt3plt5plt7-cr* (23), *plt3plt5plt7-tdna* (*plt3-1*, SALK_127417, *plt5-2*, SALK_059254; *plt7-1*, SAIL_1167_C10) (22), *gPLT1-YFP* (18), *gPLT2-YFP* (18), *gPLT4-YFP* (18), *gPLT7-YFP* (22), *gVND6-GUS* (50), *pAPL:3xYFP* (51) have been described previously. These lines together with the new lines generated in this study are listed in **Data S2**.

All entry clones were generated by PCR amplification of the target sequence. PCR products were then recombined into MultiSite Gateway compatible pDONR entry vectors using a BP clonase reaction or using Golden Gate assembly cloning methods. Multisite Gateway technology was used to assemble the entry clones into Gateway compatible binary vectors using multisite gateway LR reactions. Primers for PCR amplification, pDONR entry vectors, and expression vectors are listed in the **Data S2**.

Upon plant transformation of expression vectors, putative single insertion lines were identified based on Mendelian segregation of the selectable marker. Multiple single insertion lines were screened for each construct to observe the most consistent expression patterns or phenotypes.

To obtain *plt3plt5plt7ant* quadruple mutants, *plt3plt5plt7-cr* (♀) was crossed with *ant-GK* (♂). *PLT5* and *PLT7* are located in the long arm of chromosome 5. Thus, we expected linkage between *PLT5* and *PLT7*. 140 F2 seedlings were germinated for genetic analysis. Since *plt3plt7* double mutants are unable to form lateral roots (48), and *antplt3plt7* has defects in SAM maintenance (24), we genotyped only those F2 seedlings lacking lateral root formation and showing defects in SAM (altogether 3 individuals). These 3 seedlings were genotyped as *plt3plt5plt7-cr;ant-GK*. To analyze the root cambium phenotype of *plt3plt5plt7-cr;ant-GK* quadruple mutant, we germinated 618 F2 seedlings and identified additional 7 seedlings with defects in lateral root formation and SAM maintenance. These 7 seedlings underwent anatomical analysis.

To generate multiple independent quadruple mutants, we transferred a CRISPR construct targeting *ANT* (*ant-cr*) into *plt3plt5plt7-cr* and analyzed T1 seedlings. This CRISPR construct contained two sgRNAs designed to create a large deletion in *ANT*. The primers used to generate two fusions of a small nuclear RNA promoter and sgRNA (*pAtU3-sgRNA*) are listed in the Data S2. The resulting PCR products were cloned into a *p2PR3-Bsa I-ccdB-Bsa I* entry vector using Golden Gate and Gibson assembly cloning methods thus concatenating the two *pAtU3b-sgRNA1-ANT and pAtU3b-sgRNA2-ANT* fragments. The *zCas9i* (52) was cloned into *p221z-Bsa I-ccdB-Bsa I* using Golden Gate and the primers used to generate *zCas9i* PCR product are listed in the **Data S2**. The final binary vector was generated in a single MultiSite Gateway LR reaction by combining a RPS5A promoter, *221z-zCas9i*, *2R3z-2x-pAtU3b-sgRNA-ANT* and destination vector pFRm43GW (25).

To generate conditional *plt*/*ail* quadruple mutants, we took an advantage of an inducible genome editing system (IGE) (25). An inducible CRISPR construct targeting *ANT* was transformed into two different *plt3plt5plt7* mutant backgrounds, a null combination *plt3plt5plt7-cr* (23) and a weaker allele combination *plt3plt5plt7-tdna* (22). This IGE vector contained the same two sgRNAs as described above to create a large deletion in *ANT* upon treatment with 17-β-estradiol. The IGE binary vector was generated in a single MultiSite Gateway LR reaction by combining a 17-β-estradiol-inducible *WOODEN LEG* (*WOL*) promoter (26), which drives expression in the primary vascular cylinder (53), giving rise to all the secondary tissue in the root (3), *Cas9p*, *2R3z-2x-pAtU3b-sgRNA-ANT* and destination vector pFRm43GW (25).

To facilitate screening of transformed seeds, we used seed-specific RFP fluorescence provided by *pFRm43GW*. The *plt3plt5plt7-cr;IGE-ant* and *plt3plt5plt7-tdna;IGE-ant* lines were germinated directly in 1/2 GM plates supplemented with 5 μM 17-β-estradiol and grown for 15 days and 13 days respectively alongside Col-0 and their respective *plt3plt5plt7-cr, plt3plt5plt7-tdna* controls.

To generate the translational reporter of PXY, full-length genomic DNA and cDNA of *PXY* without stop codons were amplified with primers BsaI-PXY-F and BsaI-PXY-R. YFP with a stop codon was amplified with primers BsaI-VenYFP-F and BsaI-VenYFP-R. The resulting genomic PXY (gPXY) or cDNA PXY (cPXY) PCR products together with the YFP PCR product were cloned into the *221z-Bsa I-ccdB-Bsa I* by Golden Gate cloning. The *pPXY:gPXY-YFP* and *pPXY:cPXY-YFP* binary vectors were generated by combining 1R4z-pPXY, 221z-gPXY-YFP or 221z-cPXY-YFP, 2R3a-3AT and destination vector pFRm43GW in a single MultiSite Gateway LR reaction.

To generate the translational reporter of PXY with a K747E mutation, a PXY^{K747E} mutation was introduced by primers. 221z-gPXY-YFP was used as template and amplified with two pairs of primers BsaI-PXY-F + BsaI-PXY^{K747E}-R and BsaI-PXY^{K747E}-F + BsaI-VenYFP-R. These two PCR products were cloned into *221z-Bsa I-ccdB-Bsa I* by Golden Gate cloning, resulting 221z-gPXY^{K747E}-YFP. *pPXY:gPXY*^{K747E}*-YFP* binary vectors were generated by combining 1R4z-pPXY, 221z-gPXY^{K747E}-YFP, 2R3a-3AT and destination vector pFRm43GW in a single MultiSite Gateway LR reaction.

To generate the reporter for truncated PXY without kinase domain PXY$^{\Delta KD}$, a 2076 bp PXY fragment downstream of the PXY start codon was amplified with primers BsaI-PXY-F and BsaI- PXY$^{\Delta KD}$-R. The PCR product was inserted into *221z-Bsa I-ccdB-Bsa I* by Golden Gate cloning, resulting 221z-PXY$^{\Delta KD}$. *pPXY: gPXY*$^{\Delta KD}$*-YFP* binary vector was generated in a single MultiSite Gateway LR reaction by combining 1R4z-pPXY, 221z-gPXY$^{\Delta KD}$, 2R3a-VenYFP-3AT and destination vector pFRm43GW.

For *pPEAR1:XVE>>gPXY-YFP* and *pPEAR1:XVE>>gPXY*^{K747E}*-YFP*, entry clones 1R4a-pPEAR1:XVE, 221z-gPXY-YFP or 221z-gPXY^{K747E}-YFP and 2R3a-3AT were incorporated into pCAM-kan-R4R3 by LR reaction, respectively.

For *pPEAR1:XVE>>gPXY*$^{\Delta KD}$*-YFP*, entry clones 1R4a-pPEAR1:XVE, 221z-gPXY$^{\Delta KD}$, 2R3a-VenYFP-3AT were incorporated into pCAM-kan-R4R3 by LR reaction.

Plant growth and chemical treatments

All the plants were grown vertically in a plate in a 23°C growth chamber with 8 hours dark & 16 hours light cycle. Seeds were surface sterilized using 70% ethanol with Tween-20 (µl/ml) solution for 5 min with vortexing, followed by five washes in sterile Milli-Q (MQ) water. The sterilized seeds were stratified for 2 days at 4°C in darkness before plating them on 1/2 germination medium (GM) containing 0.5x Murashige and Skoog (MS) media with vitamins (Duchefa), 0.8% plant agar, 1% sucrose and 0.5 g/l MES pH 5.8. Alternatively, 0.5x MS (pH 5.8), 1% sucrose and 1% agar was used. The age of the plants was measured from when the plates were vertically positioned in the growth cabinet.

Aqueous 10 mM stocks of P9A and TDIF peptides (GeneCust) were prepared and stored at the -80°C. 10 mM stocks of EdU (Thermo Fisher), dissolved in dimethyl sulfoxide (DMSO) was prepared and stored at -20°C. 17-β-estradiol (EST) (Sigma), was prepared as a 20 mM stock solution in DMSO and stored at -20°C.

Short term (24 hours or less) TDIF and P9A treatments were performed in liquid 1/2GM containing the respective peptide with the working concentration of 10 µM. Longer treatments were performed on 1/2GM plates. 17-β-estradiol induced gene expression was achieved by transferring plants onto plates containing 5 µM 17-β-estradiol or an equal volume of DMSO as a mock treatment, except in **Fig. 2F and fig. S6E** and *35S:XVE>>PLT5-TagRFP* RNA-Seq where 1 µM 17-β-estradiol was used. For EdU incorporation, plants were placed in liquid 1/2GM containing 10 µM EdU for 16 hours prior to fixation.

RNA-Seq profiling and data analysis

Transcriptomes of *pxy* and *35S:CLE41* in comparison to wild type were determined from seedlings grown on vertical plates for 7 days. Upon harvesting, seedlings were separated into root and shoot samples by separating plants at the root-hypocotyl junction. RNA and library preparation in biological quadruplicate was performed as described (*54*). 50 bp single end reads were obtained on the Illumina HiSeq 4000 platform. Sequencing was performed by the QB3 Genomics Facility, University of California, Berkeley. Quality checking and trimming of the raw FASTQs was performed with Kraken (*55*) followed by alignment to TAIR10 with Tophat2 (*56*). An average of 3.4M reads were obtained per treatment. Gene counting was performed with HTSeq (*57*), and differential gene expression was determined with DESeq2 (*58*). Cut-offs for differential expression was an adjusted p value < 0.05. The data is available on GEO (accession number GSE119872). DEGs are listed in **Data S1**. GO analysis was performed on genes differentially expressed in either *35S:CLE41* or *pxy* relative to wild type (Col-0).

For PLT5 transcriptome analysis, *35S:XVE>>PLT5-TagRFP* seeds were germinated on 1/2 GM plates for 9 days or 9 days 16 hours, and then transferred to 1 μM 17-β-estradiol or DMSO plates for 24 hours or 8 hours, respectively. For each sample, 1.5 cm of root segments below the root-hypocotyl junction were collected from 15 individuals. Visible lateral roots were removed. RNA isolation, library preparation and data analysis were done as previously described (*59*) except single-end reads (86bp) and were mapped to *Arabidopsis* reference genome (TAIR 10.39). Differential expression between the mock and inductions was analyzed using the edgeR package (*60*). Subsequently, Pvalue < 0.05 was applied to identify differentially expressed genes (DEGs). The data is available on GEO (accession number GSE264403). DEGs are listed in **Data S1**.

Thin sections, GUS staining, and light microscopy

All the root samples were sectioned 5mm below the hypocotyl junction unless mentioned otherwise. Samples were fixed overnight in 1% glutaraldehyde, 4% formaldehyde in 0.05 M sodium phosphate buffer pH 7.2, followed by dehydration through an ethanol series, and embedding in plastic resin using either Historesin (Leica) or JB4 (Polysciences). 3, 5 or 10 μm sections were cut with either an RM2055 microtome (Leica) using a microtome knife, or a Shandon Finesse E+ microtome (Thermo) using a glass blade. Sections were stained with either double staining of 0.05% ruthenium red (Sigma-Aldrich) and toluidine blue (Sigma-Aldrich; 5s in each respectively, rinsed between staining's and afterwards with water), or 0.025% aqueus toluidine blue for 30s. Sections were mounted in either water or Histomount (National Diagnostics) and visualized either with a Leica 2500 Microscope or Zeiss Axioskop using 20x or 40x objectives.

For GUS-stained samples, Historesin was used. The GUS-staining protocol was adapted from (*61*). Samples were held in GUS-staining solution at 37°C until the appropriate staining level was reached prior to fixation.

Fluorescent marker analysis, vibratome sections and EdU detection

Lateral view of the fluorescent samples were analyzed in plates using Leica MZ165FC microscope, Hamamatsu C11440 digital camera, and Leica LAS X program.

For cross sections fluorescent samples were fixed as previously described (*3*), prior to embedding in 4% agarose. Agarose blocks were cut with the vibratome into 200 μm sections for confocal analysis. Sections were placed in PBS and stained with SR2200 (1:1000, Renaissance Chemicals) for cell wall staining. Lignified cell walls were stained with Basic Fuchsin, as previously described (*62*).

To visualize the EdU positive nuclei after EdU incubation, The Click-iT EdU Alexa Fluor 488 Imaging Kit (Thermo Fisher) was used for detection with a modified EdU detection mix (*63*). Samples were incubated in the detection mix for 1h and then transferred into PBS with SR2200 (1:1000).

Confocal microscopy and image processing

Confocal imaging was performed on PBS-mounted samples with a Stellaris 8 confocal microscope, except *35S:XVE>>gPLT5-TagRFP* analysis was carried out with Leica SP5 (20x and 63x objectives; Leica). Images were obtained using Las AF software (Leica). Samples visualized with multiple channels were imaged in the sequential scan mode. Confocal settings vary between experiments but were constant within experiments. The exception to this was cell wall staining to aid visualization. Here, SR2200 (cell wall) signal was adjusted during imaging (but not the fluorophore of interest) and therefore SR2200 settings varies between the sample and respective control.

Image projections

Circle unwrapping projections (**Fig. 3A**) were performed as previously described (*6*).

Image analysis

Image analysis and quantification were performed using Leica AF Lite 2.6.x, LithoGraphX 1.2.2 with Builder 1.2.2.7, and FIJI ImageJ v1.52 (*64*). For **Fig. 1C**, Cell numbers were calculated within 35 µm diameter area (primary xylem was in the center of this area). For image quantification in **Fig. 2E**, the distances of EdU-labelled nuclei were measured from the central point of each cross-section, as previously described (*3*). Locations of EdU-positive nuclei were expressed as a relative position along the radii of cross-sections. For each sample, the frequency distribution of EdU-labelled nuclei was then calculated and assigned into one of ten classes based on their relative positions in the cross-section. For each independent repeat, the mean and standard error of the frequency distributions of different cross-sections were calculated and plotted according to the treatments applied. To identify significant differences in the frequencies per distance class between the mock and induced conditions, Student's t-tests were applied.

Operational definition of cambial stem cells relied on morphological features of the tissue, supported by previous lineage tracing analysis which demonstrated that transit amplifying divisions occurred rarely in this tissue (*3*). Therefore, the vast majority of divisions were derived from the cambium stem cell. Cambium stem cells were thus considered to be those with thin cell walls suggesting a very recent deposition of phragmoplast. Subsequent experiments demonstrated that this feature co-occurred with CAIL expression (Fig. 1D for *PLT5*; fig. S2 for *ANT*, *PLT3* and *PLT7*). However, where *PLT5* was over-expressed or induced by TDIF (and in any other CAIL manipulation data e.g. **fig. 2F, fig. 3B, fig. 4G**), recent cell divisions, as judged by the presence of thin cell walls, was considered to be cambial cells, not stem cells. This is due to inability to define stem cells in cases when stem cell regulators, CAILs, are manipulated. In future studies, characterization of CAIL-independent stem cell markers will enable the precise identification of the cell identities in the CAIL manipulation lines.

Number of cambium cell layers in **Fig. 1F, 1G** refers to number of cells in a given radial cell files between recently differentiated sieve elements and vessels. We omit quantifying radial cell files which did not contain recently differentiated sieve elements or vessels, or poor image quality prevented us to make quantification. For quantification of **fig. S3A**, **fig. S3C**, **fig. S4B** and **fig. S4C**, the diameter indicates the distance between two phloem poles.

For quantification of *plt3plt5plt7-tdna;IGE-ant* root cross-sections in comparison to wild type and *plt3plt5plt7-tdna* controls **(fig. S4C)**, sectors in the upper panel lacking secondary xylem vessel differentiation were considered as mutant sectors as such sectors were absent in controls. The lower panel considers secondary phloem differentiation around primary phloem pole. Controls developed secondary phloem around primary phloem pole, but sectors in *plt3plt5plt7-tdna;IGE-ant* plants with reduced secondary xylem formation produced also less secondary phloem (quantified as number of sieve elements) were considered to be mutant sectors.

For quantification of *gANT-3xYFP* fluorescence in **Fig. 3E**, only non-xylem-pole pericycle cell lineages were considered. The first, second and third nearest-neighboring cambial cell to vessels were defined as position 1, 2 or 3, respectively and assigned as *gANT-3xYFP*-positive or negative depending on the presence or absence of signal. To determine the presence or absence of signal, nuclei with YFP signals were extracted using watershed segmentation and thresholds for lower signal intensity, nuclear size (more than 2 μm^2), and circularity (0.5-1). Extracted nuclear images were compared with the original images to assess the correctness of the chosen parameters. Occasionally, watershed failed to separate neighboring nuclei or over-segmented a single nucleus. In those cases, the extracted nuclei images were manually corrected.

For quantification of *pANT:erRFP* fluorescence in **Fig. 4D**, the signal intensity in one cell file was measured from the outermost xylem vessel phloemward. For **Fig. 4H**, a line was drawn along the tangential axis of the root cross section between the outer edges of vessels. Cells between these two vessels on this line were considered to be at position zero. The radial cell file phloemward from this cell zero were marked as +1,+2,+3...+8; and towards xylem as -1,-2,-3.

For quantification of *pPXY:erVENUS*, *pPXY:gPXY-YFP* and *pPXY:cPXY-YFP* in **Fig. 5D**, the mean signal intensity of each cambium stem cell daughter cells in one radial cell file was measured with Fiji. In one radial cell file, the ratio is calculated with the mean signal intensity of xylem-side daughter cell (ii) divided with the mean signal intensity of phloem-side daughter cell of stem cell (i).

RT-qPCR

11-day old plants with inducible *PXY* RNAi expression in *ANT* fluorescent reporter backgrounds (*35S:XVE>>PXY-RNAi; pANT:erRFP*) were transferred to 1/2GM plates containing either 5 µM of 17-β-estradiol (induced) or DMSO (mock) for three days. For RNA purification, 2 cm of primary roots 0.5 cm below the root-hypocotyl junction were harvested from ≥10 individuals for induced- or mock-treated plants. Total RNA from root samples was purified with RNeasy Plant Mini Kit (QIAGEN) with an on-column DNase I treatment (QIAGEN). cDNA was synthesized using the iScript™ cDNA Synthesis Kit (Bio-Rad) following the manufacturer's instructions. qRT-PCR experiments were carried out in 10 µl reaction volume using the LightCycler 480 SYBR Green I Master Mix (Roche Life Science) in a CFX384 Touch Real-Time PCR instrument (Bio-Rad). The PCR programme included an initial denaturation step at 95°C for 5 min, then 45 cycles of (95°C for 10s, 59°C for 10s, 72°C for 15s), followed by a melting curve analysis. Each sample was run three times. Expression levels were normalized using the comparative CT Method (ΔΔCT method) against the UBC21 reference gene expression (*65*). All primers used in qRT–PCR are listed in **Data S2**.

General methodology and statistical analysis

All experiments were repeated at least two times. We excluded samples that germinated poorly, or showed overall growth defects that were confirmed genetically not to be related to the genotype. The number of individual roots analyzed is shown as *n* in the figures or figure legends, except for **Fig. 1G, Fig. 4, D, H, Fig. 5D**, *n* represents radial cell file. The fraction in the corners of some figures indicates the frequency of the observed phenotype. Before assessing statistical analyses, normality of residues distribution and variances homoscedasticity were checked using Shapiro's and Levene's tests, respectively, to determine the type of statistical analyses that can be used for each quantitative dataset. Accordingly, Wilcoxon-Mann-Whitney test was used to assess mean comparison for the **Fig. 2, C and G; Fig. 3, A and D; and Fig. 4, D and H** while student t-tests were used for the **Fig. 2E and fig. S3A**. For multiple comparisons, Kruskal-Wallis and Dunn's post-hoc tests were used for the **Fig. 1, C and G**. For the **Fig. 3E**, categorical distribution was tested using Chi-square test. One-way ANOVA with a Tukey multiple comparisons test was used for **Fig. 5D, fig. S3C and fig. S4B**. All the p-values for the different statistical comparison are available in the data supplemental information. Specific tests are detailed in the figure legends. All statistical analysis were performed in the R studio version 2023.06.0-421 and GraphPad. For boxplots, the central line indicates the median; the bounds of the box show the 25th and 75th percentiles; and the whiskers indicate maximum and minimum values (the values out of the whiskers are outliers). For bar plots, the bar height and the error bar represent the mean and the standard error of the mean, respectively, except **fig. S6F**, the error bar indicates standard deviation. For plots showing quantitative data, every individual data point is shown on top of the plots. For the **Fig. 3A** comparisons of the distance between P9A and TDIF conditions in both *pPLT5:erRFP* and *pPXY:erVenus* were obtained by sub-setting all the negative distances values (xylem region) present around the mean ± se of the fluorescence peak in P9A samples (data available in the data S1). *p-values* shown in the figure represent comparison of the mean distances between P9A and TDIF conditions using two tailed Wilcoxon-Mann-Whitney test.

Modelling Methods

Model network architecture and dynamics

In this paper we employ models of the radial patterning of the secondary tissue, using both a single cell and multicellular model setup. In the latter case, because of the rotational symmetry, we restrict ourselves to modeling vascular patterning in a single 1D cell file of the differentiating root vasculature. In our model all cells contain the same gene regulatory network describing the dynamics of auxin, TDIF, PXY, ANT, PLT5, and HD-ZIP III concentrations. We took PLT5 as a representative of PLT3, PLT5 and PLT7, based on their presence in the same PLT subclade and their highly redundant functionality. In contrast, since our data indicated a differential regulation of ANT as well as differential downstream effects of ANT, ANT was modeled separately. Note that we use [] to signify concentrations, and that concentrations in our model are in dimensionless units.

Dynamics of the individual players making up this network are modeled using differential equations, for this we introduce variables T (TDIF), X (PXY), C (TDIF bound by PXY), A (ANT), P (PLT5), H (HD-ZIP III) and finally, a (auxin). Model cells can attain different vascular fates through experiencing different combinations of auxin and TDIF levels and through the regulatory network translating this into different gene expression patterns for PXY, ANT, PLT5 and HD-ZIP III. Cells with sufficient PLT5 and ANT expression adopt cambial identity. Cells lacking these factors differentiate into xylem if they have sufficient HD-ZIP III, or phloem if they lack HD-ZIP III (for more details on the applied threshold levels to determine cell fate see later sections). In addition to intracellular expression dynamics, the TDIF signaling peptide is excreted and diffuses in the apoplast, while the ANT and PLT5 proteins diffuse between cells via plasmodesmata.

Gene regulatory and signaling network architecture

The architecture of the model gene regulatory and signaling network is shown in **(fig. S7)**. Yellow PE (published elsewhere) and orange TS (this study) symbols refer to supporting data the interaction was based on and are summarized in the accompanying tables. In the below sections we describe the system of differential equations used to model the dynamics of the various network components.

Gene expression and signaling dynamics

PXY-TDIF expression and binding

At the heart of the model is the interaction between the auxin induced receptor protein PXY (X) and the phloem produced mobile peptide ligand TDIF (T), that binds to it forming a PXY-TDIF complex (C). We capture the production, movement, association, disassociation, and degradation of PXY and TDIF with the following set of equations.

$$\frac{dX}{dt} = p_X \frac{a^2}{a^2 + K_{a,X}^2}\left((1 - f_{P,X}) + f_{P,X} \frac{K_{P,X}^2}{P^2 + K_{P,X}^2} \right) - d_X X - K_{on} X T + K_{off} C \qquad (1)$$

$$\frac{dT}{dt} = p_T - K_{on}XT + K_{off}C - d_T T \qquad (2)$$

$$\frac{dC}{dt} = K_{on}XT - K_{off}C - d_C C \qquad (3),$$

where p_X is the maximum PXY production rate, $K_{a,X}$ is the value for which the auxin-mediated induction of PXY is at half maximum, $f_{P,X}$ is the maximum fraction of PXY expression that can be repressed by PLT5 and $K_{P,X}$ is PLT5 level at which this repression is at half maximum, d_X is the PXY degradation rate, K_{on} and K_{off} are the rates of PXY-TDIF association and disassociation, p_T and d_T are maximum production and degradation rates for TDIF and d_C is the degradation rate of PXY-TDIF complex. In the single cell layout, through varying the level of p_T we investigate the impact of TDIF level on cell fate.

The dissociation constant $K_d = K_{off}/K_{on}$ determines the ***binding strength*** of TDIF (*T*) to PXY (*X*), and hence influences the amount of complex (*C*) formed that may induce ANT (*A*) and PLT (*P*) expression (see equations below) and by necessity at the same time affects the amount of TDIF that is sequestered by PXY into complex and hence no longer available to freely diffuse, i.e. the ***sequestration strength***. Since we hypothesize that sequestration plays an important role in cambium patterning, we need to compare model simulations with and without strong sequestration. If we were to do this using Eq. 1-3, to obtain weak sequestration would imply using a very high K_d. However, in addition to resulting in weak TDIF sequestration this would also result in low complex levels and hence absence of ANT/PLT induction. To artificially decouple these two effects that both influence cambium patterning, and investigate the importance of sequestration without affecting complex levels and ANT/PLT induction, we make use of an alternative set of equations:

$$\frac{dX}{dt} = p_X \frac{a^2}{a^2 + K_{a,X}^2}\left(\left(1 - f_{P,X}\right) + f_{P,X}\frac{K_{P,X}^2}{P^2 + K_{P,X}^2}\right) - d_X X \qquad (1*)$$

$$\frac{dT}{dt} = p_T - d_T T \qquad (2*)$$

$$C = \frac{\left(X + T + \frac{Koff}{Kon}\right) - \sqrt{\left(X + T + \frac{Koff}{Kon}\right)^2 - 4*(XT)}}{2} \qquad (3*)$$

where X and T now stand for total instead of unbound PXY and TDIF levels, and steady state complex levels are computed from total PXY and TDIF levels following the earlier defined binding and unbinding rates yet ignoring complex degradation and without taking into account that complex formation results in sequestration, i.e we assume all T can diffuse freely.

HD-ZIP III expression

Aside from inducing PXY, auxin also induces the expression of the xylem identity transcription factor HD-ZIP III (*H*). We use the following equation to describe HD-ZIP III expression dynamics:

$$\frac{dH}{dt} = p_H \frac{a^4}{a^4 + K_{a,H}^4} - d_H H \qquad (4),$$

where p_H is the maximum HD-ZIP III production rate, $K_{a,H}$ is the auxin level at which HD-ZIP III production is half maximum and d_H is the degradation rate of HD-ZIP III. Note the use of a Hill-coefficient of 4 as compared to the Hill-coefficient of 2 in our other equations. Importantly, here as in many other cases we have no detailed experimental data on the number of auxin response elements (AREs) in promotor or enhancer and whether or not auxin response factor (ARF) binding to these elements is cooperative, nor on other potential sources for non-linearity to support specific Hill coefficients. Still, non-linear dynamics are reasonable to assume from the rationale that gene expression has a certain maximum (saturation) and that particularly in development non-linear interactions are the rule rather than the exception and are essential for spatial patterning. Furthermore, the Hill-coefficients applied here are on the low side, and far from inducing steep on-off switch like behavior. The somewhat higher Hill-coefficient for auxin-driving HD-ZIP III activation was reverse engineered from the requirement that HD-ZIP III needs to become more highly expressed and hence dominant over PXY at higher auxin levels, while having a more spatially constrained domain and thus a higher auxin K_m, thereby ensuring a stable xylem domain.

ANT and PLT5 expression

ANT expression is induced by both auxin and PXY-TDIF, while being repressed by HD-ZIP III. We assume that auxin and PXY-TDIF induction of ANT function additively and are independently antagonized by HD-ZIP III. Combined this results in the following equations:

$$\frac{dA}{dt} = p_A\left(\frac{a_{a,A}(H)a^2}{a^2 + K_{a,A}^2} + \frac{a_{C,A}(H)C^2}{C^2 + K_{C,A}^2}\right) - d_A A$$

$$a_{a,A}(H) = m_{a,A}\left(\left(1 - r_{H,a}\right) + \frac{r_{H,a}K_{H,A}^2}{H^2 + K_{H,A}^2}\right) \qquad (5),$$

$$a_{C,A}(H) = m_{C,A}\left(\left(1 - r_{H,C}\right) + \frac{r_{H,C}K_{H,A}^2}{H^2 + K_{H,A}^2}\right)$$

where p_A is the maximum ANT production rate, $a_{a,A}$ and $a_{C,A}$ are the auxin and PXY-TDIF dependent ANT induction functions that depend on HDZIP-III repression, $K_{a,A}$ and $K_{C,A}$ are the values of auxin and PXY-TDIF for which their activation of ANT expression are at half maximum, d_A is the degradation rate of ANT, $m_{a,A.}$ and $m_{C,,A}$ are the maximum fractions of auxin and TDIF signaling mediated ANT induction, $r_{H,a}$ and $r_{H,C}$ are the maximum fractions of these that can be repressed by HDZIP-III, and $K_{H,A}$ is the HDZIP-III level at which this repression is half maximal.

Note that while auxin and TDIF-PXY complex are assumed to regulate ANT expression additively, auxin and TDIF-PXY also regulate ANT expression in a multiplicative manner due to the auxin dependent expression of PXY. Finally, HDZIPIII, which antagonizes ANT expression is also auxin-dependent. Since there is no experimental evidence to support either additive or multiplicative regulation of ANT repression by auxin and TDIF-PXY, the additive scenario was chosen as it represents a worst-case scenario as it enables ANT activation outside of the domain of high TDIF-PXY expression, making constrained ANT/PLT expression more challenging and rendering HDIZIPIII repression more important.

In contrast to ANT, PLT5 expression is only induced by TDIF peptide signaling and is not repressed by HD-ZIP III, resulting in the following simpler equation:

$$\frac{dP}{dt} = p_P \frac{C^2}{C^2 + K_{C,P}^2} - d_P P \qquad (6),$$

where p_P is the maximum PLT5 expression rate, $K_{C,P}$ is the PXY-TDIF level for which the expression of PLT5 is half maximum, and d_P is the degradation rate of PLT5.

Model parametrization

After defining network architecture based on experimental data and establishing the basic differential equations-based model describing the dynamical interactions resulting from this network architecture, we next determined the (range of) parameter values to be used for the model.

Defining a parameter range

Production and degradation rates

As a first step, in absence of absolute quantitative data, we scaled the maximum level for the signaling molecules auxin and TDIF, as well as for the transcription factors HD-ZIP III, ANT, and PLT5 and the receptor protein PXY to a value of 100, which can be interpreted as meaning 100%. Note that such a "relativistic" approach is frequently applied in computational developmental modeling studies, both inside and outside of plant biology (examples are (*66*, *67*)) The maximum level of 100 implies that the ratio of production (p) over degradation (d) rates for each gene is set at 100, while the actual rates can be varied. We typically use a d of 0.0002s^{-1} (half-life of approximately 1 hour) and hence a p of 0.02[]s^{-1} (**see table S1**), which albeit somewhat arbitrary is chosen such that it is significantly faster than the rate of cell division, ensuring that despite growth and division driven dilution of proteins, concentrations are always near steady state. While in the current model there is no growth and division of cells, this allows seamless future incorporation of these processes without requiring reparameterization. For the ANT and PLT5 proteins (p_A , d_A , p_P, d_P) we use 10 times slower dynamics (so half-life of approximately 10 hours). We based this on our previous work that identified a slow turnover of PLT2 proteins, assuming that the closely related PLT3,5, and 7 and ANT modeled here have similar turnover dynamics (*18*).

As an exception to the above, for the receptor protein PXY we applied a higher production and degradation rate (typically p_X=0.12[]s^{-1} and d_X =0.0012s^{-1} is used, see **table S1**). The rationale behind these higher rates is that these dynamics encompass both receptor internalization and turnover. Assuming that upon binding of the TDIF ligand to the PXY receptor, the PXY-TDIF complex turns over at the same rate as isolated PXY (d_C =0.0012s^{-1}), this enabled us to investigate the effect of receptor mediated TDIF sequestration and enhanced degradation on TDIF signaling gradient formation. In the parameter sweep, performed on single cell simulations, so in absence of TDIF diffusing away to other cells, the p_T parameter is varied between 0 and 0.02[]s^{-1} to vary total (free+bound) TDIF levels between 0 and 100. In the multicellular simulations, where TDIF is only produced in the phloem cell and diffuses xylemward we applied a higher production rate of 0.03[]s^{-1} in simulations without actual PXY mediated TDIF sequestration, and an even higher production rate of 0.13[]s^{-1} in simulations with sequestration to compensate for the faster turnover of bound TDIF. For a more detailed explanation of this absence/presence of TDIF sequestration see the parameter sweep section.

K_m values and ANT expression regulation

As a second step, having set the maximum level of 100, we were now able to deduce the relevant range for model K_m values, under the assumption that the incorporated players and regulatory interactions were correct and sufficient to explain cambium patterning. Put simply, K_m values of above 100 would cause downstream activated regulatory factors to never reach their maximum levels or downstream repressed factors to never approach their minimum levels, whereas K_m values of 5 or lower would nearly abolish the dependence on an upstream regulatory factor, setting a first broad range of relevant values. Based on the biological data, and the simulated auxin and TDIF profiles in our model, reasonable K_m values can subsequently be further constrained.

Experimental data show that at the phloem side, HD-ZIP III, ANT, PXY are all not expressed. Given that these 3 factors are induced by auxin, and that at the phloem side the superimposed shape of the auxin gradient results in auxin levels of around 8 for the 3 cell settings. Therefore, the K_m at which auxin results in half maximum activation of HD-ZIP III, ANT and PXY factors should significantly exceed this auxin level in order to avoid activation of these factors at the phloem side and was therefore set to a value of at least 15. Additionally, since these factors are known to be highly expressed at the xylem side of the vasculature where auxin levels are highest (up to 100 in our model), the maximum value for these K_m values should not be higher than 50 (70 for $K_{a,H}$ because of its higher Hill coefficient). Taking into account the observation that HD-ZIP III is expressed exclusively in the xylem, where auxin levels are highest, while PXY is expressed in both xylem and cambium stem cells and ANT is only expressed in the cambium stem cells, where auxin levels are intermediate, we can further constrain and order the K_m values. (Note that ANT expression in the xylem is antagonized by HD-ZIP III, see **Fig. 3E**). Specifically, these data imply that $K_{a,H}$ is larger than $K_{a,X}$ and $K_{a,A}$. Finally we constrain $K_{H,A}$ to only become half activated at an HD-ZIP III level of 30 to restrict HD-ZIP III activity to the high auxin domain. Thus, we have established a biologically plausible range for the 4 K_m values in **table S2**.

The last four parameters in **table S2** relate to the induction of ANT by auxin and PXY and its repression by HD-ZIP III. For these we again used biological data and practical considerations to constrain their values. Since auxin also induces PXY, the additive induction of ANT by auxin and PXY corresponds to a direct activation and indirect activation by auxin. To constrain maximum ANT expression and maintain its maximum level at 100 like for the other genes (discussed earlier), in our parameter sweep the parameters controlling the maximum contribution of these two fractions ($m_{C,A}$ and $m_{a,A}$) were varied such that their sum equals 1 (i.e.$m_{C,A} = 1 - m_{a,A}$) causing their relative contribution to the maximum ANT expression to be anti-correlated. Since the PXY-TDIF interaction is known to be critical for ANT expression, we set the maximum direct auxin fraction for *ANT* induction to 0.4 and hence the minimum for the indirect PXY-TDIF induction of ANT to 0.6. The last two parameters, $r_{H,a}$ and $r_{H,P}$, represent the extent to which HD-ZIP III represses the direct auxin induction of ANT, compared to the indirect PXY-TDIF induction of ANT and are independently varied in our parameter sweep. A minimum of 0.4 was set as HD-ZIP III as the biological data dictates that HD ZIP III at least partially represses ANT induction and we are not interested in the regime where this does not occur for the parameter sweep.

PXY-TDIF signaling related parameters

The parameters in **table S3** refer to the translation of PXY-TDIF signal to PLT5 expression as well as the PLT5 repression of PXY expression. Since PXY-TDIF is formed at the region of overlap between opposing PXY and TDIF gradients, where both PXY and TDIF levels are substantially submaximal we reasoned that as a minimum requirement parameter settings should result in maximum TDIF and PXY levels (100) translating into a high level of PXY-TDIF complex (e.g. 80) and little PXY and TDIF to remain unbound (20). This gives us the following constraint for PXY-TDIF association (K_{on}) and dissociation (K_{off}) rates:

$$\frac{K_{off}}{K_{on}} = \frac{[P] * [T]}{[C]} = \frac{20 * 20}{80} = 5 \quad (7)$$

Additionally, we assumed that association and dissociation rates are faster than the turnover of these proteins themselves. We settled on K_{on} =0.02 and K_{off} =0.1, the latter being approximately 100 times faster than the degradation rate of PXY.

Note that since PXY is expressed as a gradient tapering off from the xylem side and TDIF diffusion results in a gradient tapering off from the phloem side, at the point where PXY and TDIF meet PXY and TDIF levels are considerably lower than the 100 mentioned above. As a consequence, TDIF-PXY complex numbers and receptor occupancy levels will be significantly smaller. Thus, intermediate values of PXY-TDIF complex should be capable of inducing the high levels of ANT and PLT5 expression required for cambial identity, while low PXY-TDIF levels should not lead to their expression. Combined this sets a range of K_m values for PXY-TDIF induced expression for ANT between 15 and 35, and for PLT5 between 20 and 40. We assigned slightly lower values for $K_{C,A}$ than for $K_{C,P}$ for two reasons. First, PLT5 represses PXY, so to somewhat protect PXY from this, PLT5 induction should require significant levels of PXY-TDIF. Secondly, HD-ZIP III represses ANT, so to compensate for this, a slightly lower PXY-TDIF should already sufficiently induce ANT.

The repression of PXY by PLT5 results in a negative feedback loop that puts a cap on the PXY-TDIF induced *PLT5* and *ANT* expression. To still enable the high *PLT5* and *ANT* expression observed experimentally, we assume that PLT5 can maximally reduce PXY levels by 30%, and that for this maximum repressive activity high PLT5 levels (K_m>30) are needed. We speculate that such a parametrization may serve *in planta* as a sort of homeostatic mechanism, enabling cells to generate high expression of *PLT5* and *ANT* with moderate PXY-TDIF levels, while preventing even higher PLT5 and ANT levels when PXY-TDIF levels further increase. Since the maximum and K_m of PLT5 mediated PXY repression have similar effects, we keep this maximum repression constant while varying the K_m to vary overall repression in the performed parameter sweep.

Cell fate threshold values

Finally, we need to set the values for the threshold parameters determining how we translate gene expression patterns into vascular cell fate. Based on our experimental data it is the activity of PLT5 and ANT that induce cambium stem cell identity. Given that PLT5 and ANT individually have a maximum protein level of 100, a threshold level above 100 implies that cambium stem cell identity requires both factors being present in significant amounts. Since knockout studies suggest this not to be the case (*20*), we chose a value of ANT+PLT5>75 for the cambium stem cell identity threshold.

Similarly, experimental data indicates that HD-ZIP III expression induces xylem cell fate. We set the threshold value for HD-ZIP III above which xylem fate is induced to 30. Note that the precise level of this threshold mainly determines the auxin level required to shift from phloem to xylem fate. Phloem fate occurs if neither the demands for xylem nor cambium stem cell fate have been met by the cell's expression state, thus PLT5+ANT <75 and HD-ZIP III<30.

Parameter sweep

To determine the robustness with which the above-described network reproduces the biological observation of high auxin levels resulting in xylem differentiation, high TDIF and low auxin levels resulting in phloem fate, and intermediate values inducing cambial identity, we applied a parameter sweep across the previously identified plausible ranges of parameter values. We varied each of the parameters from **tables S2 and table S3** in set increments between these extreme values. Given that $m_{C,A} = 1 - m_{a,A}$, and $r_{H,a} = r_{H,C}$ this results in a total of 10 free parameters, with for 7 parameters 5 distinct values, and for 3 parameters 7 distinct values. Overall, this results in a 10-dimensional parameter search space subsampled in 5^7 times 7^3=26,796,875 different points. To allow interested readers to perform their own parameter sweep without the use of extensive computational resources, in the provided code we increased the step size with which parameter values are varied 2-fold reducing the number of sampled parameter combinations to 3^7 times 4^3=139,968.

For each selected combination of parameter values the single cell model is subjected to a matrix of auxin and (total, free+bound) TDIF levels. Auxin levels are simply superimposed and varied between 0 and 100 in increments of 10 resulting in a total of 11 different auxin levels. TDIF levels are the result of TDIF production, sequestration by PXY, and degradation of free and bound TDIF. Due to the higher turnover of bound relative to free TDIF, and the fact that bound TFY not only depends on total TDIF but also on PXY and hence auxin levels, total TDIF is hard to precisely control through simply varying its production rate in the full model. Therefore, to obtain the precise control of total TDIF levels independent of auxin level that is needed for our parameter sweep, we used TDIF and PXY levels to compute TDIF-PXY complex levels and the PLT/ANT induction this results in yet ignored PXY mediated TDIF sequestration and the differential degradation this results in (thus applying equations 1*, 2*, 3* instead of 1, 2, 3). Note that - given that this is a single cell model in which TDIF cell-to-cell movement is irrelevant- identical simulation outcomes would occur if instead of ignoring sequestration the bound and unbound TDIF would have identical degradation rates, as well as that highly similar simulation outcomes would occur if the higher degradation rate of TDIF is compensated for by a higher production rate. Through varying p_T between 0 and 0.02 with increments of 0.004, combined with $d_T = 0.0002$ s^{-1}, we vary total TDIF between 0 and 100 in steps of 20, resulting in a total of 6 different TDIF levels. Overall, each sampled parameter combination is thus subjected to a matrix of 66 auxin-TDIF combinations. For each pair of auxin and TDIF levels investigated, we score across the entire range of the parameter sweep the frequency with which the cell converges to the different possible cell types, enabling us to draw 2D auxin-TDIF cell fate maps. As long as the combined threshold for PLT5+ANT for cambium stem cell formation remains below 100, there is only a quantitative shift in model outcome (**fig. S8, B** and **C**), while the general behavior remains robust.

Role of HD-ZIP III in specifying xylem

By taking specific subsets of the parameter sweep, where we keep one parameter constant, we can assess the effect of that parameter. While for most parameters we set relatively narrow ranges, the HD-ZIP III repression of ANT via $r_{H,a}$ and $r_{H,X}$ were left free to vary between barely repressing ANT at 0.4, to completely repressing ANT at 1.0. By comparing the results of the entire parameter sweep with the results of subset of simulations obtained for $r_{H,a}$ =1 and $r_{H,X}$ =1, we show how a maximum repression of ANT by HD-ZIP III is able to shift cells with high auxin and intermediate TDIF from cambial identity to xylem identity (compare **fig. S8, B** and **D**). Thus, this maximum HD-ZIP III activity can safeguard the high auxin xylem from intermediate TDIF mediated conversion to cambium stem cell fate.

Model analysis

After having established (a range of) plausible parameter values for our model, we analyzed whether the defined model architecture results in a single equilibrium the location of which (variable values) depends on auxin and TDIF inputs, or rather that the model structure results in multi-stability with parameters impacting the presence and basin of attraction of the alternative equilibria. For this we analytically derived the steady states of the model (Appendix 1), demonstrating the model allows for only a single positive, real valued equilibrium.

Extension to multicellular model

In the multicellular model we created a 1D tissue strand with a xylem organizer cell on the left, a mature phloem cell on the right, and 1-3 cambial cells in between. On this 1D cell file we superimposed an auxin gradient which has its maximum at the xylem organizer cell and incorporated production of TDIF occurring in the mature phloem cells (see Eq. 2). The model was run till it reached steady state before analyzing outcomes.

The model is grid based, with a space step of 0.5 microm with individual cells having an explicit width and height, and cell walls in between cells having the width of a single space step, i.e. 0.5 microm. To take into account experimentally observed cell size differences, we applied the following cell widths: xylem cell 12 µm, cambium stem cell 8 µm and phloem 16 µm. The height of cells was set at 25 µm independently of cell type.

Superimposed auxin gradient

Auxin is a key player in cambium development, being a major regulator for HD-ZIP III, PXY and ANT expression. In the cambium, experimental data show a characteristic auxin gradient with its maximum at the most cambium-ward adult xylem cell that gradually decreases towards the phloem. In absence of sufficient data on the relative importance of longitudinal and transversal auxin transport and local auxin production in shaping this gradient, instead of explicitly modeling auxin dynamics, we superimposed an auxin gradient according to the following equation:

$$
\begin{aligned}
a_{xylem} &= max_a \\
a_1 &= \left(max_a - drop_{xylem}\right) \\
a_{i>1} &= \frac{\left(max_a - drop_{xylem}\right)}{mod_{cambium} i^2}
\end{aligned}
\qquad (8)
$$

,where i is the cell number starting at 1 in the most xylem-ward cambial cell, max_a is the level of auxin at the auxin maximum in the xylem (default level 100), $drop_{xylem}$ is the initial drop relative to the maximum for the first cambial cell (default level 60), and $mod_{cambium}$ cambial modulates the further reduction of auxin as distance (measured in number of cells) from the xylem increases (default level 1.25). Overall this results in a sharp drop of auxin levels from the xylem to the first neighboring cambium cells, followed with a more gradual decline of auxin levels to subsequent cambium cells.

TDIF and PLT/ANT transport

Gene expression and thus protein level dynamics were modeled on a cellular level, using a single ODE per species and cell (see equations below). In contrast, transport of TDIF, ANT and PLT was modeled on the grid level. For this, first, cell level protein levels were assigned to the individual grid points within a cell. Next, we computed a concentration gradient based flux between the rightmost grid points of the left neighbouring cell and the leftmost grid points of the right cell. This can be taken as a diffusive flux through the plasmodesmata from one cell's cytoplasm to the other in the case of PLT/ANT, or as the diffusive flux across the cell wall separating two cells in the case of TDIF. To enable the use of a single diffusion constant we assumed plasmodesmatal density and aperture to be equal between the different cell types and incorporated the effects of plasmodesmatal mediated diffusional transport into lowered effective diffusion rates. Similarly, we assumed homogeneous cell wall properties and hence a single diffusion constant for TDIF transport. No-flux boundary conditions were applied to the leftmost gridpoints of the leftmost cell and the rightmost gridpoints of the rightmost cell. After computing the transport, grid-based levels within each cell were averaged to obtain cell level values. Note that by computing transport only between boundary grid points, we automatically scaled for cell volume and for length of cell-cell interface (see equations below). Transport computations were performed at each timestep after updating the ordinary differential equations. Model simulations use the rate parameters of **table S1**, and the default auxin and PXY-TDIF parameter values of **table S2 and table S3** unless explicitly stated differently, as described in **table S5 and table S6.**

Apoplastic diffusion of the phloem secreted TDIF peptide into the cambium stem cells and towards the xylem is critical for achieving TDIF signaling. The TDIF peptide consists of 12 amino acids (aac) (*68*). While no experimental data for TDIF diffusion rates could be found in the literature, we found rates of 4.3 * $10^{-10}m^2/s$ for oxytocin (9 aac) and 3.52 * $10^{-10}m^2/s$ for somatostatin (14 aac) (*69*), and 2.54 * $10^{-10}m^2/s$ for aprotinin (58 aac) (*70*) and 1.26 * $10^{-10}m^2/s$ for the approximately 50 amino acid long drkN SH3 domain (*71*). Given the relation between number of aac, molecular weight and protein size TDIF diffusion rates are expected to be closest to the higher values observed for the similar sized oxytocin and somatostatin peptides, i.e. approximately 4 * $10^{-10}m^2/s$. However, we found that in order to prevent TDIF from spreading homogeneously over the small number of cells in and around the cambium, diffusion coefficients that are 5 orders of magnitude smaller were required in our model (D_T=0.00094 um^2/s=0.94 * $10^{-15}m^2/s$). Experimentally measured diffusion constants obtained from the literature are typically obtained in a watery solution. In contrast, in the cell wall viscosity is much higher than that of water and it is well established that viscosity is inversely related to the diffusion coefficient (Stokes-Einstein relation), additionally the cell wall is charged leading to interactions further slowing diffusion (*72*), and finally the cell wall is a porous medium with the cell wall fibrils forming a complex network of obstacles for diffusion (effective diffusion inversely related to tortuosity). Indeed, a classical study by Kramer and co-workers demonstrated that the environment of the cell wall causes a one to two order of magnitude decrease in diffusion rates relative to water, with the two order of magnitude decreases occurring higher up in the root in the area where cambium formation occurs (*73*). Correcting the experimental values for this (i.e. 4 * $10^{-12}m^2/s$), thus reduces the difference between experimental and model diffusion constants to 3 orders of magnitude.

Notably, our specific implementation of transport effectively assumes infinitely fast diffusion of TDIF across the cell wall overlaying the cells and limited TDIF diffusion across the cell walls in between cells in 2D (or for PLT/ANT infinitely fast diffusion inside cells and limited diffusion through plasmodesmata), while in reality, identical diffusion can be expected for the cell walls overlaying the cells as for the cell walls separating the cells in our 2D model. Consequently, in addition to diffusion being inhomogeneous, *effective* diffusion across the entire 1D tissue is larger than suggested by the value of the diffusion coefficients used to implement the in between cell transport. If we assume a periodic tissue, with an average cell width of 11 microm and a cell wall width of 0.5 microm, one can approximate this effective diffusion coefficient as the harmonic mean of the intracellular and intercellular diffusion coefficients:

$$D_{eff} = \frac{11.5}{\frac{11}{D_{intra}} + \frac{0.5}{D_{inter}}}$$

which for an infinite intracellular diffusion coefficient translates to $D_{eff} = 23\, D_{inter} = 2.2\ 10^{-14}$, that would further reduce the difference between (adjusted) experimental and (effective) model diffusion constants to 2 orders of magnitude. To validate this inference, we created an alternative model in which full, homogeneous 2D diffusion of TDIF across the tissue strand was simulated. In addition to generating intracellular gradients of TDIF and TDIF-PXY complex we found that while for the normal diffusion coefficient value a very limited TDIF diffusion leads to failure of PLT and ANT activation indeed a 23-fold increased diffusion coefficient compared to the default model generates a similar TDIF gradient, PXY binding and PLT and ANT activation (Fig S10A).

Finally, as explained earlier we take a relativistic modeling approach and set maximum levels of all players to 100 arbitrary units by fixing the ratio of production over degradation rates to 100. While we applied some reasoning for the timescales of production and degradation rates, with e.g. ANT and PLT having slower turnover based on experimental data than other proteins, applied timescales are still relatively arbitrary. With regards to TDIF these timescales are relevant for the diffusion coefficients needed to achieve a particular gradient length. Assuming homogeneous TDIF diffusion and ignoring PXY mediated TDIF sequestration, the analytical solution for a production-degradation-diffusion system is given by:

$$T(x) = \frac{p_T}{d_T} \frac{\cosh(\lambda x)}{\cosh(\lambda L)}$$

with $\lambda = \sqrt{d_T/D}$ and L the length of the tissue. From this it follows that identical steady state gradients can be generated if the TDIF diffusion coefficient and degradation constant are both increased or decreased by the same factor. This analysis thus suggests that unless mechanisms are in place that cause TDIF to diffuse substantially slower than can be expected for a peptide of that size in planta TDIF turnover is approximately 100-fold higher than assumed in our default model parametrization.

We added a scale factor in our model code, allowing interested users to test that simultaneously increasing TDIF diffusion, TDIF and PXY production and degradation dynamics with the same factor although generating somewhat different temporal dynamics results in identical steady state model behavior.

The transcription factors ANT and PLT5 are capable of moving between cells through plasmodesmata (*18*). For their transport, our model uses as a default a diffusion coefficient that is 3 orders of magnitude smaller than that used for TDIF. As for TDIF, our specific implementation of ANT and PLT5 transport effectively assumes infinite fast diffusion inside cells and limited diffusion between cells, and following the harmonic mean approach we can again estimate that effective diffusion constant is 23-fold higher than the model value. However, since this applies for both TDIF and PLT/ANT this does not affect the size difference between the TDIF and PLT/ANT diffusion constants. Therefore, we performed additional simulations varying either TDIF or PLT/ANT diffusion rates, using strong sequestration settings (see below) (Fig. S10 B). We find that our results are reasonably robust to 2.5-fold increases in TDIF diffusion while showing significant deviations for 5-fold increases in TDIF diffusion results. In contrast, model outcomes are robust against a 10-fold increase in PLT/ANT diffusion rate which still results in spatially constrained ANT/PLT patterns with a clearly localized maximum, while for a 100-fold increase ANT/PLT patterns instead become smeared out, preventing localized cambium stem cell patterning. These results indicate that PLT/ANT diffusion rate could be increased 10-fold relative to default model parametrization, and that hence only a 2 order of magnitude smaller diffusion for PLT/ANT than for TDIF is required. However, if TDIF diffusion rate is further increased to better agree with experimental data concomitant with increases in TDIF turnover (see above), this difference would further increase.

To justify differences in TDIF and PLT/ANT diffusivity let us consider both differences in TDIF peptide and PLT/ANT protein properties and in where or how their transport is taking place. ANT and PLT5 proteins (555-558 amino acids) are far larger than the small TDIF peptides (12 aac). Assuming 110 Dalton per amino acid this results in a weight of approximately 61kDa for ANT/PLT5 and of 1.4kDa for TDIF. Next, assuming globular protein shape and assuming that 10kDa corresponds to a globular radius of 1.59nm this implies a radius of 2.9nm for ANT/PLT5 and 0.82nm for TDIF (for details see Appendix 2). Following the Stokes-Einstein relation the 3.5 larger radius of ANT/PLT5 compared to TDIF should already result in a 3.5 slower diffusion. Combined with the likely non-perfectly globular shape of particularly larger proteins like ANT/PLT5 this results in an order of magnitude difference in diffusion rates. On top of this TDIF is a signaling molecule that is excreted and diffuses in the apoplast, whereas ANT/PLT5 are transcription factors that need to leave the nucleus, diffuse in the cytoplasm and then enter the plasmodesmatal neck region to diffuse from cell to cell through the narrow plasmodesmatal sleeve. Currently we do not have data to determine whether ANT/PLT5 sizes exceed the size exclusion limit of the plasmodesmata in the cambium, nor whether ANT/PLT5 plasmodesmata transport involves protein unfolding or plasmodesmatal regulation. However, given the approximately 2.9nm molecular radius diffusional hindrance is expected to occur and can easily result in a further 10-100 fold reduction in diffusion rates. Combined, the size difference and the difference in where/how transport is taking place, this is expected to result in substantial differences in diffusion rates justifying the modeled differences between TDIF and ANT/PLT diffusion rates (see **table S4**).

Maximum HD-ZIP III repression versus strong sequestration settings

In **(fig. S9; and Fig. 4)** of the main manuscript text we compare two alternative model settings. Specifically, we used either the maximum HD-ZIP III' repression of ANT **(Fig. 4, A and E; fig. S9C)** or we used the "strong sequestering" parameter values (**Fig. 4, B and F; fig. S9D**) to investigate the relevance of regulatory interactions versus immobilization of TDIF through PXY mediated sequestration for robust cambium patterning.

For the maximum HD-ZIP III simulations, to enable us to focus on the importance of regulatory interactions we omitted effective TDIF sequestration, using multicellular versions of equations 1*, 2* and 3* rather than 1, 2 and 3 (for explanation see above). Note that in theory a similar effect of strongly reduced TDIF sequestration while maintaining effective ANT/PLT induction can be achieved through reducing the binding of TDIF to PXY (increased K_d), while simultaneously introducing a compensatory increase in the effectiveness of PXY-TDIF mediated ANT and PLT5 expression (lowering $K_{C,A}$ and $K_{C,P}$).

In contrast, under the strong sequestration settings, to focus on the importance of TDIF immobilization through sequestration we reduced the relevance of regulatory interactions for patterning. To achieve this, under these settings HD-ZIP III does not repress the PXY-TDIF based expression of ANT, and exclusively represses the auxin fraction, effectively halving the maximum achievable repression. To further enhance sequestration, we lowered the K_{off} from 0.1 to 0.02.

Variable gradients

To investigate the capacity of the network to robustly integrate and respond to various auxin and TDIF signaling inputs, we varied the auxin and TDIF production levels in a 3 cells wide cambium (5 cells in total) **(fig. S12)**. In this larger cambium there is more room for differences in spatial overlap of gradients for different auxin gradient and TDIF production and diffusion parameter settings (**table S6**). These simulations used the strong sequestration parameters from **table S5**. We ascribe cell fates to the cells based on the cell fate threshold values section as described above.

Numerical procedures

Differential equations were solved using simple Euler forward integration with a time step of 0.25s, and for the spatial 1D model a space step of 0.5 microm. For the spatial model no-flux boundary conditions were used. As initial conditions all protein levels for ANT, PLT5, PXY, TDIF, PXY-TDIF complex and HD-ZIP III were set to zero. Simulations were run for 60h of simulated time. Results shown represent steady state dynamics.

Appendix 1

Differential equations

Let us first recap the relevant differential equations:

$$\frac{dX}{dt} = \frac{p_X \cdot a^2}{a^2 + K_{a,X}^2} \cdot \left(\left(1 - f_{P,X}\right) + \frac{f_{P,X}}{1 + P^2/K_{P,X}^2} \right) - d_X \cdot X - K_{\mathrm{on}} \cdot X \cdot T + K_{\mathrm{off}} \cdot C$$

where $p_X, d_X, K_{a,X}, K_{P,X}, K_{\mathrm{on}}, K_{\mathrm{off}} \in \mathbb{R}^+$, $f_{P,X} \in \mathbb{R}^+$ and $a(t)$ is provided as an input.

$$\frac{dT}{dt} = p_T - d_T \cdot T - K_{\mathrm{on}} \cdot X \cdot T + K_{\mathrm{off}} \cdot C$$

$$p_T, d_T \in \mathbb{R}^+$$

$$\frac{dC}{dt} = K_{\mathrm{on}} \cdot X \cdot T - K_{\mathrm{off}} \cdot C - d_C \cdot C$$

$$d_C \in \mathbb{R}^+$$

$$\frac{dP}{dt} = \frac{p_P \cdot C^2}{C^2 + K_{CP}^2} - d_P \cdot P$$

$$p_P, d_P, K_{CP} \in \mathbb{R}^+$$

We will use $X_\infty$to indicate the steady state value of X, T_∞ to indicate the steady state value of T, etc. We aim to solve for $\{X_\infty, T_\infty, C_\infty, P_\infty\}$ excluding $\{H_\infty, A_\infty\}$; the first set is co-dependent and needs to be solved simultaneously. We will show below that T_∞, C_∞ and P_∞ can be written as a function of X_∞. This implies that to determine the number of different equilibria we can focus on solving X_∞. Note that $\{H_\infty, A_\infty\}$ are uncoupled since $H_\infty = g(a_\infty)$ (it is determined solely by the input $a(t)$) while $A_\infty = h(H_\infty, a_\infty, C_\infty) = h(X_\infty)$ (there is one value of A for each value of X) and is not impacting X_∞. Thus, A does not contribute to the number of fixed points for the system of ODEs.

Steady-states

We can directly solve for C_∞:

$$C_\infty = \frac{K_{\text{on}} \cdot X_\infty \cdot T_\infty}{K_{\text{off}} + d_C}$$

To solve for T_∞, we set $\frac{dT}{dt} + \frac{dC}{dt} = 0$

$$0 = p_T - d_T \cdot T_\infty - d_C \cdot C = p_T - d_T \cdot T_\infty - d_C \cdot \frac{K_{\text{on}} \cdot X_\infty \cdot T_\infty}{K_{\text{off}} + d_C}$$

and thus:

$$T_\infty = \frac{p_T}{d_T + d_C \cdot \frac{K_{\text{on}} \cdot X_\infty}{K_{\text{off}} + d_C}} = \frac{p_T \cdot K_{\text{off}} + p_T \cdot d_C}{d_T \cdot K_{\text{off}} + d_T \cdot d_C + d_C \cdot K_{\text{on}} \cdot X_\infty} = \frac{\alpha}{X_\infty + \beta}$$

where $\alpha := \frac{p_T \cdot K_{\text{off}} + p_T \cdot d_C}{d_C \cdot K_{\text{on}}}$ and $\beta := \frac{d_T \cdot K_{\text{off}} + d_T \cdot d_C}{d_C \cdot K_{\text{on}}}$ demonstrating that $T_\infty = k(X_\infty)$, substituting T_∞ in C_∞ then shows that $C_\infty = l(X_\infty)$.

P_∞ is:

$$P_\infty = \frac{p_P \cdot C_\infty^2}{d_P \cdot (C_\infty^2 + K_{CP}^2)} = \frac{p_P}{d_P} \cdot \frac{K_{\text{on}}^2 \cdot X_\infty^2 \cdot T_\infty^2}{K_{\text{on}}^2 \cdot X_\infty^2 \cdot T_\infty^2 + (K_{\text{off}} + d_C)^2 \cdot K_{CP}^2} = \frac{\gamma \cdot X_\infty^2 \cdot T_\infty^2}{X_\infty^2 \cdot T_\infty^2 + \delta}$$

where $\gamma := \frac{p_P}{d_P}$ and $\delta := \frac{(K_{\text{off}} + d_C)^2 \cdot K_{CP}^2}{K_{\text{on}}^2}$.

Substituting T_∞:

$$P_\infty = \frac{\gamma \cdot X_\infty^2 \cdot \left(\frac{\alpha}{X_\infty + \beta}\right)^2}{X_\infty^2 \cdot \left(\frac{\alpha}{X_\infty + \beta}\right)^2 + \delta} = \frac{\gamma \cdot \alpha^2 \cdot X_\infty^2}{(\alpha^2 + \delta) \cdot X_\infty^2 + 2 \cdot \beta \cdot \delta \cdot X_\infty + \beta^2 \cdot \delta} = \frac{X_\infty^2}{\epsilon \cdot X_\infty^2 + \zeta \cdot X_\infty + \eta}$$

where $\epsilon := \frac{\alpha^2 + \delta}{\gamma \cdot \alpha^2}$, $\zeta := \frac{2 \cdot \beta \cdot \delta}{\gamma \cdot \alpha^2}$ and $\eta := \frac{\beta^2 \cdot \delta}{\gamma \cdot \alpha^2}$ demonstrating that also $P_\infty = m(X_\infty)$.

To solve for X_∞, we set $\frac{dX}{dt} + \frac{dC}{dt} = 0$:

$$0 = \frac{p_X \cdot a_\infty^2}{a_\infty^2 + K_{aX}^2} \cdot \left(\left(1 - f_{P,X}\right) + \frac{f_{P,X}}{1 + P_\infty^2 / K_{PX}^2}\right) - d_X \cdot X_\infty - d_C \cdot C_\infty$$

Since we can rewrite C_∞ solely as a function of X_∞ as:

$$C_\infty = \frac{K_{\text{on}} \cdot X_\infty \cdot T_\infty}{K_{\text{off}} + d_C} = \frac{\alpha \cdot K_{\text{on}}}{K_{\text{off}} + d_C} \cdot \frac{X_\infty}{X_\infty + \beta}$$

we can expand equation [eq10] to:

$$0 = \frac{1}{d_X} \cdot \frac{p_X \cdot a_\infty^2}{a_\infty^2 + K_{aX}^2} \cdot \left(1 - f_{P,X}\right) + \frac{1}{d_X} \cdot \frac{p_X \cdot a_\infty^2}{a_\infty^2 + K_{aX}^2} \cdot \frac{f_{P,X}}{1 + P_\infty^2 / K_{PX}^2} - X_\infty - \frac{d_C}{d_X} \cdot \frac{\alpha \cdot K_{\text{on}}}{K_{\text{off}} + d_C} \cdot \frac{X_\infty}{X_\infty + \beta}$$

We define the following constants: $p_0 := \frac{1}{d_X} \cdot \frac{p_X \cdot a_\infty^2}{a_\infty^2 + K_{aX}^2} \cdot \left(1 - f_{P,X}\right)$, $p := \frac{f \cdot p_X \cdot a_\infty^2}{d_X \cdot (a_\infty^2 + K_{aX}^2)}$ and $d := \frac{d_C \cdot \alpha \cdot K_{\text{on}}}{d_X \cdot (K_{\text{off}} + d_C)}$ and thus equation [eq11] can be condensed to:

$$0 = p_0 + \frac{p}{1 + P_\infty^2/K_{PX}^2} - X_\infty - d \cdot \frac{X_\infty}{X_\infty + \beta}$$

Focusing on the term $\frac{p}{1+P_\infty^2/K_{PX}^2}$, we can expand it as:

$$\frac{p}{1 + P_\infty^2/K_{PX}^2} = \frac{p}{1 + \frac{X_\infty^4/K_{PX}^2}{(\epsilon \cdot X_\infty^2 + \zeta \cdot X_\infty + \eta)^2}} = \frac{p \cdot (\epsilon \cdot X_\infty^2 + \zeta \cdot X_\infty + \eta)^2}{(\epsilon \cdot X_\infty^2 + \zeta \cdot X_\infty + \eta)^2 + X_\infty^4/K_{PX}^2}$$

that expands to:

$$\frac{p}{1 + P_\infty^2/K_{PX}^2} = \frac{p\epsilon^2 X_\infty^4 + 2p\epsilon\zeta X_\infty^3 + p(2\epsilon\eta + \zeta^2)X_\infty^2 + 2p\zeta\eta X_\infty + p\eta^2}{(\epsilon^2 + 1/K_{PX}^2)X_\infty^4 + 2\epsilon\zeta X_\infty^3 + (2\epsilon\eta + \zeta^2)X_\infty^2 + 2\zeta\eta X_\infty + \eta^2}$$

This is:

$$\frac{p}{1 + P_\infty^2/K_{PX}^2} = \frac{a_4 X_\infty^4 + a_3 X_\infty^3 + a_2 X_\infty^2 + a_1 X_\infty + a_0}{b_4 X_\infty^4 + b_3 X_\infty^3 + b_2 X_\infty^2 + b_1 X_\infty + b_0}$$

where $a_0 := p\eta^2$, $a_1 := 2p\zeta\eta$, $a_2 := p(2\epsilon\eta + \zeta^2)$, $a_3 := 2p\epsilon\zeta$, $a_4 := p\epsilon^2$,

where $b_0 := \eta^2$, $b_1 := 2\zeta\eta$, $b_2 := 2\epsilon\eta + \zeta^2$, $b_3 := 2\epsilon\zeta$, $b_4 := \epsilon^2 + 1/K_{PX}^2$

$$0 = p_0 + \frac{a_4 X_\infty^4 + a_3 X_\infty^3 + a_2 X_\infty^2 + a_1 X_\infty + a_0}{b_4 X_\infty^4 + b_3 X_\infty^3 + b_2 X_\infty^2 + b_1 X_\infty + b_0} - X_\infty - \frac{d \cdot X_\infty}{X_\infty + \beta}$$

$$0 = \frac{c_6 X_\infty^6 + c_5 X_\infty^5 + c_4 X_\infty^4 + c_3 X_\infty^3 + c_2 X_\infty^2 + c_1 X_\infty + c_0}{(b_4 X_\infty^4 + b_3 X_\infty^3 + b_2 X_\infty^2 + b_1 X_\infty + b_0)(X_\infty + \beta)}$$

where

$$\begin{aligned}
c_0 &:= p_0 \beta b_0 + a_0 \beta \\
c_1 &:= p_0(b_0 + \beta b_1) - \beta b_0 - d b_0 + a_0 + a_1 \beta \\
c_2 &:= p_0(b_1 + \beta b_2) - b_0 - \beta b_1 - d b_1 + a_1 + a_2 \beta \\
c_3 &:= p_0(b_2 + \beta b_3) - b_1 - \beta b_2 - d b_2 + a_2 + a_3 \beta \\
c_4 &:= p_0(b_3 + \beta b_4) - b_2 - \beta b_3 - d b_3 + a_3 + a_4 \beta \\
c_5 &:= p_0 b_4 - b_3 - \beta b_4 - d b_4 + a_4 \\
c_6 &:= -b_4
\end{aligned}$$

This expression is equal to zero only when the numerator is zero. Since the numerator is a hexic polynomial, there must be 6 fixed points in $\mathbb{C}$ for X_∞.

Interpretation

Importantly, we are modeling a biological system. Thus, only positive, real valued equilibria are relevant. The question thus is how many of these equilibria may exist. For this we make use of the fact that the coefficients of the hexic polynomial are not unconstrained. Firstly, since:

$$p_X, d_X, K_{a,X}, K_{P,X}, K_{\mathrm{on}}, K_{\mathrm{off}}, \mathrm{a}, d_C, p_T, d_T, p_P, d_P, K_{C,P} \in \mathbb{R}^+$$
$$f_{P,X} \in [0,1]$$

From which follows that:

$$\alpha, \beta, \gamma, \delta. \epsilon, \zeta, \eta. p_0, p, d \in \mathbb{R}^+$$
$$a_0, a_1, a_2, a_3, a_4 \in \mathbb{R}^+$$
$$b_0, b_1, b_2, b_3, b_4 \in \mathbb{R}^+$$
$$c_0, c_1, c_2, c_3, c_4, c_5, c_6 \in \mathbb{R}$$

The complex conjugate root theorem thus applies: given a polynomial with real coefficients, if z is a root such that $\mathrm{Im}(z) \neq 0$, then its complex conjugate z^* will also be a root of this polynomial (complex roots come in pairs). Thus, given that complex roots necessarily occur in pairs, without taking the constraints of the problem into account, there could be zero, two, four or six real roots.

To investigate whether one or more equilibria exist in $\mathbb{R}^+$ we applied a heuristic approach. We sampled random parameter values (drawn uniformly from $U(0{,}10 \times v_i)$, where v_i is the parameter value used in the final model settings (tables S1-3). An exception is $f_{P,X}$ which was sampled from $U(0{,}1)$. The number of parameter value combinations sampled was $n_{\mathrm{sampling}} = 10^6$, for each of which we evaluated the number of real valued solutions r.

The number of real valued solutions for all the sampled parameter combinations are shown in the table below:

$R^-: 1; R^+: 1$	$R^-: 3, R^+: 1$
999063	937

These numbers support the high likelihood of a single equilibrium existing in R^+.

Phase plane analysis

As an alternative to solving for the equilibrium of our system and to further proof there is only a single equilibrium in R^+, we performed a graphical phase plane analysis to determine null clines and their points of intersection and thereby the number of equilibria in R^+. For this we needed to reduce our model to 2 dimensions. As before we ignored *H* and *A*, focussing on *X, T, C* and *P,* which together constitute a 4 dimensional system. We reduced this to a 2 dimensional system by taking a so-called quasi steady state assumptions for both the C variable and the T variable, eliminating these as variables and replacing them by algebraic expressions. This procedure makes this problem tractable without affecting the steady-state properties of the system.

We previously showed that:

$$T_\infty = \frac{\alpha}{X_\infty + \beta}; \quad C_\infty = \frac{K_{\mathrm{on}} \cdot X_\infty \cdot T_\infty}{K_{\mathrm{off}} + d_C} = \frac{\alpha \cdot K_{\mathrm{on}}}{K_{\mathrm{off}} + d_C} \cdot \frac{X_\infty}{X_\infty + \beta}$$

Assuming quasi steady state, we can similarly replace T and C with the following algebraic expressions for T(X) and C(X):

$$\mathrm{T(X)} = \frac{\alpha}{\mathrm{X}+\beta}; \quad \mathrm{C(X)} = \frac{\alpha \cdot K_{\mathrm{on}}}{K_{\mathrm{off}} + d_C} \cdot \frac{\mathrm{X}}{\mathrm{X}+\beta}$$

Trivially, these expressions tend to T_∞ and C_∞ as $\mathrm{t} \to \infty$.

Next we need to find the null clines for X and P by solving for $\dot{X} \coloneqq \frac{dX}{dt} = 0$ and $\dot{P} \coloneqq \frac{dP}{dt} = 0$ while making use of the algebraic expressions for C and T.

For P this results in the following equation of the P null cline

$$P_{\dot{P}=0}(X) = \frac{X^2}{\epsilon \cdot X^2 + \zeta \cdot X + \eta}; \quad X \in \mathbb{R}^+$$

The P null cline thus corresponds to a monotonically increasing non-linear saturating function in the positive quadrant since

$$\frac{d}{dX} P_{\dot{P}=0}(X) = \frac{\zeta \cdot X^2 + 2 \cdot \eta \cdot \mathrm{X}}{(\epsilon \cdot X^2 + \zeta \cdot X + \eta)^2} > 0 \text{ if } \mathrm{X} \in \mathbb{R}^+$$

Writing an analytical expression for the X null cline is more complex:

$$\frac{dX}{dt} = \frac{p_X \cdot a_\infty^2}{a_\infty^2 + K_{aX}^2} \cdot \left(\left(1 - f_{P,X}\right) + \frac{f_{P,X}}{1 + \frac{P^2}{K_{PX}^2}} \right) - d_X \cdot X - d_C \cdot \frac{\alpha \cdot K_{\mathrm{on}}}{K_{\mathrm{off}} + d_C} \cdot \frac{X}{X+\beta} = 0$$

Which can be rewritten as

$$0 = p_0 + \frac{pK_{PX}^2}{K_{PX}^2 + P^2} - X - d \cdot \frac{X}{X+\beta}$$

where as before $p_0 := \frac{1}{d_X} \cdot \frac{p_X \cdot a_\infty^2}{a_\infty^2 + K_{aX}^2} \cdot \left(1 - f_{P,X}\right)$, $p := \frac{f \cdot p_X \cdot a_\infty^2}{d_X \cdot \left(a_\infty^2 + K_{aX}^2\right)}$ and $d := \frac{d_C \cdot \alpha \cdot K_{\mathrm{on}}}{d_X \cdot (K_{\mathrm{off}} + d_C)}$

this can be reordered as

$$\frac{pK_{PX}^2}{K_{PX}^2 + P^2} = p_0 + X + d \cdot \frac{X}{X+\beta}$$

rewritten as

$$\frac{pK_{PX}^2}{K_{PX}^2 + P^2} = \frac{p_0(X+\beta) + X(X+\beta) + dX}{X+\beta}$$

and next as

$$\frac{K_{PX}^2 + P^2}{pK_{PX}^2} = \frac{X+\beta}{p_0(X+\beta) + X(X+\beta) + dX}$$

inverted as

$$P^2 = \frac{pK_{PX}^2(X+\beta)}{p_0(X+\beta) + X(X+\beta) + dX} - K_{PX}^2$$

And finally written as

$$P_{\dot{X}=0}(X) = \pm K_{PX}\sqrt{\frac{p \cdot (X+\beta)}{p_0 \cdot (X+\beta) + X \cdot (X+\beta) + d \cdot X} - 1}$$

where only the positive expression is biologically relevant. This can be expanded as:

$$P_{\dot{X}=0}(X) = K_{PX}\sqrt{\frac{-X^2 + (p - p_0 - \beta - d) \cdot X + p \cdot \beta - p_0 \cdot \beta}{X^2 + (p_0 + \beta + d) \cdot \mathrm{X} + \mathrm{p}_0 \cdot \beta}} = K_{PX}\sqrt{\frac{P(X)}{Q(X)}}$$

defined in the domain of $S \coloneqq \{X \in \mathbb{R}^+ | P(X) > 0\}$ since $Q(X) > 0$ ($p_0, \beta, d \in \mathbb{R}^+$). To assess it potential monotonicity, we differentiate with respect to X and study its sign:

$$\frac{d}{dX} P_{\dot{X}=0}(X) = K_{PX} \frac{P'(X) \cdot \mathrm{Q(X)} - \mathrm{Q'(X)} \cdot \mathrm{P(X)}}{2\sqrt{\frac{P(X)}{Q(X)}}\, Q(X)^2}$$

Since for $X \in S$, both $P(X), Q(X) > 0$, the denominator is strictly positive in this domain. We thus focus on the sign of the numerator:

$$P'(X) \cdot \mathrm{Q(X)} - \mathrm{Q'(X)} \cdot \mathrm{P(X)} = -p \cdot (X^2 + 2\beta X + \beta^2 + \beta \cdot d) < 0$$

Since the expression for the X null cline describes a monotonically decreasing function while the expression for the P null cline describes a monotonically increasing function only a single point of intersection in R^+ is possible, proving there is only a single biologically relevant equilibrium in our system.

Appendix 2

The precise size of a specific protein will depend on the number and type of amino acids it contains and how these determine the shape the protein will fold into. To get an estimate of protein size (radius), typically the following approach is used:

1. It is assumed that the protein has a globular shape, and hence a volume that can be described as $V = \frac{4}{3}\pi r^3$, with V volume in nm^3 and r radius in nm.
2. It is assumed that the protein has an average protein density ρ in Da/nm^3 enabling the conversion between molecular weight and volume as $V = \frac{1}{\rho} MW$, where MW is the molecular weight of the protein in Dalton.

An explanation of this approach can also be found in the following documentation:
https://biologicalproceduresonline.biomedcentral.com/counter/pdf/10.1007/s12575-009-9008-x.pdf

Online different calculators for protein radius from molecular weight are available which use slightly different assumptions for the value of average protein density ρ in their calculations resulting in slightly different estimates for protein radius *r*.

We made use of the following two online calculators:
https://nanocomposix.com/pages/molecular-weight-to-size-calculator
https://www.fidabio.com/molecular-weight-to-size-protein-radius-calculator

The first website assumes a molecular density that results in a predicted 1.42nm radius for a globular protein of 10kDa, whereas the second website assumes a somewhat different molecular density that results in a predicted 1.78nm radius for a 10kDa globular protein. We decided to use an average value of a 1.59nm radius for 10kDa protein to calculate the radii for the TDIF peptide and ANT/PLT proteins.

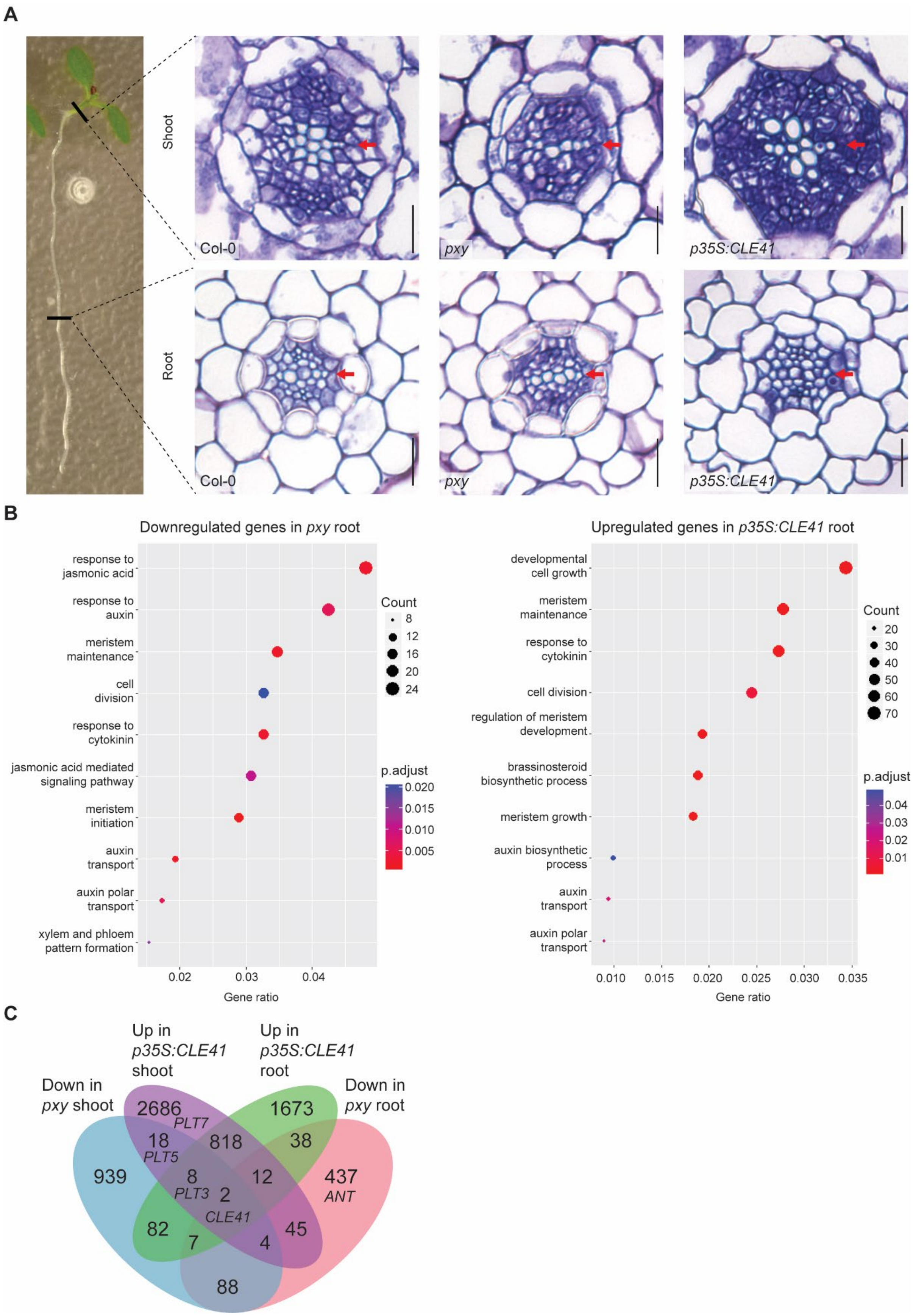
A
Shoot
Root
Col-0
pxy
p35S:CLE41
Col-0
pxy
p35S:CLE41
B
Downregulated genes in pxy root
response to jasmonic acid
response to auxin
meristem maintenance
cell division
response to cytokinin
jasmonic acid mediated signaling pathway
meristem initiation
auxin transport
auxin polar transport
xylem and phloem pattern formation
0.02
0.03
0.04
Gene ratio
Count
8
12
16
20
24
p.adjust
0.020
0.015
0.010
0.005
Upregulated genes in p35S:CLE41 root
developmental cell growth
meristem maintenance
response to cytokinin
cell division
regulation of meristem development
brassinosteroid biosynthetic process
meristem growth
auxin biosynthetic process
auxin transport
auxin polar transport
0.010
0.015
0.020
0.025
0.030
0.035
Gene ratio
Count
20
30
40
50
60
70
p.adjust
0.04
0.03
0.02
0.01
C
Up in p35S:CLE41 shoot
Up in p35S:CLE41 root
Down in pxy shoot
Down in pxy root
2686
PLT7
1673
18
PLT5
818
38
939
8
PLT3
2
CLE41
12
437
ANT
82
7
4
45
88

Fig. S1. Transcriptomic analysis of *pxy* and CLE41 overexpression

(A) Seedling material for the RNA-seq analysis. Left, an image of a seedling showing the position of cross section shown on the right. Cross-sections of 7-day old Wild type Col-0, *pxy, p35S:CLE41* of hypocotyls and roots. **(B)** Gene Ontology terms reduced in *pxy* and enriched in *p35S:CLE41* root respectively. Red arrows mark the primary xylem axis. (**C**) Venn diagram showing numbers of genes with differential expression in *pxy* and *p35S:CLE41* shoots or roots relative to Col-0 in 7-day-old seedlings. Genes upregulated in *p35S:CLE41* and down-regulated in *pxy*, were considered more likely to be PXY-signaling targets. Sections within the Venn diagram where *PLT3*, *PLT5*, *PLT7*, and *ANT* fall are marked. Scale bars 20 µm.

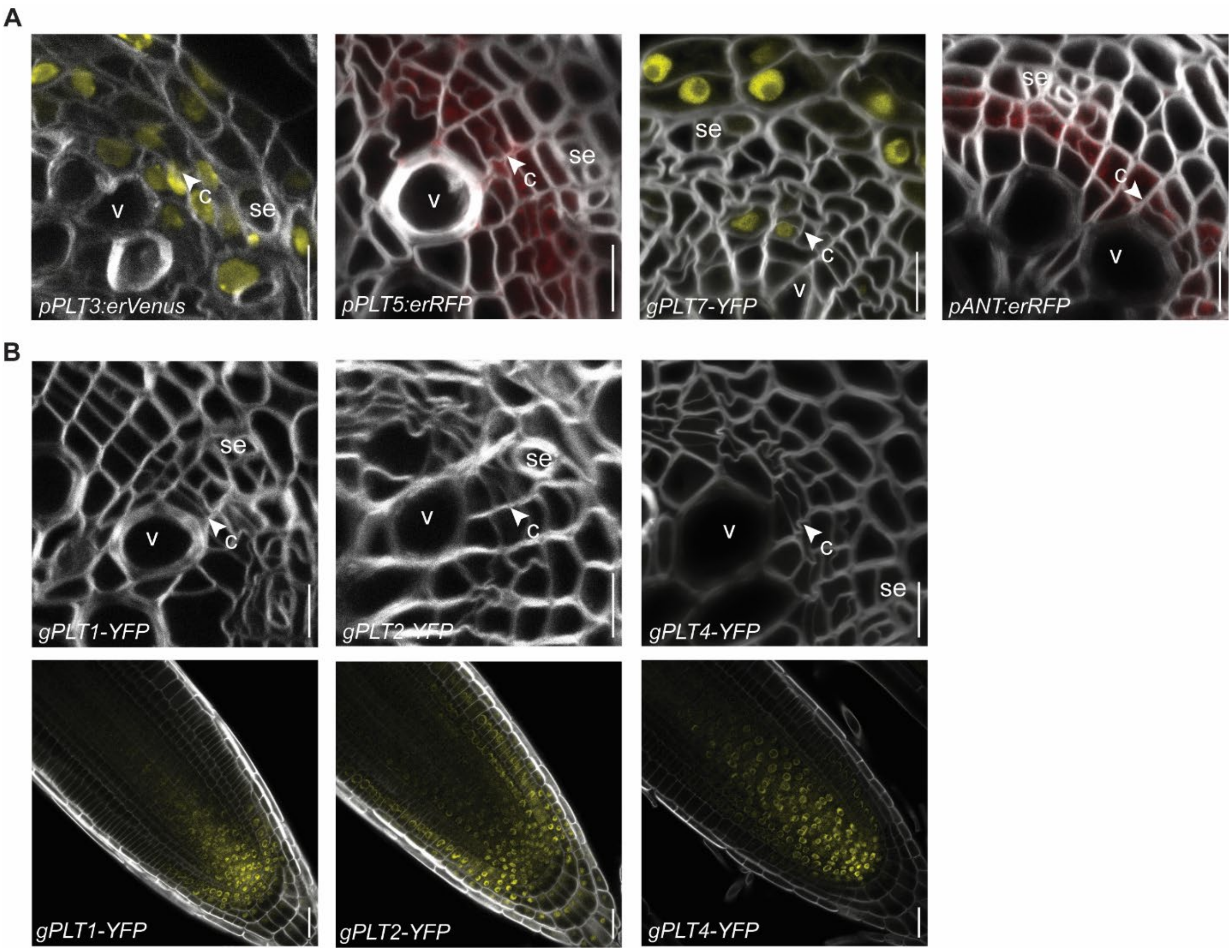

Fig. S2. Four *AIL/PLT*s are expressed in root cambium

(A) Confocal cross-sections of 14-day-old *pPLT3:erVenus, pPLT5:erRFP, gPLT7-YFP* and *pANT:erRFP* roots. **(B)** Confocal cross-sections of 14-day-old roots and longitudinal view of root tips of *gPLT1-YFP, gPLT2-YFP* and *gPLT4-YFP* show expression in root tip as previously reported (*18*), however they show no fluorescence in root vascular cambium. White arrowheads mark recent cell division. Vessels (v), cambium (c), sieve element (se). Scale bars 10 µm.

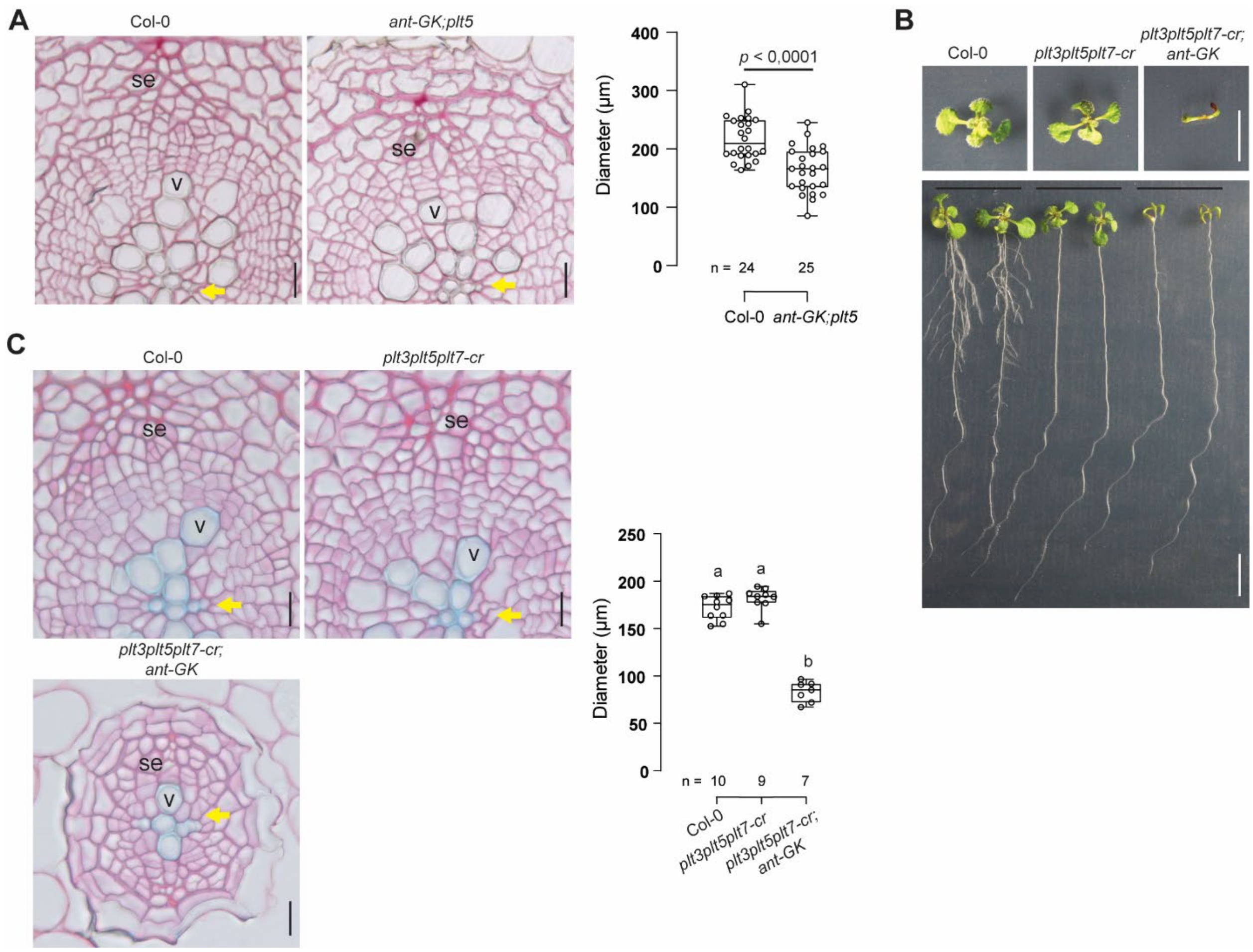

Fig. S3. Histological analysis of higher order *ail/plt* mutants generated by crossing.

(A) Cross section of 14-day-old Col-0 and *ant-GK;plt5* double mutant together with the quantification of the vascular diameter. **(B)** Gross morphology of 11-day-old Col-0, *plt3plt5plt7-cr* and *plt3plt5plt7-cr;ant-GK* seedlings. (**C**) Root cross-sections of 12-day-old Col-0, *plt3plt5plt7-cr*, and *plt3plt5plt7-cr;ant-GK.* Quantification of the vascular diameter presents on the right panel. Significance difference was tested by Student t-test in (A). Letters indicate significant differences using one-way ANOVA with a Tukey post hoc test in (C). Yellow arrows mark the primary xylem axis. Vessels (v), sieve elements (se), Scale bars 10 µm (A and C) and 1 cm (B).

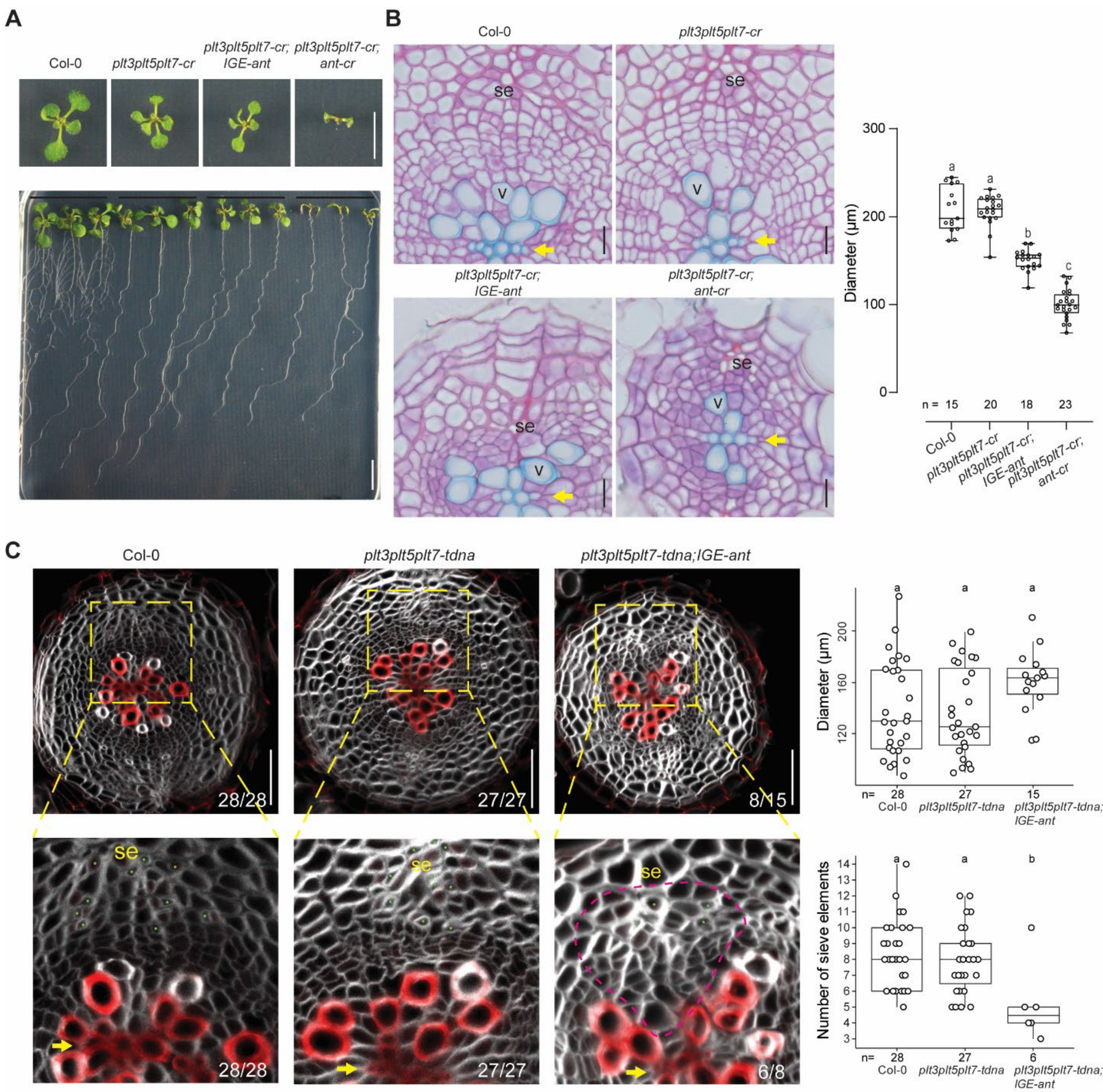

Fig. S4. Histological analysis of higher order *ail/plt* mutants generated by gene editing

(**A**) Gross morphology of 11-day-old plants of Col-0, *plt3plt5plt7-cr*, *plt3plt5plt7-cr;IGE-ant*, and *plt3plt5plt7-cr;ant-cr*. (**B**) Root cross-sections of 13-day-old Col-0, *plt3plt5plt7-cr*, *plt3plt5plt7-cr;IGE-ant*, and *plt3plt5plt7-cr;ant-cr* seedlings. The quantification of vascular tissue diameter is shown on the right. (**C**) Confocal cross-section of 13-day-old roots of Col-0, *plt3plt5plt7-tdna, plt3plt5plt7-tdna;IGE-ant* and the quantification of the vascular tissue diameter and the number of sieve elements (right panels). 8/15 of *plt3plt5plt7-tdna;IGE-ant* roots showed sectors without vessel production. 6/8 of these sectors occurred in the position of phloem pole, and these 6 sectors were used in quantification of sieve elements (lower right panel). Inset images show reduced number of sieve elements (marked with green dot) and the sector marked with dotted line (magenta). Cell walls are stained with SR2200 (grey), lignified cell walls are stained with 0.1% basic fuchsin (red). Letters indicate significant differences using one-way ANOVA with a Tukey post hoc test in (B), or using Kruskal-Wallis with Dunn post hoc test in (C). Numbers in (C) represent the frequency of the observed phenotypes. Yellow arrows mark the primary xylem axis. Vessels (v), sieve elements (se), Scale bars 10 µm (B), 50 µm (C) and 1 cm (A).

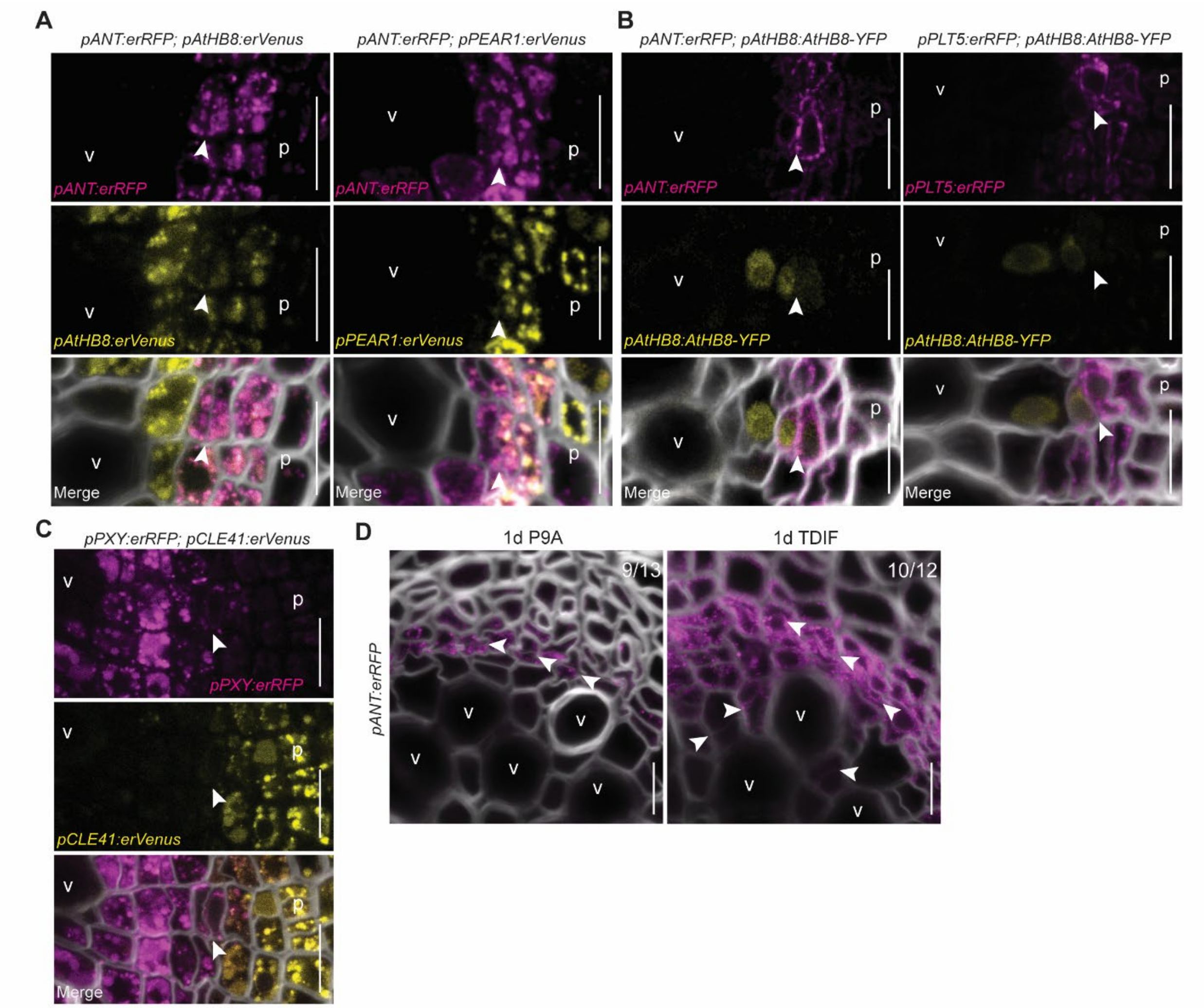

Fig. S5. Expression patterns of key cambial regulators

(A) Confocal cross-sections of 12-day-old roots expressing *ANT* double markers. (**B**) Confocal cross-sections of 13-day-old roots expressing *pAtHB8:AtHB8-YFP* double markers. **(C)** Confocal cross-sections of 14-day-old *pPXY:erRFP;pCLE41:erVenus* root. **(D)** Confocal cross-sections of *pANT:erRFP* after 1-day TDIF treatment in 14-day-old plants. Numbers in (D) represent the frequency of the observed phenotypes. White arrowheads mark recent cell division. Phloem (p). Vessels (v). Scale bars 10 µm (A to D).

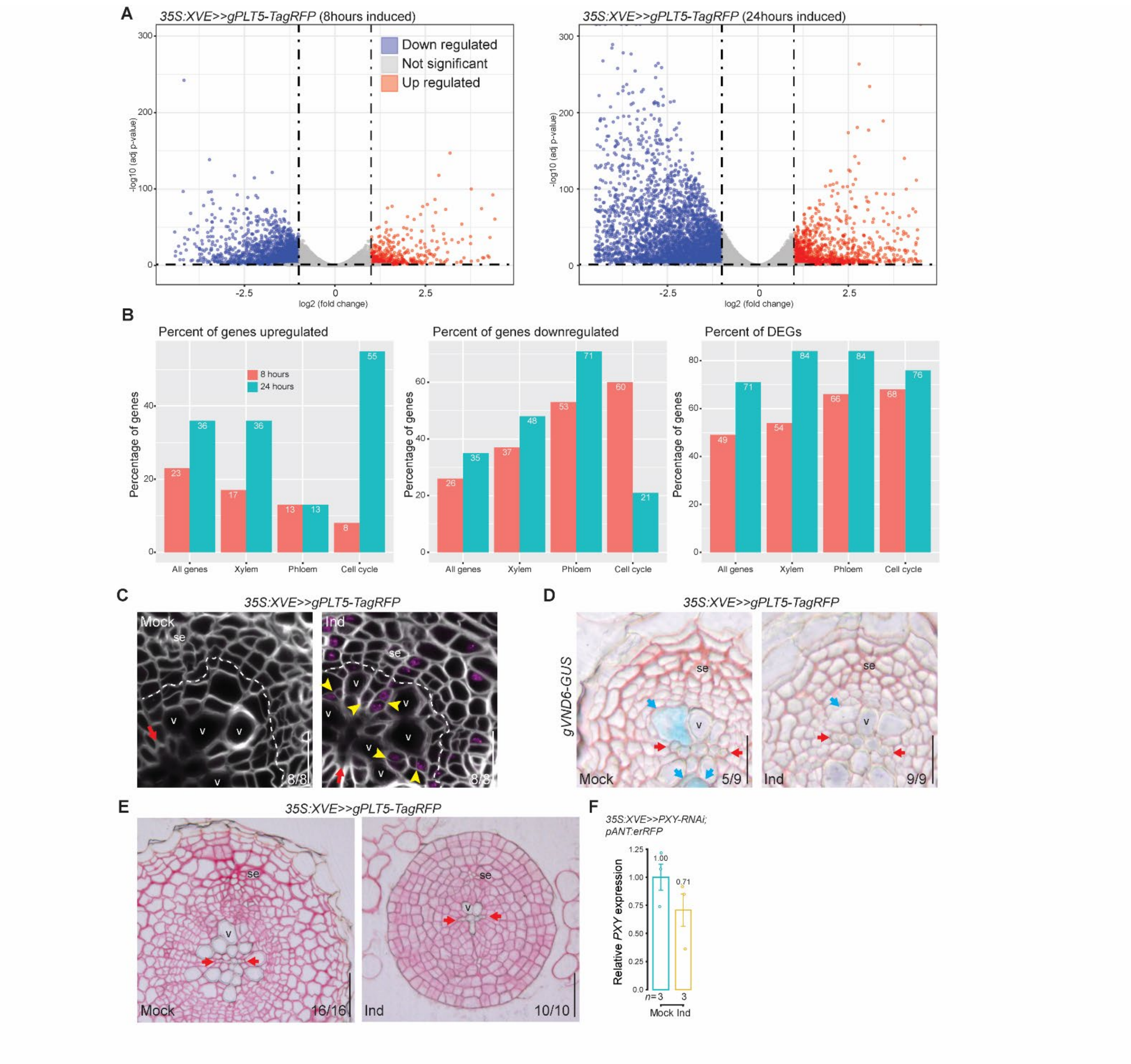

Fig. S6. Analysis of the consequences of inducible *PLT5* overexpression

(A) Volcano plot of all the transcript after 8 hours or 24 hours induction of *35S:XVE>>PLT5-TagRFP* RNA-seq. The dotted horizontal line corresponds to a Benjamini–Hochberg corrected significance of Padj Value <0.05. The dotted vertical lines bound the minimal fold-change for the most-differentially-expressed genes. **(B),** Bar plot shows the percentage of the genes that are upregulated, downregulated and differentially expressed genes (DEGs) in categories of All genes, xylem, phloem and cell cycle genes for 8 and 24 hours using PValue <0.05. **(C),** Confocal cross-section of *35S:XVE>>PLT5-TagRFP* after 2-day induction (Ind) (in 12-day-old plants) showing ectopic cell division in xylem parenchyma. These ectopic divisions are not present in the Mock. Most recent cell divisions in cambium are marked with dotted lines (white). **(D),** Cross-section of *35S:XVE>>PLT5-TagRFP;gVND6-GUS* after 2-day induction (in 8-day-old plants). **(E),** Cross-section of *35S:XVE>>PLT5-TagRFP* after 7-day induction (in 8-day-old plants). **(F),** RT-qPCR showing the reduced *PXY* transcript levels in *35S:XVE>>PXY-RNAi;pANT:erRFP*. Barplot shows average with ± sd. Numbers in panels (C to E) represents the frequency of the observed phenotypes. Yellow arrowheads mark recent, ectopic cell division, red arrows mark the primary xylem axis, and blue arrows marks the expanding xylem vessels. Vessels (v). Sieve elements (se). Estradiol induction (Ind). Scale bars 20 μm (C to E).

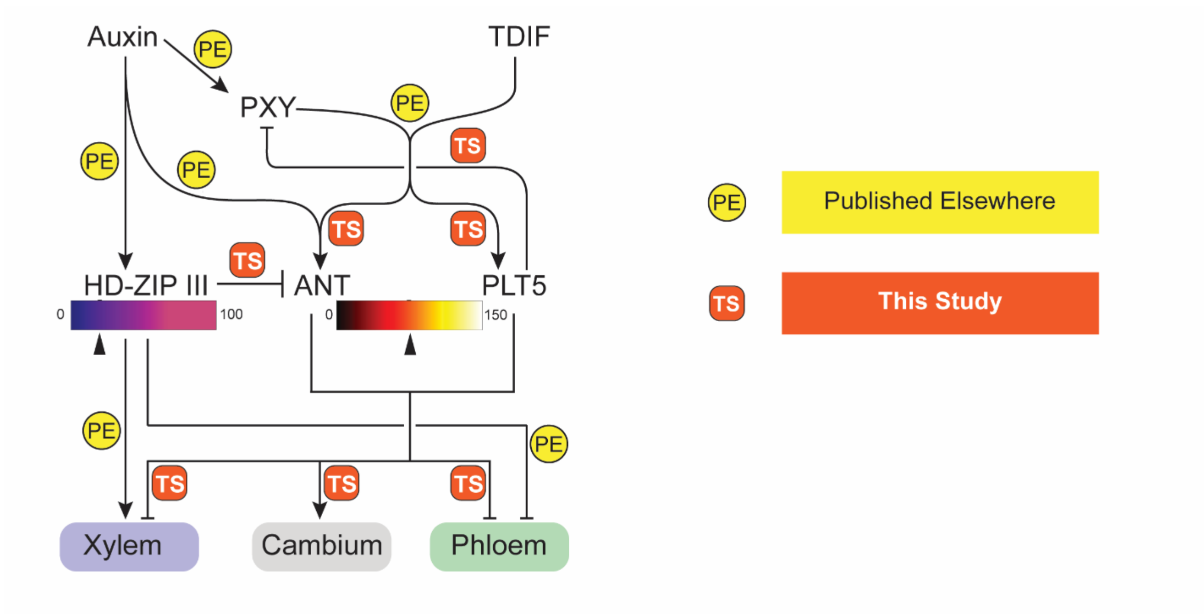

Published Elsewhere	Auxin ->PXY	Smetana et al., 2019
	PXY & TDIF	Hirakawa et al., 2008; Etchells et al., 2010; Morita et al., 2016
	Auxin -> HD-ZIP III	Smetana et al., 2019; Donner et al., 2009; Ursache et al., 2014
	Auxin -> ANT	Smetana et al., 2019; Yamaguchi et al., 2013
	HD-ZIP III -> Xylem	Zhong and Ye, 1999; Smetana et al., 2019; Ohashi-Ito et al., 2005; Carlsbecker et al., 2010
	HD-ZIP III -| Phloem	Smetana et al., 2019; Miyashima et al., 2019

This Study	PXY-TDIF -> ANT	Fig. 1B; fig. S5D
	PXY-TDIF -> PLT5	Fig. 1B; Fig. 3A
	PLT5 -| PXY	Fig. 2B; Fig. 3D
	HD-ZIP III -| ANT	Fig. 3E
	ANT/PLT5 -| Xylem	Fig. 2, F and G; fig. S6E
	ANT/PLT5 -> Cambium	Fig. 2, D and E; fig. S6C
	ANT/PLT5 -| Phloem	Fig. 2, F and G; fig. S6E

Fig. S7. Signaling network in vascular cambium used in the modelling

Top panel indicates the same network of modelled regulatory interactions driving cambial cell fate decision making as shown in Fig. 3C. Bottom panels indicate the experimental support for the different incorporated regulatory interactions categorized according to being published elsewhere (yellow, PE) or observed in this current study (orange, TS).

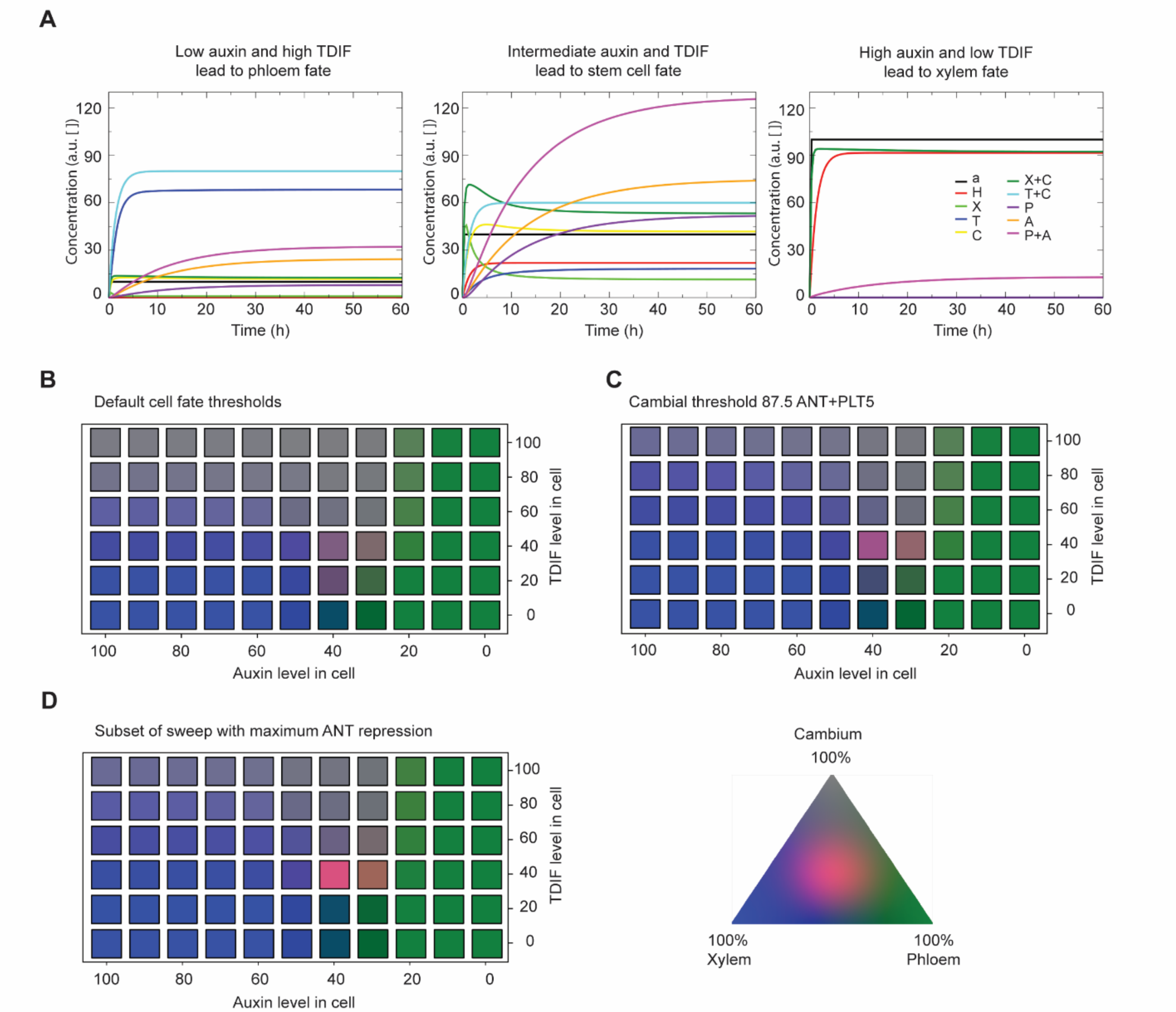

Fig. S8. Fate map for large scale Parameter Sweeps

(A) Model simulation examples illustrating convergence to alternative cell fates depending on varying auxin and TDIF input levels. a=auxin, H=HD-ZIP III, X=PXY, T=TDIF, C=TDIF-PXY complex, P=PLT5, A=ANT. Parameter settings used are the final values shown in Tables S1-S5, combined with maximum HD-ZIP III mediated ANT repression, and normal TDIF-PXY complex formation dynamics (K_d=5). Left figure: auxin level of 10 and (total) TDIF level of 80 leads to phloem fate (HD-ZIP III<30 and PLT5+ANT<75); middle figure: auxin level of 40 and (total) TDIF level of 60 leads to stem cell fate (PLT5+ANT>75); right figure: auxin level of 100 and (total) TDIF level of 0 leads to xylem fate (HD-ZIP III>30). Left figure: Since PXY (X) and HD-ZIPIII (H) are both auxin-dependent, X is plotted on top of H, and thus H is not visible. Similarly, in the right figure in absence of TDIF (T), both T, TDIF-PXY complex (C), total TDIF (T+C) and PLT (P) equal zero, P is plotted on top making T, C, and T+C not visible, while free PXY (X) and total PXY (X+C) are equal causing X to not be visible and ANT (A) and ANT plus PLT (P+A) being equal causing A to not be visible. (**B**) Fate map of overall parameter sweep including both strong and weak HD-ZIP III mediated ANT repression for a cambial fate threshold of 75. For the range and sampling interval of parameter values used for the parameter sweep see Supplementary Modeling Methods. Each Auxin-TDIF combination is colored according to the fraction of simulations that acquire xylem, cambium, or phloem identity according to the color triangle. **(C)** Alternative fate map of an overall parameter sweep using a cambial fate threshold of 87.5. Raising this threshold to 87.5 reduces the cambial domain but retains the same qualitative behavior as shown in (B). **(D)** Fate map for a parameter sweep with default (same as in (B)) cell fate thresholds but now constrained to maximum HD-ZIP III mediated ANT repression (see Modelling Methods), showing an expansion of xylem over cambial fate for high auxin and high TDIF levels, when compared to (B).

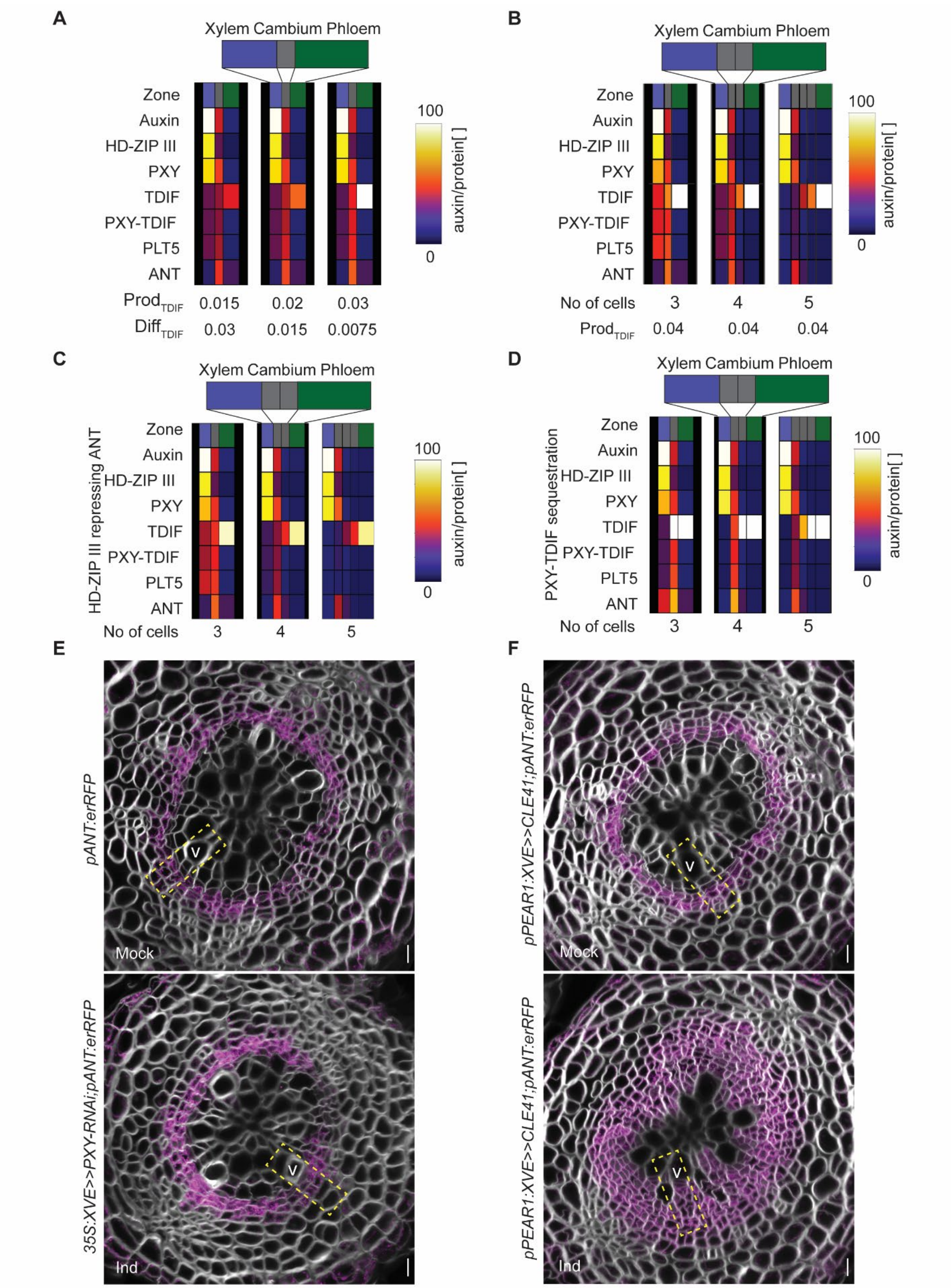

Fig. S9. Robustness to variable TDIF gradients and cambial size.

(**A**) Robust cell fate decision making in a 3-cell tissue for variable production and diffusion rates of TDIF for maximum HD-ZIP III mediated ANT repression and moderate TDIF sequestration. (**B-D**) Robustness of cell fate decision making to variation in cambial cell number for the same settings as in (A) except that TDIF production was fixed to a value of 0.04 (B), for maximum HD-ZIP III mediated ANT repression in absence of TDIF sequestration (C), and for low (halved) HD-ZIP III mediated ANT repression combined with enhanced TDIF sequestration (5-fold reduced TDIF-PXY dissociation) (D). C and D are both for default TDIF production and diffusion rates. For A, B and D Equations 1, 2 and 3 were used, while for C Equations 1*, 2*, 3* were used (for details see Supplemental Methods) (**E-F**) Uncropped images presented in Fig. 4C and Fig. 4G. The yellow dashed square shows the region that is magnified in Fig. 4C and Fig. 4G. Vessels (v). Scale bars 10 µm.

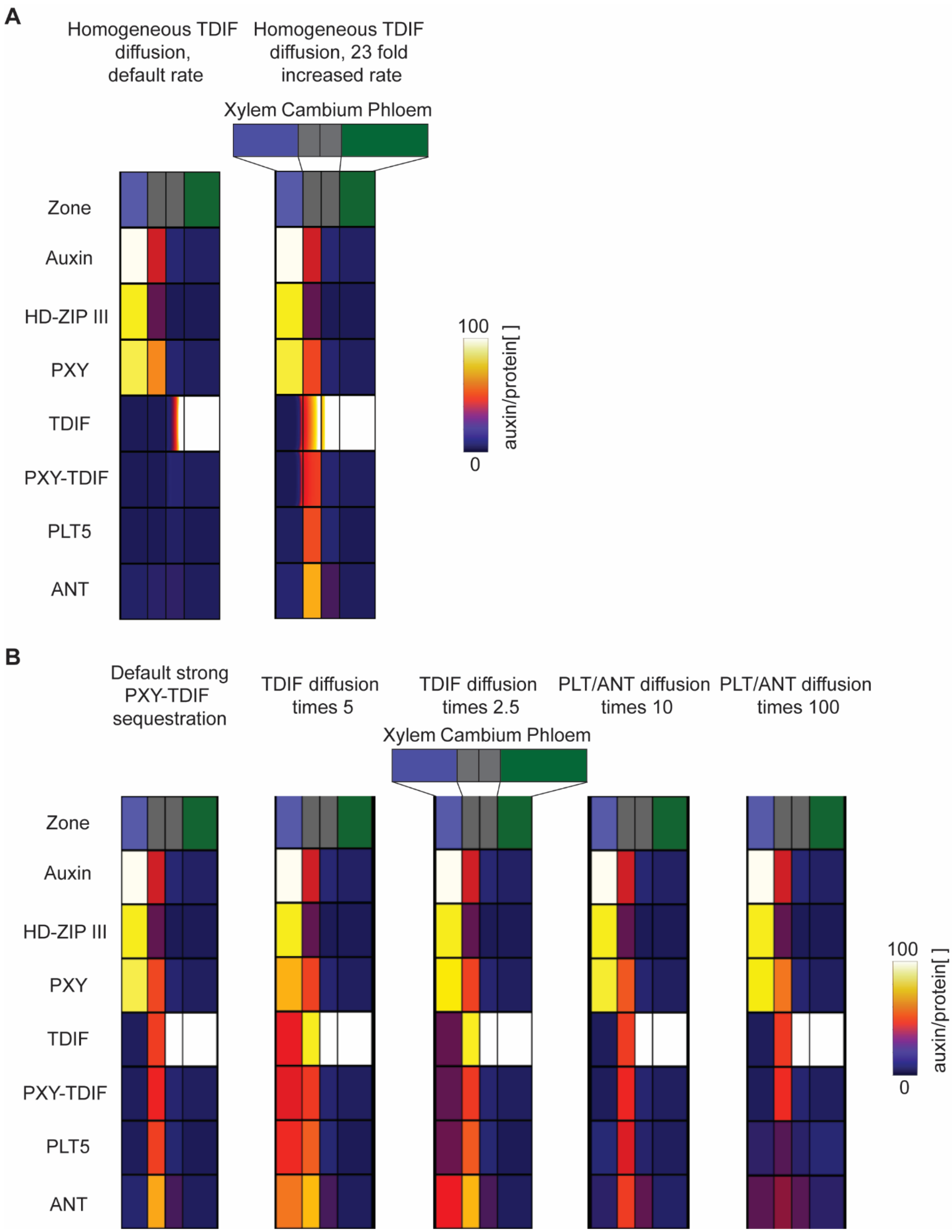

Fig. S10. Robustness of cambium patterning to variations in diffusion implementation and rates of TDIF and PLT/ANT. (**A**) Cambium patterning for alternative TDIF diffusion implementation in which

TDIF diffuses homogeneously across the tissue instead of only in between cells. Left: cambium patterning if the same diffusion coefficient is used as for the default TDIF diffusion implementation. Right: cambium patterning for a 23 fold increased diffusion coefficient. (**B**) From left to right: cambium patterning for the default strong sequestration modeling setting and default diffusion implementation; cambium patterning for a 5 fold increase in TDIF diffusion rate; cambium patterning for a 2.5 fold increase in TDIF diffusion rate; cambium patterning for a 10 fold increase in PLT/ANT diffusion rate; and cambium patterning for a 100 fold increase in PLT/ANT diffusion rate.

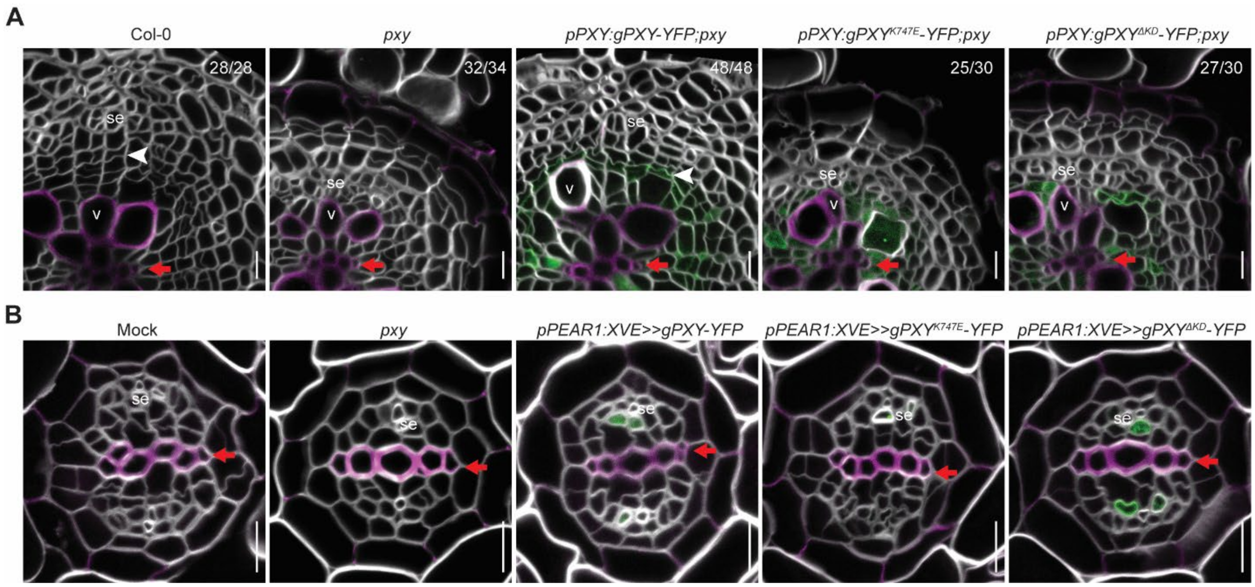

Fig. S11. Complementation analysis of different versions of PXY.

(A) Complementation of the *pxy* phenotype with different versions of PXY-YFP. Confocal cross-sections of 14-day-old Col-0, *pxy*, *pPXY:gPXY-YFP;pxy, pPXY: gPXY*^{K747E}*-YFP;pxy* and *pPXY:gPXY*$^{\Delta KD}$*-YFP;pxy* roots While the transgenic line containing *pPXY* complements the *pxy* mutant, lines containing *PXY*^{K747E} or *PXY*$^{\Delta KD}$ failed to do so, and thus, show *pxy*-like stem cell differentiation phenotype: a vessel (v) adjacent to a sieve element (se). The numbers in the top right corner of subpanels represent the frequency of the observed phenotype. **(B)** Expression of PXY-YFP variants after 1d of induction. Confocal root cross sections of 6-day-old mock, *pxy*, and 5-day-old *pPEAR1:XVE>>gPXY-YFP*, *pPEAR1:XVE>>gPXY*^{K747E}*-YFP* and *pPEAR1:XVE>>gPXY*$^{\Delta KD}$*-YFP* seedlings induced for 1 day. Note, *pxy* phenotype is typically not yet visible in 7-day-old roots (such as *pxy* in panel B). Cell wall stained with SR2200 (grey), lignified cell walls are stained with 0.1% basic fuchsin (magenta)**.** White arrowheads mark recent cell divisions. Red arrows mark the primary xylem axis. Sieve element (se), xylem vessels (v). Scale bars 10 µm (A and B).

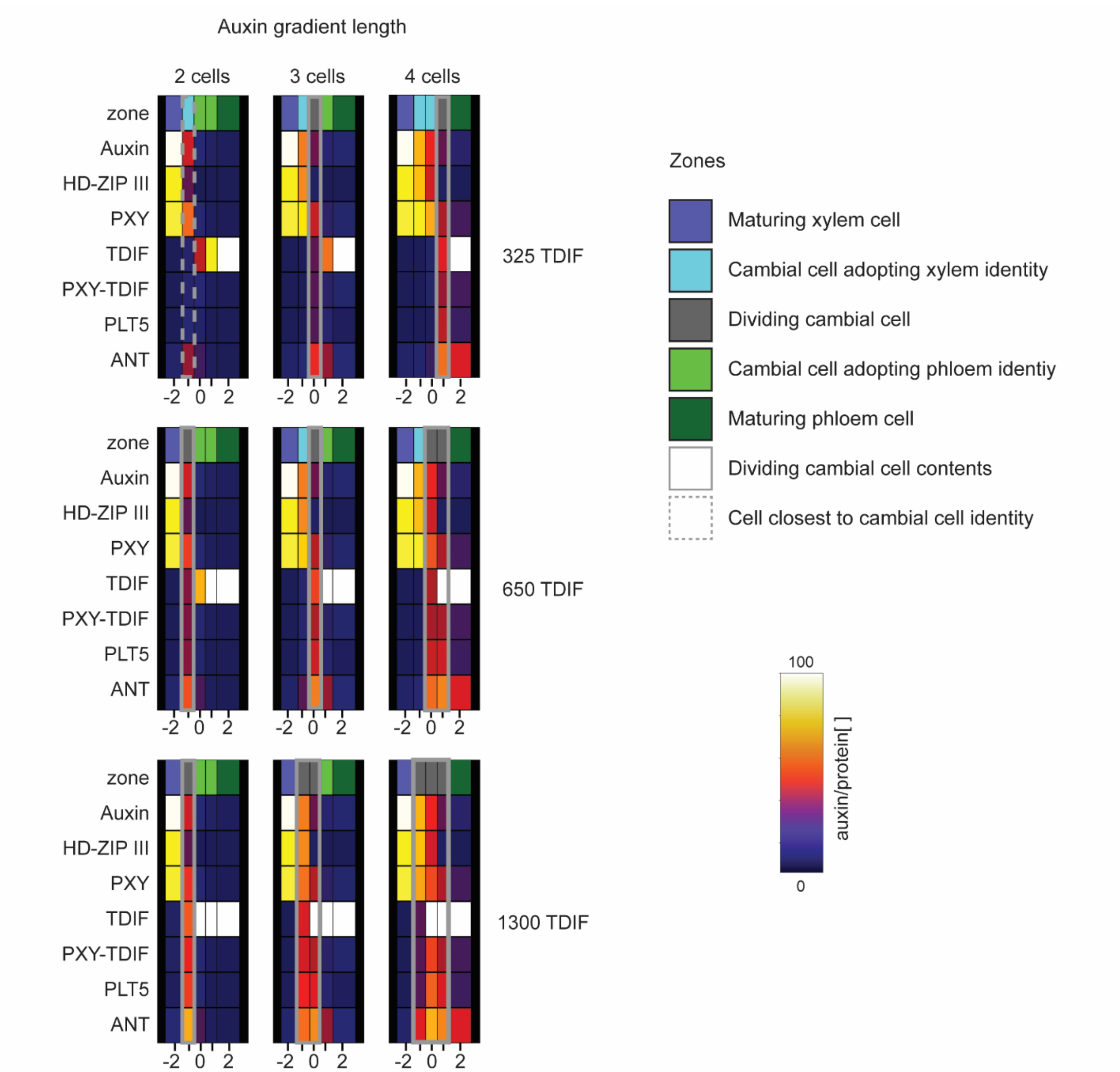

Fig. S12. Flexibility to respond to variation in auxin and TDIF gradients in variable size cambium

Overview of cell fate decision making in a 3 to 5-cell vasculature exposed to variable auxin gradient lengths (left to right) and variable TDIF production levels in the phloem (top to bottom) under strong sequestration parameter settings. Gray bars show which cells will retain cambial identity (grey zone) as a result of expressing sufficient ANT+PLT5. Light blue cells express sufficient HD-ZIP III to differentiate to xylem, while light green cells lack both high levels of ANT+PLT5 and HD-ZIP III and will thus differentiate to phloem. A strong auxin gradient (top right) pushes the cambial cell identity towards the phloem, allowing differentiation of new xylem cells. A strong TDIF signal pushes the cambial cell identity towards the xylem (bottom left) allowing phloem cells to differentiate. A combination of these two gradients allows for a larger total overlap (bottom right) that generates a larger cambium. When the overlap is too weak (top left) a meristem cannot be sustained. The dashed line indicates the highest current ANT+PLT5 level, where a smaller cambium (with increased PXY-TDIF overlap) could be maintained.

table S1. Constant valued model parameters, their values and units.

Parameter name	Parameter value	Unit
p_H	0.02	$[]s^{-1}$
d_H	0.0002	s^{-1}
p_A	0.002	$[]s^{-1}$
d_A	0.00002	s^{-1}
p_P	0.002	$[]s^{-1}$
d_P	0.00002	s^{-1}
K_{on}	0.02	$[]^{-1}s^{-1}$
K_{off}	0.1	s^{-1}
p_X	0.002	$[]s^{-1}$
d_X	0.00012	s^{-1}
d_C	0.00012	s^{-1}
d_T	0.0002	s^{-1}

table S2. Parameters for auxin and HDZIPIII, the range of values investigated, sampling interval used and values used for final model settings and units.

Parameter name	Parameter range	Interval	Final value	Unit
$K_{a,X}$	15-35	5	25	[]
$K_{a,H}$	30-70	10	55	[]
$K_{a,A}$	15-35	5	20	[]
$K_{H,A}$	30-50	5	50	[]
$m_{a,A}$	0.1-0.4	0.05	0.2	Dimensionless
$m_{C,A}$	1- $m_{a,A}$	0.05	0.8	Dimensionless
$r_{H,a}$	0.4-1.	0.1	1.0	Dimensionless
$r_{H,C}$	$r_{H,a}$	0.1	1.0	Dimensionless

table S3. PXY-TDIF dependent parameters, the range of values investigated, sampling interval used and values used for final model settings and units.

Parameter name	Parameter range	Interval	Final value	Unit
$K_{C,A}$	15-35	5	20	[]
$K_{C,P}$	20-40	5	40	[]
$K_{P,X}$	30-50	5	50	[]
$f_{P,X}$	0.3-0.6	0.05	0.6	[]

table S4. Diffusion parameters

Parameter name	Parameter values	Unit
D_T	0.00094	μm^2 s^{-1}
D_A	0.00000125	μm^2 s^{-1}
D_P	0.00000125	μm^2 s^{-1}

table S5. Alternative parameter regimes

Parameter name	Maximum HD-ZIP III repression value	Strong sequestering value	Unit
p_T	0.03	0.13	[]s^{-1}
$r_{H,a}$	1.0	1.0	Dimensionless
$r_{H,X}$	1.0	0.0	Dimensionless
Effective TDIF degradation rate when bound to PXY	0	0.0012	s^{-1}
K_{off}	0.02	0.02	s^{-1}

table S6. Auxin and TDIF gradient values

Auxin gradient			
Gradient strength	Weak	Intermediate	Strong
$drop_{xylem}$	60	30	20
$mod_{cambium}$	1.25	0.75	0.4
TDIF gradient			
Gradient strength	Weak	Intermediate	strong
p_T	0.065	0.13	0.26

Data S1
Source and RNA-seq data

Data S2
List of Primers, constructs, seeds